

## DYNAMIC MODELING OF EARLY DIAGENESIS AND NUTRIENT CYCLING. A CASE STUDY IN AN ARCTIC MARINE SEDIMENT

PETER BERG\*†, SØREN RYSGAARD\*\*, and BO THAMDRUP\*\*\*

**ABSTRACT.** In this paper, we present a dynamic diagenetic model of the oxygen consumption pathways and cycling of carbon, nitrogen, manganese, iron, and sulfur in marine sediments. Sixteen dissolved or solid species are included in our model and the vertical transport processes accounted for are molecular diffusion, bioturbation, irrigation, and burial. Adsorption of dissolved species onto solid sediment is assumed to be reversible and to follow a linear equilibrium isotherm. Interactions between species are formulated in 21 biogeochemical reactions that are regulated through simplified Michaelis-Menten kinetics. The key driving input parameter to the model is the transient flux of organic matter supplied to the sediment surface, below which mineralization is described through the well-known 3-G model that includes a fast, a slow, and a non-degradable pool of organic matter.

The model was applied to the Arctic sediment of Young Sound in Northeast Greenland using extensive measurements covering a full annual cycle. The model parameterization was performed in a stepwise process, first focusing on parameters describing transport in the sediment and then on parameters related to biogeochemical reactions. The model successfully simulated the measured concentration-depth profiles of  $O_2$ ,  $\Sigma CO_2$ ,  $NH_4^+$ ,  $NO_3^-$ ,  $Mn^{2+}$ ,  $Fe^{2+}$ , adsorbed  $Fe^{2+}$ ,  $SO_4^{2-}$ ,  $H_2S$ ,  $FeS$ ,  $FeS_2$ ,  $MnO_2$ ,  $FeOOH$ , and organic matter; sediment-water fluxes of  $\Sigma CO_2$ ,  $O_2$ ,  $NH_4^+$ , and  $NO_3^-$ ; depth-integrated process rates of denitrification and sulfate reduction; and depth profiles of iron and sulfate reduction rates. The model application to the Young Sound sediment provided an excellent means to examine whether our perceptions of the most significant transport processes and biogeochemical reactions were correct. The successful simulation of measured data supported their internal consistency and confirmed previously reported interpretations and conclusions.

The imposed supply of organic matter to the sediment surface that reproduced the measured data was found to be almost three times higher for the month of July than the average for the rest of the year. The peak in organic matter supply in mid-July coincided with the disappearance of sea ice. A sensitivity analysis performed for the model showed that the rate constants for the two degradable pools of organic matter were among those input variables that most affected the simulated results. As a result, we are confident of the accuracy of these rate constants of  $76\text{ y}^{-1}$  and  $0.095\text{ y}^{-1}$ . In comparison with results from temperate sediments, these constants showed no significant correlation to the sub-zero Arctic temperatures. The reproduction of measured data for the sulfur cycle could be obtained only when sulfur disproportionation was included in the model as a sink for  $S^0$ , indicating that this process plays an important role in the Young Sound sediment.

### INTRODUCTION

Mathematical modeling has become an indispensable tool in science. Many significant advances achieved in recent decades, for example in the fields of fluid mechanics and meteorology, have involved modeling as an essential component. Compared with other fields, the development and use of mathematical models for organic matter (OM) and nutrient diagenesis in marine sediments have had a

\*Department of Environmental Sciences, University of Virginia, Clark Hall, 291 McCormick Road, PO Box 400123, Charlottesville, Virginia 22904-4123, USA; pb8n@virginia.edu

\*\*National Environmental Research Institute, Department of Marine Ecology, Vejlsøvej 25, DK-8600 Silkeborg, Denmark

\*\*\*Danish Center for Earth System Science, Institute of Biology, University of Southern Denmark, Campusvej 55, DK-5230 Odense M, Denmark

†Corresponding author

surprisingly slow start. Boudreau (1996) speculated that this could be explained because many investigators working in the field traditionally are trained as experimentalists and lack the mathematical background to implement modeling. Another obvious reason is the lack of immediate commercial or military interest in the subject.

Mathematical models of OM and nutrient diagenesis in sediments are commonly based on mass conservation approaches expressing balances between vertical transport contributions of selected species and biogeochemical interactions between them. Significant benefits can be achieved by applying these transport-reaction models in experimental and descriptive field studies. First, they provide an excellent means to test our perception of which transport processes and biogeochemical reactions are important. A successful simulation of a monitored system strongly indicates that our understanding of the system is accurate. Second, large deviations between simulated and measured results indicate important gaps in our knowledge and point to areas in which additional research is needed. Third, if a model is successfully validated against measured data, it can be used as a predictive tool to study how the system will respond to various changes. Modeling of OM and nutrient diagenesis, however, is not trivial. It is a challenging task to identify and subsequently parameterize the transport processes and biogeochemical reactions necessary to simulate an appropriate fraction of the real and complex world. Furthermore, if models are used as predictive tools, it is essential to know the limitations of the assumptions upon which the models are based.

Many researchers consider the classic book by Berner (1980a) on early diagenesis to be a turning point in the use of modeling in the field. The book contains a large selection of analytical transport-reaction models and it illustrates convincingly the advantages of using mathematical models for interpretation of measured data and as tools for performing various analyses. Since only a limited number of mathematically-formulated problems can be solved analytically, there has been a shift over the years from a focus on analytical models to numerical models. A culmination was clearly seen in 1996, when four detailed transport-reaction models were published by Boudreau (1996), Dhakar and Burdige (1996), Soetaert and others (1996), and Van Cappellen and Wang (1996). The models are all based on a vertical one-dimensional description of the sediment column, and they represented the state of the art of modeling in the sense that they relied on and combined recent research findings.

Even though these models focus on the same subject, some clear differences can be identified. For example, two of the models are dynamic (Boudreau, 1996; Soetaert and others, 1996), while two consider only steady-state conditions (Dhakar and Burdige, 1996; Van Cappellen and Wang, 1996). With respect to the vertical transport in the sediment, all models account for molecular diffusion, burial, and bioturbation (the diffusion-like transport caused by random movements of fauna), while irrigation (the transport caused by pumping activity of tube-dwelling animals) is neglected in the model of Dhakar and Burdige (1996). This model also neglects sulfate reduction and all other processes describing the sulfur cycling, while the model by Soetaert and others (1996) lumps the cycling of manganese, iron, and sulfur into one. The four models also differ significantly in their description of carbon cycling. The model of Van Cappellen and Wang (1996) does not include any transport of OM, but imposes a known OM mineralization rate as a function of depth. The model of Dhakar and Burdige (1996) includes the transport of OM, but describes degradable OM as one constituent, thus disregarding variations in OM lability. Boudreau (1996) and Soetaert and others (1996) included several fractions of OM with different mineralization rates in their models as suggested in the well known multi-G model (Jørgensen, 1978; Berner, 1980b; Westrich and Berner, 1984). With respect to applications of the models, the work by Van Cappellen and Wang (1996) is particularly impressive

because of their thorough model parameterization and validation against detailed measurements by Canfield and others (1993a, 1993b).

Other modeling studies have been published since 1996. Some of them describe applications of the models reviewed briefly above (for example Boudreau and others, 1998; Herman and others, 2001), while other studies report simplifications or extensions of these models (for example Luff and others, 2000; Archer and others, 2002; Wijsman and others, 2002). One study, Meysman and others (2003a), offers a detailed comparison of the models of Van Cappellen and Wang (1996), Soetaert and others (1996), and Boudreau (1996). Using this comparison as a starting point, Meysman and others (2003b) developed a new object-based software package for early diagenesis modeling.

In this paper we present a model that also focuses on the OM and nutrient diagenesis in marine sediments. The model is dynamic, and describes the oxygen consumption pathways and the cycling of carbon, nitrogen, manganese, iron, and sulfur. With respect to vertical transport in the sediment, this model accounts for molecular diffusion, burial, bioturbation, and irrigation. The model includes adsorption processes, and the description of OM degradation is based on the multi-G model (Jørgensen, 1978; Berner, 1980b; Westrich and Berner, 1984). The model represents a significant extension of our earlier modeling effort (Rysgaard and Berg, 1996), and compared with all four models reviewed briefly above, our model differs on several important points. For example, in this model, the descriptions of transport contributions by bioturbation and irrigation differentiate among the species that are being simulated. The model includes additional processes such as sulfur disproportionation and more than one pool is utilized for some solid manganese and iron constituents. These differences were implemented based on extensive comparisons between simulated results and detailed measurements by Rysgaard and others (1998) covering a full annual cycle in the sediment of Young Sound, Northeast Greenland. From a modeling application perspective, there were some clear advantages in using measurements from this remote field site. For example, the water temperature was constant throughout the year, which allowed us to neglect all temperature effects in biogeochemical reactions. In addition, the dynamic input of OM to the sediment followed a relatively simple pattern largely controlled by the short, predictable sea ice break-up period. Finally, no benthic primary producers were present at the site.

The process of defining and parameterizing this particular model, which is capable of reproducing measured concentration profiles, fluxes, and process rates throughout the annual cycle, is a good and illustrative example of how new information can be obtained when modeling is applied in descriptive field studies. This process is the main focus of the paper.

#### MODEL FORMULATION

##### *Reactive Species*

The 16 dissolved or solid species included in the model are listed in table 1. As suggested by Westrich and Berner (1984) in their application of the multi-G model (Jørgensen, 1978; Berner, 1980b), three pools are utilized for OM to account for differences in OM lability. These pools consist of a fast decaying pool ( $OM_f$ ), a slow decaying pool ( $OM_s$ ), and a pool not decaying ( $OM_n$ ) on the time scale considered in the model. Furthermore, two pools are utilized for both  $MnO_2$  and  $FeOOH$  to distinguish fractions available to both bacterial and abiotic reactions ( $MnO_{2A}$ ,  $FeOOH_A$ ) from fractions only accessible to chemical reactions ( $MnO_{2B}$ ,  $FeOOH_B$ ). Three dissolved species,  $NH_4^+$ ,  $Fe^{2+}$ , and  $Mn^{2+}$ , can adsorb onto the solid sediment, a process that significantly enhances the capacity of the sediment to store these solutes, and as a result, the rate at which they are transported. The term  $\Sigma CO_2$  is used for total dissolved

TABLE 1

*Dissolved and solid species included in the model. Some species are represented by more than one pool.*

	Species	Number of pools	Name
Non-adsorbing solutes	Oxygen	1	O <sub>2</sub>
	Nitrate	1	NO <sub>3</sub> <sup>-</sup>
	Nitrogen gas	1	N <sub>2</sub>
	Dissolved inorganic carbon	1	ΣCO <sub>2</sub>
	Sulfide	1	H <sub>2</sub> S
	Sulfate	1	SO <sub>4</sub> <sup>2-</sup>
	Methane	1	CH <sub>4</sub>
Adsorbing solutes	Ammonium	1	NH <sub>4</sub> <sup>+</sup>
	Manganese	1	Mn <sup>2+</sup>
	Iron	1	Fe <sup>2+</sup>
Solids	Organic matter (OM)	3	OM <sub>f</sub> OM <sub>s</sub> OM <sub>n</sub>
	Iron (hydr)oxide	2	FeOOH <sub>A</sub> FeOOH <sub>B</sub>
	Manganese (hydr)oxide	2	MnO <sub>2A</sub> MnO <sub>2B</sub>
	Elementary sulfur	1	S <sup>0</sup>
	Iron sulfide	1	FeS
	Pyrite	1	FeS <sub>2</sub>

inorganic carbon (CO<sub>2</sub>, HCO<sub>3</sub><sup>-</sup>, CO<sub>3</sub><sup>2-</sup>). Phosphorus is not included in the model because only scant data were available for phosphorus in the Young Sound sediment and this prohibited thorough model parameterization and verification. It should be noted that the benthic phosphorus cycle does not exert any controls on the processes in the model. Furthermore, phosphorus does not limit primary production in the arctic sediments, and thus, has little effect on benthic-pelagic coupling (Rysgaard and others, 1999).

Throughout the paper the unit used for solutes is nmol (cm pore water)<sup>-3</sup> (referred to as μM below) and the unit of solids is nmol (g dry sediment)<sup>-1</sup> (referred to as nmol g<sup>-1</sup> below).

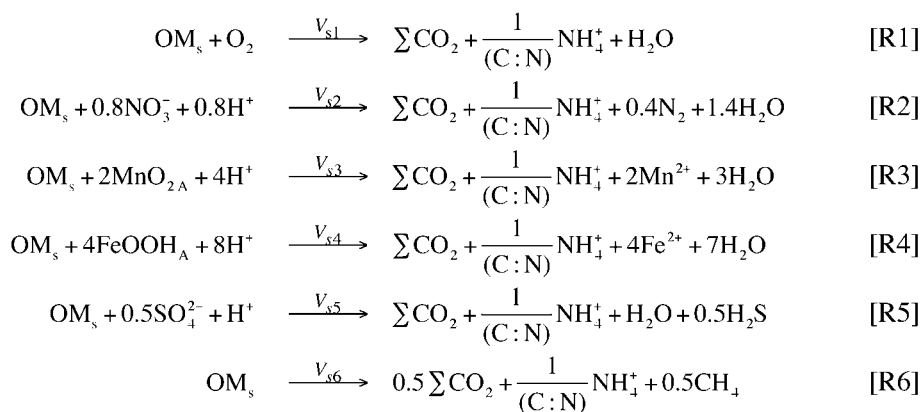
#### *Primary Redox Reactions*

Mineralization of OM in marine sediments is the result of many enzymatic reactions involving a variety of organisms and intermediate compounds. Despite this complexity, the net effect of OM degradation on pore water and solid constituents can be described by six reactions, referred to as primary redox reactions. These reactions (table 2) are heterotrophic oxygen respiration (R1), denitrification (R2), manganese reduction (R3), iron reduction (R4), sulfate reduction (R5), and methanogenesis

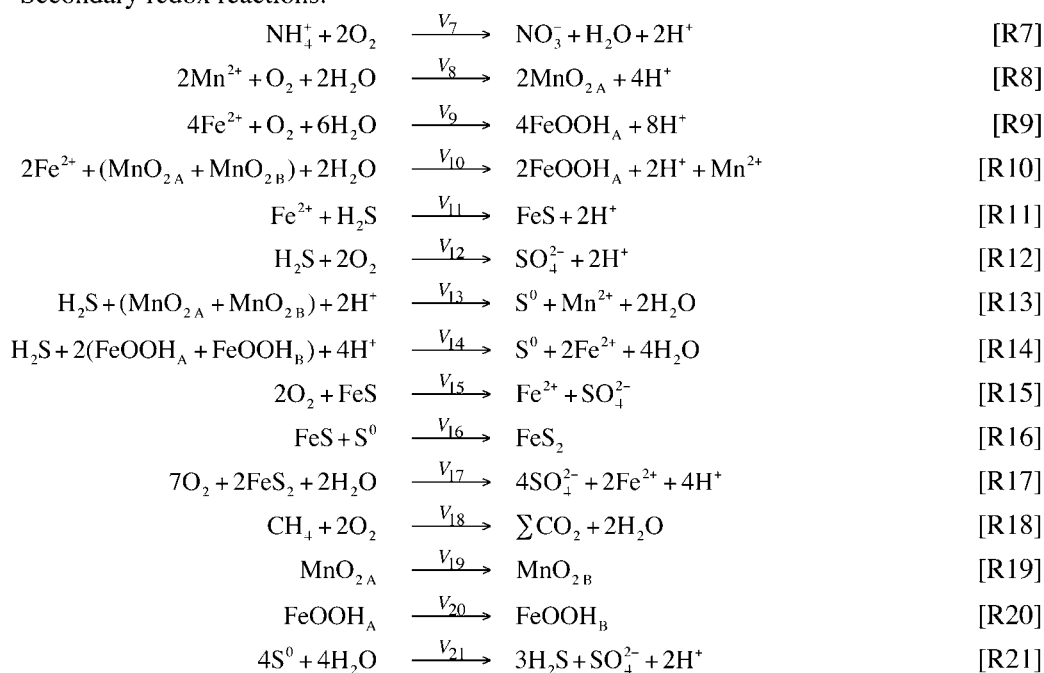
TABLE 2

Primary and secondary redox reactions accounted for in the model. Only the slow decomposing pool ( $OM_s$ ) is shown in the degradation of OM ( $(CH_2O)(NH_4^+)_{1/(C:N)}$ ). Reactions similar to R1 to R6 for the fast decomposing pool ( $OM_f$ ) are included in the model. Two pools each are included for  $FeOOH$  and  $MnO_2$ . Note that  $H^+$  is included in the reactions for balancing but is not included as a reactant in their regulation.

Primary redox reactions:



Secondary redox reactions:



(R6). The reactions are modified some from those defined by Froelich and others (1979) and Van Cappellen and Wang (1996). In reaction R1, organic nitrogen is not oxidized to  $NO_3^-$  as suggested by Froelich and others (1979) and Van Cappellen and Wang (1996), but is instead liberated as  $NH_4^+$  that can then be nitrified to  $NO_3^-$ .



through a secondary redox reaction (see below) in agreement with the current perception of benthic nitrogen transformations (Herbert, 1999). Likewise, Froelich and others (1979) assumed that organic nitrogen released during carbon oxidation coupled to manganese reduction was converted to  $\text{N}_2$ . In our equivalent reaction, (R3)  $\text{NH}_4^+$  is the inorganic nitrogen end product. This modification was made because  $\text{NH}_4^+$  oxidation to  $\text{N}_2$  with  $\text{MnO}_2$  was not detected in a recent study specifically examining the potential for this reaction in marine sediments (Thamdrup and Dalsgaard, 2000). The reactions shown in table 2 all contain the slow decaying OM pool ( $\text{OM}_s$ ). A similar set of reactions that contains the fast decaying OM pool ( $\text{OM}_f$ ) is also included in the model. In agreement with studies of marine cultures of  $\text{MnO}_2$ - and  $\text{FeOOH}$ -reducing bacteria (see below), the reduction of  $\text{MnO}_2$  and  $\text{FeOOH}$  coupled to OM oxidation (R3 and R4) uses only a subset of these oxides present in the sediment ( $\text{MnO}_{2A}$  and  $\text{FeOOH}_A$ ), which corresponds to the amorphous or poorly crystalline fraction. A larger fraction of these oxides is available for reaction with  $\text{H}_2\text{S}$  and, with respect to  $\text{MnO}_2$ , also  $\text{Fe}^{2+}$  (see below). The C:N ratio in the primary redox reactions represents the ratio between the production of  $\Sigma\text{CO}_2$  and  $\text{NH}_4^+$  when OM is mineralized and should be distinguished from the total C:N ratio of the sediment commonly measured in field studies. The order of the primary redox reactions in table 2 represents the sequence in which they occur with increasing sediment depth, a sequence that is in agreement with the decreasing free energy released through OM mineralization.

#### *Secondary Redox Reactions*

The primary redox reactions give rise to an array of reduced inorganic solutes. In marine sediments, a large fraction of these metabolites does not leave the sediment, but is re-oxidized through a series of secondary redox reactions or precipitate as authigenic minerals. As a whole, the secondary redox reactions included in the model (table 2) contain several substantial differences from the ones defined by Van Cappellen and Wang (1996). In contrast to their model, we have simplified our model by not including carbonate dissolution and precipitation reactions. The Young Sound sediment has a very low carbonate content ( $\leq 0.1$  weight percent C; S. Rysgaard unpublished data), and there was no evidence for any significant contribution of carbonate precipitation or dissolution to changes in  $\Sigma\text{CO}_2$  in anoxic incubation experiments (Rysgaard and others, 1998). Another important difference in our model compared to earlier ones lies in the description of the cycles of manganese, iron, and sulfur, and their interactions. Observations from Young Sound and other marine sediments indicate that a larger part of the benthic iron pool is available for reaction with  $\text{H}_2\text{S}$  (R14) than for organotrophic bacterial reduction (R4) (Canfield, 1989; Canfield and others, 1993a; Thamdrup and Canfield, 1996; Rysgaard and others, 1998). For that reason the model includes the two pools of  $\text{FeOOH}$  ( $\text{FeOOH}_A$  and  $\text{FeOOH}_B$ ). Less information is available on the availability of  $\text{MnO}_2$  for bacterial and chemical reduction in sediments, but based on the analogies between the manganese and iron cycles, the similar division of  $\text{MnO}_2$  was utilized. The oxidation of  $\text{Mn}^{2+}$  and  $\text{Fe}^{2+}$  (R8 and R9) produces poorly crystalline oxides that are available to both bacterial and abiotic reduction (Thamdrup, 2000), while the less reactive oxide pools are renewed through aging of the more reactive oxides (Cornell and Schwertmann, 1996; Taillefert and others, 2000) (R19 and R20). Furthermore, the oxidation of  $\text{Mn}^{2+}$  and  $\text{Fe}^{2+}$  with  $\text{O}_2$  in our model (R8 and R9) is described only as homogeneous reactions, whereas van Cappellen and Wang additionally included the catalysis on the surfaces of  $\text{MnO}_2$  and  $\text{FeOOH}$ , respectively. There is good evidence that biological catalysis dominates the oxidation of  $\text{Mn}^{2+}$  in marine sediments (Thamdrup and others, 1994a), and the same might be the case for  $\text{Fe}^{2+}$  oxidation with  $\text{O}_2$  (Emerson and Moyer, 1997; Sobolev and Roden, 2001). Thus, it is not clear that including surface catalysis provides a more correct description or deeper insight into the mechanisms of metal ion

oxidation. Most reduced  $\text{Fe}^{2+}$  in marine sediments is associated with the solid phase (Thamdrup and others, 1994b; Kostka and Luther, 1994). The particulate ferrous iron may be bound in a variety of different phases of which iron sulfides,  $\text{FeS}$  and  $\text{FeS}_2$ , are the only early diagenetic ferrous phases that are well-documented in surface layers (Berner, 1981; Thamdrup, 2000). The non-sulfide bound particulate ferrous pool as well as particulate  $\text{Mn(II)}$  are described as reversible adsorption (see below).

Our model incorporates three different pools of solid reduced sulfur,  $\text{S}^0$ ,  $\text{FeS}$ , and  $\text{FeS}_2$ . As in previous models,  $\text{FeS}$  and  $\text{S}^0$  are produced by reaction of  $\text{H}_2\text{S}$  with  $\text{Fe}^{2+}$  and  $\text{MnO}_2$  or  $\text{FeOOH}$ , respectively (R11, R13, R14). The pathways of pyrite ( $\text{FeS}_2$ ) formation in sediments still need clarification. For simplicity,  $\text{FeS}_2$  in our model is formed through the combination of  $\text{FeS}$  and  $\text{S}^0$  (R16; Berner, 1970) and may be oxidized by  $\text{O}_2$  (R17; Aller, 1980a). These reactions represent an extension relative to previous models that did not distinguish  $\text{FeS}$  and  $\text{FeS}_2$  and formulated iron sulfides only as  $\text{FeS}$ . Since iron sulfide formation is typically limited by iron availability (Canfield, 1989), and since  $\text{FeS}_2$  stores 67 percent more electron equivalents than  $\text{FeS}$ , it seems important to specifically include  $\text{FeS}_2$  in the diagenetic models of sediments where  $\text{FeS}_2$  is quantitatively important. Including reaction R16 also has the advantage of introducing a sink for  $\text{S}^0$ , which was not accounted for in the previous models. In the present model, large amounts of  $\text{S}^0$  can be produced through reaction R13 and R14, and in order to keep  $\text{S}^0$  from accumulating to unrealistic levels in the anoxic sediment, we found it necessary to include an additional sink in the form of sulfur disproportionation (R21, Thamdrup and others, 1993). Sulfur disproportionating bacteria are ubiquitous in marine sediments (Thamdrup and others, 1993; Canfield and Thamdrup, 1994; Finster and others, 1998), and in the only direct analysis of its significance in marine sediments thus far, the process was found to be the main sink for  $\text{S}^0$  (Canfield and Thamdrup, 1996).

#### *Regulation of Primary Redox Reactions*

Westrich and Berner (1984) followed decomposing planktonic material over a period of two years and showed that the amount of residual OM could be described at all times by the classic 3-G model (Jørgensen, 1978; Berner, 1980b; Westrich and Berner, 1984) as the sum of a fast decaying pool ( $\text{OM}_f$ ), a slow decaying pool ( $\text{OM}_s$ ), and an inert pool ( $\text{OM}_n$ ). Both decaying pools followed a simple exponential decline which mathematically are solutions to an equation of the form  $d[\text{OM}]/dt = -K_{\text{OM}}[\text{OM}]$  where  $[\text{OM}]$  is the concentration of the decaying OM pool,  $t$  is the time, and  $K_{\text{OM}}$  is a rate constant. We adopted this first-order kinetics in the regulation of the slow and the fast decomposing OM pools and assumed that the same rate constants apply to both oxic and anoxic mineralization (Westrich and Berner, 1984; for a discussion, see Kristensen and others, 1995).

As a first step when determining the primary redox reaction rates,  $V_{s1}$  to  $V_{s6}$ , the sum of the rates ( $V_s$ ) is calculated as a function of depth from the actual concentration profile of  $\text{OM}_s$  as  $V_s = K_{\text{OM}_s}(1 - \phi)\rho_s[\text{OM}_s]$ , where  $\phi$  is the porosity and  $\rho_s$  is the density of the solid sediment. The factor  $(1 - \phi)\rho_s$  serves as a conversion factor to give the reaction rate the unit of  $\text{mol time}^{-1} (\text{volume sediment})^{-1}$ . After  $V_s$  is determined,  $V_s$  is distributed on  $V_{s1}$  to  $V_{s6}$  following the procedure described by Van Cappellen and Wang (1996). The procedure is based on simplified Michaelis-Menten kinetics and is founded on the classic assumption that the electron acceptors in reaction R1 to R6 are consumed in the following order,  $\text{O}_2$ ,  $\text{NO}_3^-$ ,  $\text{MnO}_2$ ,  $\text{FeOOH}$ ,  $\text{SO}_4^{2-}$ , reflecting the decrease in free energy released as  $\text{OM}_s$  is oxidized. The depth intervals in which these oxidants are consumed are not fully separated and the degree of overlap is expressed by a set of limiting oxidant concentrations ( $[\text{O}_2]_{\text{lim}}$ ,  $[\text{NO}_3^-]_{\text{lim}}$ ,  $[\text{MnO}_2]_{\text{lim}}$ ,  $[\text{FeOOH}]_{\text{lim}}$ ,  $[\text{SO}_4^{2-}]_{\text{lim}}$ ) given as input to the model. More specifically, in the depth interval where  $[\text{O}_2] > [\text{O}_2]_{\text{lim}}$ ,  $\text{OM}_s$  is oxidized exclusively by  $\text{O}_2$  (R1), which means that  $V_{s1}$  is equal

to  $V_s$ , while all less energetic reactions (R2 to R6) are effectively inhibited. In the depth interval below where  $[\text{O}_2]_{\text{lim}} > [\text{O}_2] > 0$ ,  $V_{s1}$  is reduced proportionally to the  $\text{O}_2$  concentration so that  $V_{s1}$  is equal to  $V_s[\text{O}_2]/[\text{O}_2]_{\text{lim}}$ . In the same depth interval,  $\text{OM}_s$  is also oxidized by  $\text{NO}_3^-$  (R2), and because the sum of reaction rates of the active oxidation reactions (R1 and R2) always equals  $V_s$ ,  $V_{s2}$  is equal to  $V_s - V_{s1}$ . Obviously, reaction R1 comes to a complete halt when all  $\text{O}_2$  is consumed. The further distribution of  $V_s$  on  $V_{s3}$  to  $V_{s6}$  follows the same principle. The simplicity of this procedure, as reflected in the low number of input parameters, represents a significant advantage when formulating the regulation of the primary redox reactions. In reality this regulation is extremely complex and not yet fully understood.

Determination of the reaction rates  $V_{f1}$  to  $V_{f6}$  for the fast decomposing pool of OM is performed along the same lines. The sum of the reaction rates ( $V_f$ ) is calculated as  $V_f = (V_f:V_s)K_{\text{OM}_s}(1 - \varphi)\rho_s[\text{OM}_f]$  where the rate constant for the fast decomposing pool is specified as the factor,  $V_f:V_s$ , times the rate constant for the slow decomposing pool.

### *Regulation of Secondary Redox Reactions*

Several aspects of the secondary redox reactions included in the model (R7 to R21) are not yet fully understood. For example, it is still unclear for several of the reactions whether they are mediated by microbes or they are strictly chemically controlled (Van Cappellen and Wang, 1996). For other reactions the functional dependencies in their regulation are known, but it is still a challenging process to assign values to variables such as rate constants under realistic field conditions. As a consequence, it is a common practice when modeling these reactions to express their regulations by simple functional relationships requiring a minimum of input parameters. Van Cappellen and Wang (1996) regulated all secondary redox reactions in their model by the same simple rate law as  $K[\text{reactant}_1][\text{reactant}_2]$  where  $K$  is a rate constant. Boudreau (1996) adopted this formulation in his model and we have essentially done the same. Direct or indirect effects of pH on reaction kinetics were not included in the previous modeling studies, except in inorganic dissolution precipitation reactions, and we have also ignored such effects.

For the reactions where both reactants are solutes (R7, R8, R9, R11, R12, R18), the reaction rate is calculated as  $K\varphi[\text{solute}_1][\text{solute}_2]$  where  $\varphi$  serves as a conversion factor to give the reaction rate the desired unit of  $\text{mol time}^{-1} (\text{volume sediment})^{-1}$ . For reactions in which one solute reacts with one solid (R10, R13, R14, R15, R17), the reaction rate is calculated as  $K(1 - \varphi)\rho_s[\text{solute}][\text{solid}]$ , and for the single reaction in which both reactants are solids (R16), the reaction rate is calculated as  $K((1 - \varphi)\rho_s)^2[\text{solid}_1][\text{solid}_2]$ . For the two reactions describing the crystalline change of  $\text{MnO}_2$  and  $\text{FeOOH}$  (R19, R20), the reaction rate is calculated as  $K(1 - \varphi)\rho_s[\text{solid}]$ . Finally, the reaction rate of the  $\text{S}^0$  disproportionation (R21) is also calculated as  $K(1 - \varphi)\rho_s[\text{solid}]$ , and in addition, is inhibited by the presence of  $\text{H}_2\text{S}$  (Thamdrup and others, 1993). More specifically, this reaction rate is multiplied by the factor,  $1 - [\text{H}_2\text{S}]/[\text{H}_2\text{S}]_{\text{stop}}$ , where  $[\text{H}_2\text{S}]_{\text{stop}}$  is the  $\text{H}_2\text{S}$  concentration at which the reaction comes to a complete stop.

### *Net Production Rates*

Net production (or consumption) rates for all pools of species are determined from the stoichiometries of the primary and secondary redox reactions (table 2) and their calculated reaction rates. The net production rates are calculated as a function of depth for the entire sediment column considered in the model. As an example, the net production of  $\text{OM}_s$  is equal to  $-V_{s1} - V_{s2} - V_{s3} - V_{s4} - V_{s5} - V_{s6}$ . Likewise, the net production rate of  $\text{MnO}_{2\text{A}}$  is equal to  $-2(V_{s3} + V_{f3}) + 2V_8 - V_{10}\gamma_{\text{MnO}_2} - V_{13}\gamma_{\text{MnO}_2} -$



$V_{19}$  where  $\gamma_{\text{MnO}_2}$  is defined as the ratio  $[\text{MnO}_2]_{\text{A}} / ([\text{MnO}_2]_{\text{A}} + [\text{MnO}_2]_{\text{B}})$  while the net production rate of  $\text{MnO}_2_{\text{B}}$  is equal to  $-V_{10}(1 - \gamma_{\text{MnO}_2}) - V_{13}(1 - \gamma_{\text{MnO}_2}) + V_{19}$ .

#### Adsorption Processes

Adsorption (and desorption) of dissolved species onto the solid sediment is included in the model as a reversible, linear process assumed to be in local equilibrium at all times and at all depths. Consequently, the adsorbed amount of a solute is proportional to the surrounding pore water concentration and equal to  $K' C$  where  $K'$  is the adsorption constant and  $C$  is the pore water concentration of the adsorbing solute. This model implicitly assumes that adsorption happens at rates significantly faster than the vertical transport in the sediment, so that adsorption equilibrium is always present. This simple description of what are in reality complex adsorption processes is often used in diagenetic modeling (Berner, 1980a). More detailed models for adsorption processes exist, but are generally difficult to apply, because they rely on several input variables that are difficult to parameterize under realistic field conditions.

#### Transport Processes and Fluxes

The vertical transport processes included in the model are molecular diffusion, bioturbation, burial, and irrigation.

The flux of solutes by molecular diffusion is calculated from Fick's first law as  $-\phi D_s \partial C / \partial x$  where  $D_s$  is the molecular diffusivity corrected for tortuosity,  $C$  is the concentration, and  $x$  is the depth (positive downward). The porosity  $\phi$  and thus  $D_s$  can vary with depth, because  $D_s$  is calculated as function of  $\phi$  as  $D / (1 + 3(1 - \phi))$  according to Iversen and Jørgensen (1993) where  $D$  is the molecular diffusivity in water.

The transport of solutes and solids by bioturbation is also described as a diffusive process. By applying the same biodiffusivity ( $D_B$ ) for both types of species, bioturbation is commonly assumed to affect solutes and solids to the same degree. However, a recent study of Berg and others (2001) suggests that the effect of bioturbation on solutes can be many times stronger than on solids. Following Berg and others (2001) we have thus included this difference in the model by expressing the flux of solutes as  $-\phi D_{Bw} \partial C / \partial x$  where  $D_{Bw}$  is the biodiffusivity for solutes, and the flux of solids as  $-\rho_s(1 - \phi) D_{Bs} \partial C / \partial x$  where  $D_{Bs}$  is the biodiffusivity for solids. Both  $D_{Bw}$  and  $D_{Bs}$  are allowed to vary with depth. Bioturbation gives rise to an additional transport contribution for solutes that adsorb onto the solid sediment. Because the adsorbed fraction of a solute is equal to  $K' C$  according to the adopted adsorption model, this additional flux equals  $-\rho_s(1 - \phi) D_{Bs} K' \partial C / \partial x$ .

The advective transport contributions for the solutes and solids included are assumed to be exclusively the result of sediment burial. Thus, the vertical flux of solutes is equal to  $\phi u C$  where  $u$  is the burial velocity of pore water relative to the sediment-water interface. The equivalent expression for the flux of solids is  $\rho_s(1 - \phi) w C$  where  $w$  is the burial velocity of solids. At larger sediment depths where compaction, which is assumed to be a steady state phenomenon, has come to a halt,  $u$  and  $w$  are identical. Furthermore, continuity equations for dissolved and solid species ( $\partial(\phi u) / \partial x = 0$  and  $\partial((1 - \phi) w) / \partial x = 0$ ) expresses that the products  $\phi u$  and  $(1 - \phi) w$  are constant with depth. Thus, the vertical flux of solutes due to sediment burial can be expressed as  $[\phi u]_{\infty} C$  and the flux of solids as  $\rho_s [(1 - \phi) w]_{\infty} C$  where the notation  $[\ ]_{\infty}$  symbolizes that  $\phi u$  and  $(1 - \phi) w$  are evaluated at a depth where there is no sediment compaction. As for bioturbation, sediment burial causes an additional transport of adsorbing solutes that is equal to  $\rho_s [(1 - \phi) w]_{\infty} K' C$ .

Pore water irrigation is included through the non-local source-sink function suggested by Boudreau (1984) and Emerson and others (1984). The function ex-

presses that the removal or supply of a solute by irrigation at a given sediment depth is equal to  $\phi\alpha(C_0 - C)$  where  $\alpha$  is the irrigation coefficient and  $C_0$  is the water column concentration. Although pore water irrigation is clearly a complex three-dimensional phenomenon (Aller, 1980b) this function has been used successfully in numerous one-dimensional models (Boudreau, 1996; Van Cappellen and Wang, 1996; Berg and others, 1998; Fossing and others, 2000; Meile and others, 2001; Koretsky and others, 2002). Because the function expresses the average effect of irrigation at a given sediment depth, it provides the perfect match to the lateral average approach adopted in such one-dimensional models. In general,  $\alpha$  exhibits an overall decrease from the sediment surface towards the value of zero at some depth, reflecting the presence of active irrigating fauna. While it is common to use the same  $\alpha$  for all solutes this practice can lead to significant overestimation of the effects of irrigation on solutes that react with  $O_2$  in the sediment near the wall of well-irrigated burrows (see below). For that reason differing  $\alpha$  values are utilized for some solutes included in the model.

#### *Mass Conservation*

Mass conservation is fulfilled for all 20 pools of species included in the model (table 1) at all times. Mass conservation is expressed mathematically in a general mass balance equation that contains the flux contributions defined above. More specifically, the mass balance equation expresses for a thin horizontal layer (an infinitesimal control volume) located at any depth, that a concentration change over time equals the difference between vertical fluxes in and out of the control volume plus the sum of all sources (or sinks) within the control volume. These sources represent net production (or consumption) rates of the species, and if the species is a solute, also a removal or a supply by irrigation. Regardless of whether the species is a solute, solid, or solute that adsorbs onto solid sediment, all mass balance equations can be summarized mathematically in one equation as

$$(\xi\phi + \rho_s(1 - \phi)\kappa) \frac{\partial C}{\partial t} = \frac{\partial}{\partial x} \left( (\xi\phi(D_{Bw} + D_s) + \rho_s(1 - \phi)D_{B,\kappa}) \frac{\partial C}{\partial x} \right) - \frac{\partial}{\partial x} ((\xi[\phi w]_\infty + \rho_s[(1 - \phi)w]_x\kappa)C) + \xi\phi\alpha(C_0 - C) + R \quad (1)$$

where  $R$  is the net production rate (or consumption rate if  $R$  is negative) per unit volume of sediment. The variables  $\xi$  and  $\kappa$  indicate wherever the constituent is a solute ( $\xi = 1, \kappa = 0$ ), a solid ( $\xi = 0, \kappa = 1$ ), or a solute that adsorbs onto the solid sediment ( $\xi = 1, \kappa = K'$ ). For details on the derivation of such mass balance equations, see for example Berner (1980a, 1980b) or Boudreau (1997).

#### *Numerical Procedure*

A model simulation is performed in a stepwise process that moves forward through time in pre-defined time steps ( $\Delta t$ ). A central element in the simulation is the numerical solution to the general mass balance equation (eq 1) that is produced with the appropriate set of boundary conditions (see below) for each pool of species. In every time step, new concentrations, reaction rates, and fluxes are calculated as a function of depth for the time  $t + \Delta t$  based on known values valid for time  $t$ . These calculations are performed in the following order. Based on known concentrations at time  $t$ , all reaction rates ( $V_{s1}$  to  $V_{s6}$ ,  $V_{j1}$  to  $V_{j6}$ , and  $V_7$  to  $V_{21}$ ) are calculated from the reaction rate laws. From the reaction rates, net production rates are subsequently determined for all pools of species. The net production rates are then assumed to be valid for the time interval from  $t$  to  $t + \Delta t$  and used in the solutions of equation 1, which result in new concentrations and fluxes for time  $t + \Delta t$ . This procedure is repeated for each time step as the simulation moves forward in time.

The numerical solution to equation 1 is based on an implicit control volume technique as described by Berg and others (1998). The technique separates the sediment column under consideration and the fraction of the overlying water column defined by the diffusive boundary layer into a finite number of thin layers, so-called control volumes. Each control volume has a grid point located in its center. Each grid point has a unique concentration value of all pools of species. A typical number of control volumes is 100. Because the most pronounced concentration gradients are to be found near the sediment surface, the smallest size control volumes are defined here, and then increased gradually with depth.

When parameterizing the model, simulations are often performed every time a value of one or more input parameters is changed. Because simulated times of several centuries might be required before the full effect of such changes are seen, and because time steps of one hour typically are required to describe the fastest responding elements in the model correctly, such simulations can become time consuming. The control volume technique we use, however, is optimized specifically for minimal computation time. In short, this was done by decomposing the system of equations derived from the discretization of equation 1 only once, after which multiple solutions, one for every time step, can be produced with minimal computation. A unique feature of this technique allows this decomposition to be performed so that values of boundary conditions can vary as a simulation develops, without requiring new decompositions (Berg and others, 1998).

#### *Boundary Conditions*

The boundary conditions required in the numerical solution of equation 1, one for the top of the calculation domain and one for the bottom, can be of three types: a known concentration, a known flux, or a known concentration gradient. Upper boundary conditions are imposed at the top of the diffusive boundary layer for solutes and at the sediment-water interface for solids. No boundary conditions are needed for the adsorbed fractions of adsorbing solutes, because they are implicitly given through the conditions for dissolved fractions and the assumed local equilibrium in the adopted adsorption model.

A concentration gradient of zero ( $\partial C/\partial x = 0$ ) is specified as a lower boundary condition for all pools of species. We assumed that near quasi-steady state conditions are expected at the lower boundary and that the net production of all species has come to a complete halt at this depth, which will give rise to zero concentration gradients. This boundary condition allows the concentrations at the lower boundary to adjust to changes in the sediment above, and because the condition imposes diffusive fluxes equal to zero, any transport over the boundary is facilitated exclusively by burial.

In principle, all upper boundary conditions can vary with time. These transient conditions drive the dynamics in the model. Because known concentrations are specified for all solutes as upper boundary conditions, and since the boundary conditions are imposed at the top of the diffusive boundary layer, these concentrations represent values for the water column. For all solids, known fluxes are imposed over the sediment-water interface as upper boundary conditions. For OM the total flux  $J_{OM}$  is given as a key input parameter to the model and is then distributed between the three pools of OM ( $OM_f$ ,  $OM_s$ ,  $OM_n$ ) through the fractions  $\beta_{OMf}$  and  $\beta_{OMn}$  as follows

$$\begin{aligned} J_{OMf} &= \beta_{OMf} J_{OM} \\ J_{OMs} &= (1 - \beta_{OMf} - \beta_{OMn}) J_{OM} \\ J_{OMn} &= \beta_{OMn} J_{OM} \end{aligned} \tag{2}$$

Depending on the specific model application, both  $\beta_{\text{OMf}}$  and  $\beta_{\text{OMn}}$  can vary through time.

The total flux of  $\text{MnO}_2$  over the sediment surface consists of two contributions, one representing an external source ( $J_{\text{MnO}_2\text{ext}}$ ) and one originating from the flux of  $\text{Mn}^{2+}$  out of the sediment into the water column, where it is assumed to react with  $\text{O}_2$  and recycle back to the sediment as  $\text{MnO}_2$ . Because this reaction also takes place in the oxic zone of the sediment (R8) where in most cases it brings the  $\text{Mn}^{2+}$  concentration close to zero and effectively minimizes diffusive losses, this recycling mechanism is mainly supported by irrigation. Assuming that the transformation from  $\text{Mn}^{2+}$  to  $\text{MnO}_2$  happens instantaneously in the water column, the flux of recycled manganese can be calculated at any time during a simulation from already known variables. It is further assumed that recycled manganese is in a form accessible to both biological and abiotic reactions and thus included in the upper boundary conditions for  $\text{MnO}_{2\text{A}}$ . The distribution of the external flux  $J_{\text{MnO}_2\text{ext}}$  between the two  $\text{MnO}_2$  pools is defined through the fraction  $\beta_{\text{MnO}_2}$ . The imposed fluxes to the pools yields

$$J_{\text{MnO}_{2\text{A}}} = \beta_{\text{MnO}_2} J_{\text{MnO}_2\text{ext}} + \left( (\varphi D_s + \varphi D_{\text{Bw}} + \rho_s(1 - \varphi) D_{\text{Bs}} K'_{\text{Mn}}) \frac{\partial [\text{Mn}^{2+}]}{\partial x} \right) \Big|_{x=0} - ([\varphi w]_{\infty} + \rho_s[(1 - \varphi)w]_{\infty} K'_{\text{Mn}}) [\text{Mn}^{2+}]_{x=0} - \int_0^L \varphi \alpha_{\text{Mn}} ([\text{Mn}^{2+}]_0 - [\text{Mn}^{2+}]) dx$$

$$J_{\text{MnO}_{2\text{B}}} = (1 - \beta_{\text{MnO}_2}) J_{\text{MnO}_2\text{ext}} \quad (3)$$

where  $L$  is the depth of the calculation domain and  $[\text{Mn}^{2+}]_0$  is the water column concentration of  $\text{Mn}^{2+}$ . It should be noted that the only input variables that are not already known in equation 3 are  $\beta_{\text{MnO}_2}$  and  $J_{\text{MnO}_2\text{ext}}$ . The value of  $J_{\text{MnO}_2\text{ext}}$  can be estimated from manganese concentrations measured at the bottom of the calculation domain and the burial rate (see below).

Based on similar assumptions, the equivalent upper boundary conditions are used for the two pools of  $\text{FeOOH}$ .

For all remaining solid species ( $\text{S}^0$ ,  $\text{FeS}$ , and  $\text{FeS}_2$ ), a flux of zero is imposed as the upper boundary condition.

#### MODEL APPLICATION

The model presented here applies to many different types of sediments. In applications to a particular site, some input parameters, such as the supply of OM, are obviously specific to that site while others, such as certain rate constants, are of a more general nature. In typical site-specific applications, some input parameters can be assigned values before any simulations are performed, either directly from site-specific measurements or from literature surveys. Other input parameters must be given values in a trial-and-error process, in which model simulations are repeated and the parameters adjusted until acceptable agreements are obtained between simulated and measured results. Obviously, this distinction between input parameters will vary from application to application, depending on the site-specific measurements at hand. Given the large number of input parameters in the model, it is an advantage to assign values to as many parameters as possible before pursuing the more time-consuming parameterization by trial-and-error simulations.

Strong links exist between different elements in the model. For example, changes in the parameters describing the transport processes will obviously affect the cycling of all species included. Despite these links, it is still possible to parameterize some parts of the model before paying attention to others. For example, none of the solute and solid

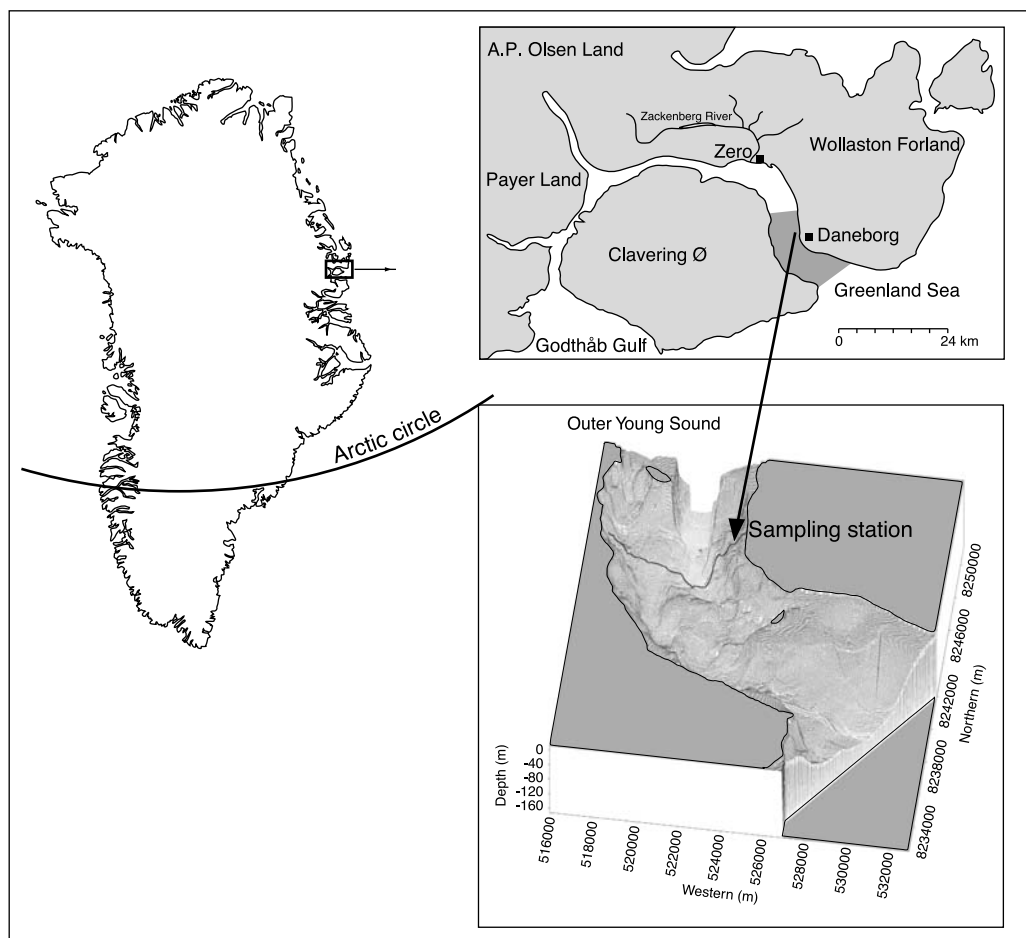


Fig. 1. Location of the site in Young Sound, Northeast Greenland, where model was applied.

concentrations affect the transport processes in the model. This makes it possible to parameterize the transport processes before variables related to the primary and secondary redox reactions are assigned values. Also, the carbon cycle is not affected by oxygen, nitrogen, manganese, iron, and sulfur constituents. This allows a complete parameterization of the carbon cycle before other cycles are addressed. In the specific model application presented below, manganese was present in such small concentrations that the other constituents were minimally affected by manganese cycling. For that reason, the manganese cycle was the last one to be parameterized.

#### Site

The model was applied to the sediment in Young Sound, Northeast Greenland (fig. 1;  $74^{\circ}18.58'N$ ,  $20^{\circ}15.04'W$ ), which has been monitored intensively by Rysgaard and others (1998). The site is located at a water depth of 36 meters and is covered by sea ice 9 to 10 months of the year. Despite air temperatures above  $0^{\circ}C$  during summer, the bottom water temperature remains below  $-1^{\circ}C$ . Intensive sampling took place from June through August 1996 and during February 1997. Rates of sedimentation, porosity and OM content were obtained. Furthermore, concentration profiles of  $O_2$ ,  $\Sigma CO_2$ ,  $NH_4^+$ ,  $NO_3^-$ ,  $Mn^{2+}$ ,  $Fe^{2+}$ ,  $SO_4^{2-}$ ,  $Mn(II)$ ,  $Fe(II)$ ,  $Fe(III)$ ,  $FeS$ , and  $FeS_2$  were measured 6 to 10 times during 1996 and 1997 together with the sediment-water fluxes



of  $O_2$ ,  $\Sigma CO_2$ ,  $NO_3^-$ ,  $NH_4^+$ , urea,  $PO_4^{3-}$  and Si. At the same time, denitrification and sulfate reduction rates were measured. Replicate measurements of all quantities were typically determined at each sampling event. The measured sediment-water fluxes exhibited a pronounced seasonal dynamic. An obvious goal in our modeling effort was to reproduce these changes over the year. The concentration profiles exhibited large spatial variation in most cases, which made it impossible to identify distinctive seasonal patterns. For that reason, the averages of all measured profiles throughout the year were used in the model parameterization. For further information on the site and the measurements see Rysgaard and others (1998) and also Rysgaard and others (1996, 1999).

Measured  $SO_4^{2-}$  concentrations in the sediment layer included in the model were never depleted to levels allowing the oxidation of OM by methanogenesis (R6). For that reason, all reactions involving  $CH_4$  were neglected. All model input parameters are listed in table 3 and their value assignments are described below in the order they were done.

#### *Calculation Domain*

The upper boundary of the calculation domain, equivalent to the top of the diffusive boundary layer above the sediment surface, was estimated from concentration-depth profiles of  $O_2$  measured with microelectrodes (Rysgaard and others, 1998). The lower boundary of the calculation domain was chosen from measured depth distributions of sulfate reduction rates (see below) so that no significant mineralization activity took place below this depth.

#### *Porosity and Density*

The measured porosity (fig. 2A) showed a clear decrease with depth below the sediment surface and reached a constant level at a few centimeters depth (Rysgaard and others, 1998). An exponentially declining function was fitted to the measurements and used to calculate the porosity for all the control volumes defined in the model. Because the measured density of the solid sediment did not exhibit any clear variations with depth (fig. 2B), the mean value of all measurements was used for all control volumes.

#### *Adsorption Coefficient*

The adsorption coefficient for  $NH_4^+$  was set to the average value determined in fine-grained coastal sediments by Mackin and Aller (1984).

The adsorption coefficient for  $Mn^{2+}$  was estimated by comparing the rate of  $Mn^{2+}$  accumulation in the pore water to the rate of carbon oxidation in anoxic incubations of surface sediments, where  $MnO_2$  was the only important electron acceptor. It was assumed that the  $Mn^{2+}$  produced from  $MnO_2$  reduction that was not recovered in the pore water had adsorbed onto the sediment. Using data from the 0 to 1 centimeter depth interval at two sites in Young Sound (Rysgaard and others, 1998; Glud and others, 2000), we obtained an adsorption coefficient ( $SE = 4$ ,  $n = 5$ ) that compared relatively well to the value of  $13 \text{ cm}^3 \text{ g}^{-1}$  determined in a  $MnO_2$ -poor Danish sediment (Canfield and others, 1993a).

By far, the most important adsorption processes are those involving  $Fe^{2+}$ . The  $Fe^{2+}$  speciation in suboxic marine sediments is characterized by an accumulation of a large particulate  $Fe^{2+}$  pool of unknown composition that is not iron sulfide. The depth distribution of this pool in marine sediments is typically similar to the distribution of soluble  $Fe^{2+}$  (Thamdrup and others, 1994b; Rysgaard and others, 1998), which suggests that the pool can be adequately described as reversibly adsorbed  $Fe^{2+}$ . It is important to note, however, that ferrous precipitates are likely to contribute to this pool, and that the adsorption coefficient needed to describe the pool probably

TABLE 3

*Model input parameters for the application to the Young Sound sediment. Some results from the modeling study of Van Cappellen and Wang (1996) are listed for comparison.*

Parameter	Value	Values from 7) and 8)	Source
Top of calculation domain	$x = -0.03 \text{ cm}$		1
Bottom of calculation domain	$x = 20 \text{ cm}$		*
Porosity	$\varphi = 0.631 + 0.207 e^{-1.02x}$		1
Density	$\rho_s = 2.41 \text{ g cm}^{-3}$		1
Adsorption coefficient	$K'_{\text{NH}_4} = 1.6 \text{ cm}^3 \text{ g}^{-1}$		2
„	$K'_{\text{Mn}} = 28 \text{ cm}^3 \text{ g}^{-1}$		1
„	$K'_{\text{Fe}} = 268 \text{ cm}^3 \text{ g}^{-1}$		*
Diffusivity at 0 °C	$D_{\text{O}_2} = 11.7 \times 10^{-6} \text{ cm}^2 \text{ s}^{-1}$		3
„	$D_{\text{NO}_3} = 9.8 \times 10^{-6} \text{ cm}^2 \text{ s}^{-1}$		4
„	$D_{\text{NH}_4} = 9.8 \times 10^{-6} \text{ cm}^2 \text{ s}^{-1}$		4
„	$D_{\text{N}_2} = 9.5 \times 10^{-6} \text{ cm}^2 \text{ s}^{-1}$		3
„	$D_{\Sigma\text{CO}_2} = 9.4 \times 10^{-6} \text{ cm}^2 \text{ s}^{-1}$		3
„	$D_{\text{H}_2\text{S}} = 8.7 \times 10^{-6} \text{ cm}^2 \text{ s}^{-1}$		3
„	$D_{\text{SO}_4} = 5.0 \times 10^{-6} \text{ cm}^2 \text{ s}^{-1}$		4
„	$D_{\text{Mn}} = 3.1 \times 10^{-6} \text{ cm}^2 \text{ s}^{-1}$		4
„	$D_{\text{Fe}} = 3.4 \times 10^{-6} \text{ cm}^2 \text{ s}^{-1}$		4
Biodiffusivity for solutes	$x \leq 4 \text{ cm:}$ $D_{Bw} = 4.6 \times 10^{-6} \text{ cm}^2 \text{ s}^{-1}$ $x > 4 \text{ cm:}$ $D_{Bw} = 4.6 \times 10^{-6} e^{-0.35(x-4)} \text{ cm}^2 \text{ s}^{-1}$		5
Biodiffusivity for solids	$D_{Bs} = D_{Bw}/12$		5
Sedimentation rate	$w = 0.12 \text{ cm year}^{-1}$		6
Irrigation parameter	$x \leq 16 \text{ cm:}$ $\alpha = 48(1 - x/16) \text{ year}^{-1}$ $x > 16 \text{ cm:}$ $\alpha = 0 \text{ year}^{-1}$		*
„	$\alpha_{\text{Mn}} = 0.2 \alpha$		*
„	$\alpha_{\text{Fe}} = 0 \text{ year}^{-1}$		*

TABLE 3  
(continued)

Parameter	Value	Values from 7) and 8)		Source
Boundary conditions for solutes	$[\text{O}_2]_{x=-0.03} = 389 \mu\text{M}$			1
„	$[\text{NO}_3^-]_{x=-0.03} = 6.2 \mu\text{M}$			1
„	$[\text{NH}_4^+]_{x=-0.03} = 0.58 \mu\text{M}$			1
„	$[\text{N}_2]_{x=-0.03} = 669 \mu\text{M}$			1
„	$[\Sigma\text{CO}_2]_{x=-0.03} = 2203 \mu\text{M}$			1
„	$[\text{H}_2\text{S}]_{x=-0.03} = 0 \mu\text{M}$			1
„	$[\text{SO}_4^{2-}]_{x=-0.03} = 27300 \mu\text{M}$			1
„	$[\text{Mn}^{2+}]_{x=-0.03} = 1 \mu\text{M}$			1
„	$[\text{Fe}^{2+}]_{x=-0.03} = 0 \mu\text{M}$			1
Flux of OM	See Fig. 10			*
Fraction	$\beta_{\text{OMn}} = 0.32$			*
„	$\beta_{\text{OMf s}} = 0.25$			*
„	$\beta_{\text{OMf b}} = 0.14$			*
Ratio	$V_f : V_s = 800$			*
„	$\text{C:N} = 10.3$			*
External flux of FeOOH	$J_{\text{FeOOH ext}} = 5.2 \times 10^{-4} \text{ nmol cm}^{-2} \text{ s}^{-1}$			*
Fraction	$\beta_{\text{FeOOH}} = 0.5$			*
External flux of MnO <sub>2</sub>	$J_{\text{MnO}_2 \text{ ext}} = 1.5 \times 10^{-6} \text{ nmol cm}^{-2} \text{ s}^{-1}$			*
Fraction	$\beta_{\text{MnO}_2} = 0.5$			*
Limiting concentration	$[\text{O}_2]_{\text{lim}} = 20 \mu\text{M}$	20	(1 – 30)	7,8
„	$[\text{NO}_3^-]_{\text{lim}} = 2 \mu\text{M}$	2 – 5	(4 – 80)	7,8
„	$[\text{MnO}_2]_{\text{lim}} = 10000 \text{ nmol g}^{-1}$	4000 – 32000		*
„	$[\text{FeOOH}]_{\text{lim}} = 20000 \text{ nmol g}^{-1}$	65000 – 100000		*

TABLE 3  
(continued)

Parameter	Value	Values from 7) and 8)		Source
Rate constant	$K_{\text{OMs}} = 3.0 \times 10^{-9} \text{ s}^{-1}$			*
„	$K_7 = 6.3 \times 10^{-7} \mu\text{M}^{-1} \text{ s}^{-1}$	$1.6 \cdot 10^{-7}$	$(\sim 3.2 \cdot 10^{-7})$	*
„	$K_8 = 1.1 \times 10^{-8} \mu\text{M}^{-1} \text{ s}^{-1}$	0		*
„	$K_9 = 1.1 \times 10^{-6} \mu\text{M}^{-1} \text{ s}^{-1}$	$1.1 \cdot 10^{-6}$		7,8
„	$K_{10} = 7.5 \times 10^{-11} \mu\text{M}^{-1} \text{ s}^{-1}$	$9.5 \cdot 10^{-8} - 3.2 \cdot 10^{-7}$	$(< 3.2 \cdot 10^{-5})$	*
„	$K_{11} = 4.7 \times 10^{-7} \mu\text{M}^{-1} \text{ s}^{-1}$			*
„	$K_{12} = 5.1 \times 10^{-9} \mu\text{M}^{-1} \text{ s}^{-1}$	$5.1 \cdot 10^{-9}$	$(\geq 5.1 \cdot 10^{-9})$	7,8
„	$K_{13} = 2.0 \times 10^{-9} \mu\text{M}^{-1} \text{ s}^{-1}$	$6.3 \cdot 10^{-10}$	$(< 3.2 \cdot 10^{-6})$	*
„	$K_{14} = 1.4 \times 10^{-9} \mu\text{M}^{-1} \text{ s}^{-1}$	$2.5 \cdot 10^{-10}$	$(< 3.2 \cdot 10^{-9})$	*
„	$K_{15} = 6.0 \times 10^{-9} \mu\text{M}^{-1} \text{ s}^{-1}$	$1.9 \cdot 10^{-9} - 1.0 \cdot 10^{-8}$		*
„	$K_{16} = 2.3 \times 10^{-10} \text{ cm}^3 \text{ nmol}^{-1} \text{ s}^{-1}$			*
„	$K_{17} = 3.0 \times 10^{-10} \mu\text{M}^{-1} \text{ s}^{-1}$			*
„	$K_{18}$ not used			*
„	$K_{19} = 5.4 \times 10^{-8} \text{ s}^{-1}$			*
„	$K_{20} = 1.8 \times 10^{-8} \text{ s}^{-1}$			*
„	$K_{21} = 1.0 \times 10^{-7} \text{ s}^{-1}$			*
Inhibiting conc.	$[\text{H}_2\text{S}]_{\text{stop}} = 10 \mu\text{M}$			*

1) Rysgaard and others (1998); 2) Mackin and Aller (1984); 3) Broecker and Peng (1974); 4) Li and Gregory (1974); 5) Berg and others (2001); 6) Rysgaard and others (1996); 7) Van Cappellen and Wang (1996); 8) Wang and Van Cappellen (1996); \*This study.

represents an overestimation of the true coefficient for immediate reversible adsorption. We have estimated the  $\text{Fe}^{2+}$  adsorption constant specifically for the site using measured iron partitioning. We assumed that the adsorbed  $\text{Fe}^{2+}$  consisted of the entire non-sulfide-bound extractable  $\text{Fe}(\text{II})$  pool as determined along with the pore water concentration of  $\text{Fe}^{2+}$  (fig. 3) by Rysgaard and others (1998). With the adopted adsorption model, the  $\text{Fe}^{2+}$  adsorption coefficient was then defined as  $K'_{\text{Fe}} = [\text{adsorbed } \text{Fe}^{2+}]/[\text{Fe}^{2+}]$ . Large variations were found when the coefficient was initially estimated as the ratio between the two pools in depth-to-depth comparisons, especially near the sediment surface, where the  $\text{Fe}^{2+}$  concentrations were close to zero and where the assumption of equilibrium in the adopted adsorption model is dubious. For

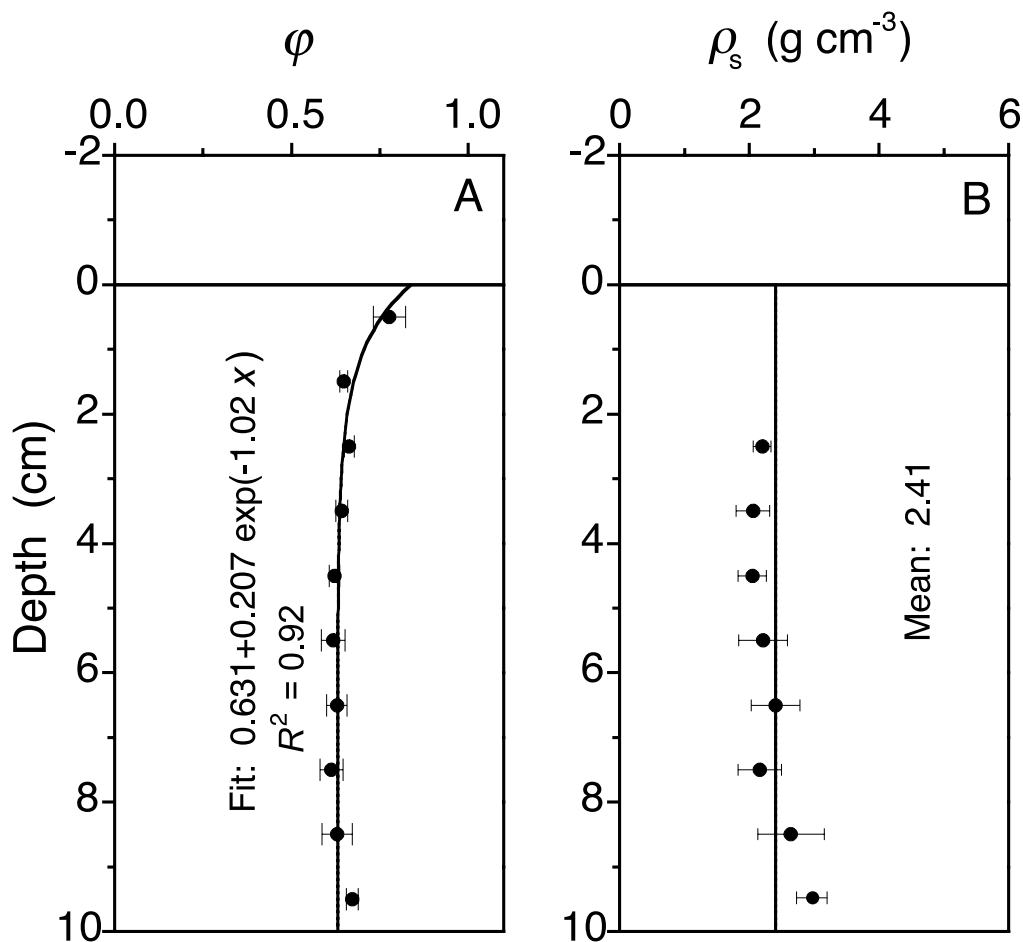


Fig. 2. (A) Measured porosity fitted by an exponentially declining function (error bars represent  $\pm 1$  SE,  $n = 3$ ). (B) Measured and mean sediment density of the solid sediment fraction (error bars represent  $\pm 1$  SE,  $n = 3$ ). The fit to the porosity and the mean sediment density were used as input to the model.

that reason, we used a more advanced methodology that took advantage of the clear overall parabolic shape of both the  $\text{Fe}^{2+}$  and the adsorbed  $\text{Fe}^{2+}$  profiles (fig. 3). Based on the adopted adsorption model, parabolic fits to these profiles can be written as  $[\text{Fe}^{2+}] = ax^2 + bx + c$  and  $[\text{adsorbed Fe}^{2+}] = K'_{\text{Fe}}(ax^2 + bx + c)$  where  $x$  is the depth and constants  $a$ ,  $b$ , and  $c$  have the same values in the two expressions. These three constants and the value of  $K'_{\text{Fe}}$  were found in a least-squared fitting process where fits to both profiles were determined simultaneously (fig. 3).

#### Diffusivities

Molecular diffusivities for all solutes in free water were taken from Broecker and Peng (1974) and Li and Gregory (1974).

The biodiffusivities, one for solutes and one for solids, were adopted from Berg and others (2001) who determined the diffusivities for the same site in Young Sound as used in this model application. In short, the biodiffusivities were estimated from tracer experiments with both dissolved and solid tracers (bromide, oxygen, glass beads, and  $^{210}\text{Pb}$ ) combined with inverse modeling of the vertical tracer distributions. Although not conclusive, the results of Berg and others (2001) also suggested a decline in the biodiffusivities below a depth of approximately 4 centimeters (fig. 4A). The decrease



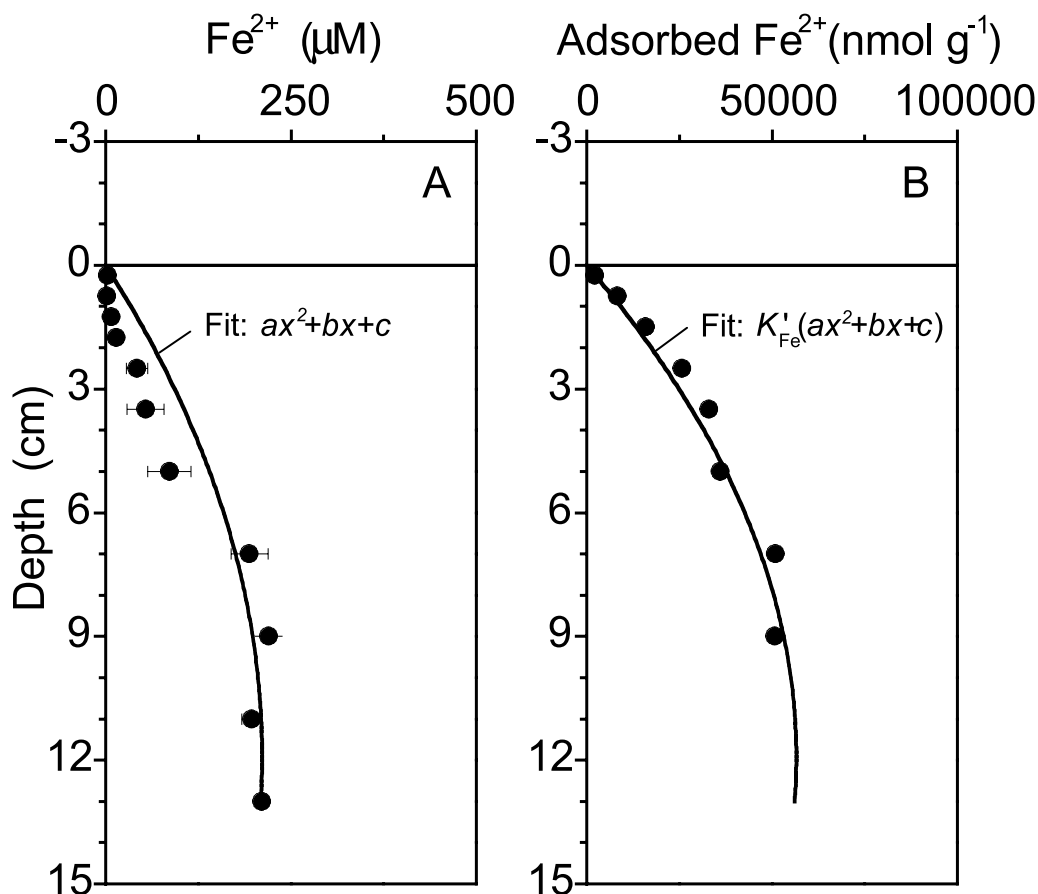


Fig. 3. Estimation of the adsorption coefficient for  $\text{Fe}^{2+}$ . (A) Measured  $\text{Fe}^{2+}$  profile that was fitted with the parabola  $ax^2 + bx + c$  (error bars represent  $\pm 1$  SE,  $n = 6$ ). (B) Measured profile of adsorbed  $\text{Fe}^{2+}$  that was fitted with the parabola  $K'_{\text{Fe}}(ax^2 + bx + c)$ . The three constants  $a$ ,  $b$ ,  $c$ , and  $K'_{\text{Fe}}$  were determined simultaneously in the same fitting process.

was approximated by an exponential declining function. This depth variation agrees well with the one argued for in other modeling studies (fig. 4B).

#### Sedimentation

The sedimentation rate was taken from Rysgaard and others (1996), who estimated the value from triplicate  $^{210}\text{Pb}$  profiles measured in the Young Sound sediment.

#### Irrigation Parameters

The amount and distribution of  $\Sigma\text{CO}_2$  in the sediment represents a balance between the OM mineralization (R1 to R6) and the vertical transport in the sediment. After  $\Sigma\text{CO}_2$  is produced, it is assumed to act as a conservative tracer and is removed from the sediment by molecular diffusion, bioturbation and irrigation. This characteristic behavior of  $\Sigma\text{CO}_2$  was used to determine the irrigation parameter used for most solutes in a series of trial-and-error simulations in which the simulated production of  $\Sigma\text{CO}_2$  was temporarily substituted with a hypothetical depth profile of OM mineralization (fig. 5). The hypothetical profile was derived from the measured sulfate reduction rate and the measured  $\Sigma\text{CO}_2$  flux out of the sediment. At depths where the OM mineralization was determined to take place exclusively by sulfate reduction (see below), the measured sulfate reduction rates exhibited an almost linear decrease with

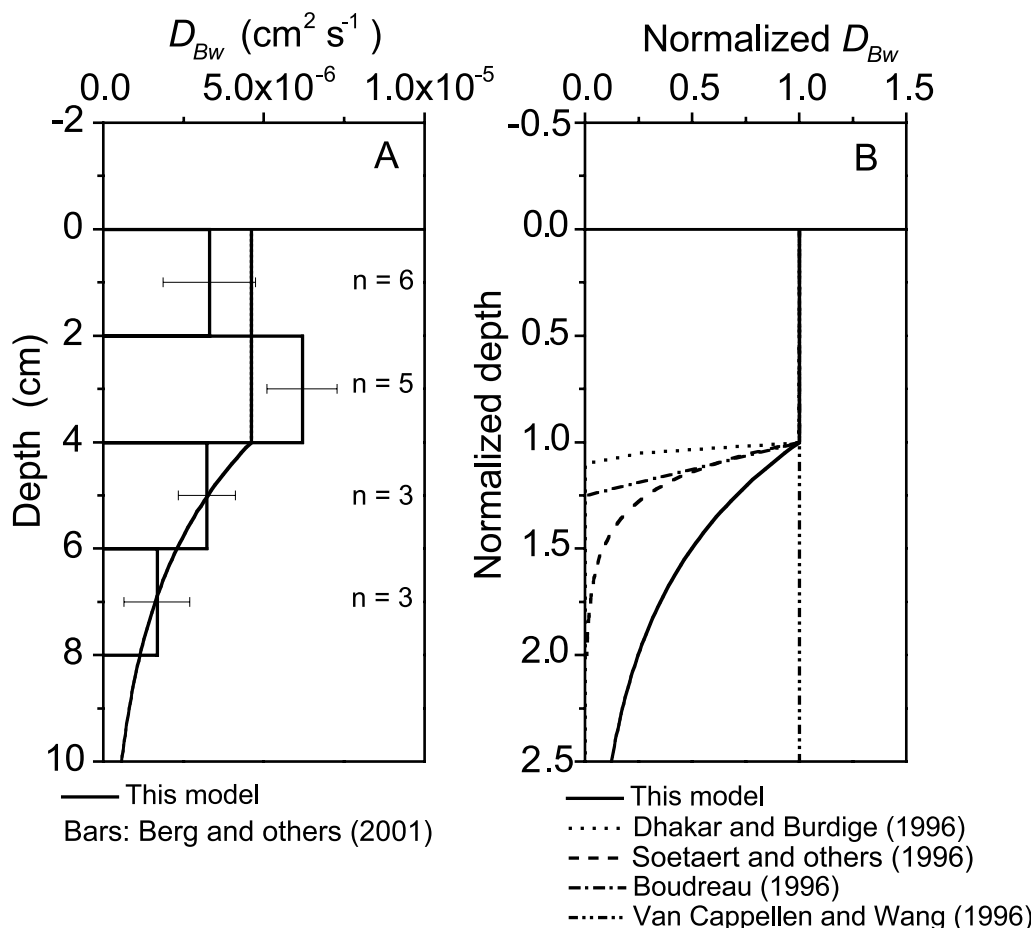


Fig. 4. Depth variations of biodiffusivities used in this and other studies. (A) The biodiffusivity estimated by Berg and others (2001) for the Young Sound sediment and the derived fit used in this model (error bars represent  $\pm 1$  SE). (B) Depth variations used in this and other models.

depth (fig. 5A). For that reason, the OM decomposition was approximated with a straight line overlaid with an exponential declining function as  $R_{\text{OM}} = a + bx + c \exp(-dx)$  where  $x$  is the depth and  $a$ ,  $b$ ,  $c$ , and  $d$  are constants. The values of  $a$  and  $b$  were found from a linear fit to the lowest data points on the sulfate reduction rate profile (fig. 5A). The values of  $c$  and  $d$  were determined so that the depth integration of  $R_{\text{OM}}$  equaled the average measured  $\Sigma\text{CO}_2$  flux out of the sediment, and further, so that the depth integration of  $R_{\text{OM}}$  over the 0 to 1.5 centimeter depth equaled 38 percent of this flux. This last condition was defined from estimates by Rysgaard and others (1998), who determined that approximately 38 percent of the total annual OM mineralization was facilitated by oxic decomposition in the upper 1 to 1.5 centimeter sediment layer. The resulting hypothetical profile for OM mineralization (fig. 5A) was imposed in a series of steady-state, trial-and-error simulations in which the irrigation parameter, specified as a function of depth, was varied until a good agreement between the measured and simulated  $\Sigma\text{CO}_2$  profiles was achieved (fig. 5B, 5C, and 5D). The sensitivity of the simulated  $\Sigma\text{CO}_2$  profile to dynamic changes through the annual cycle is examined below.

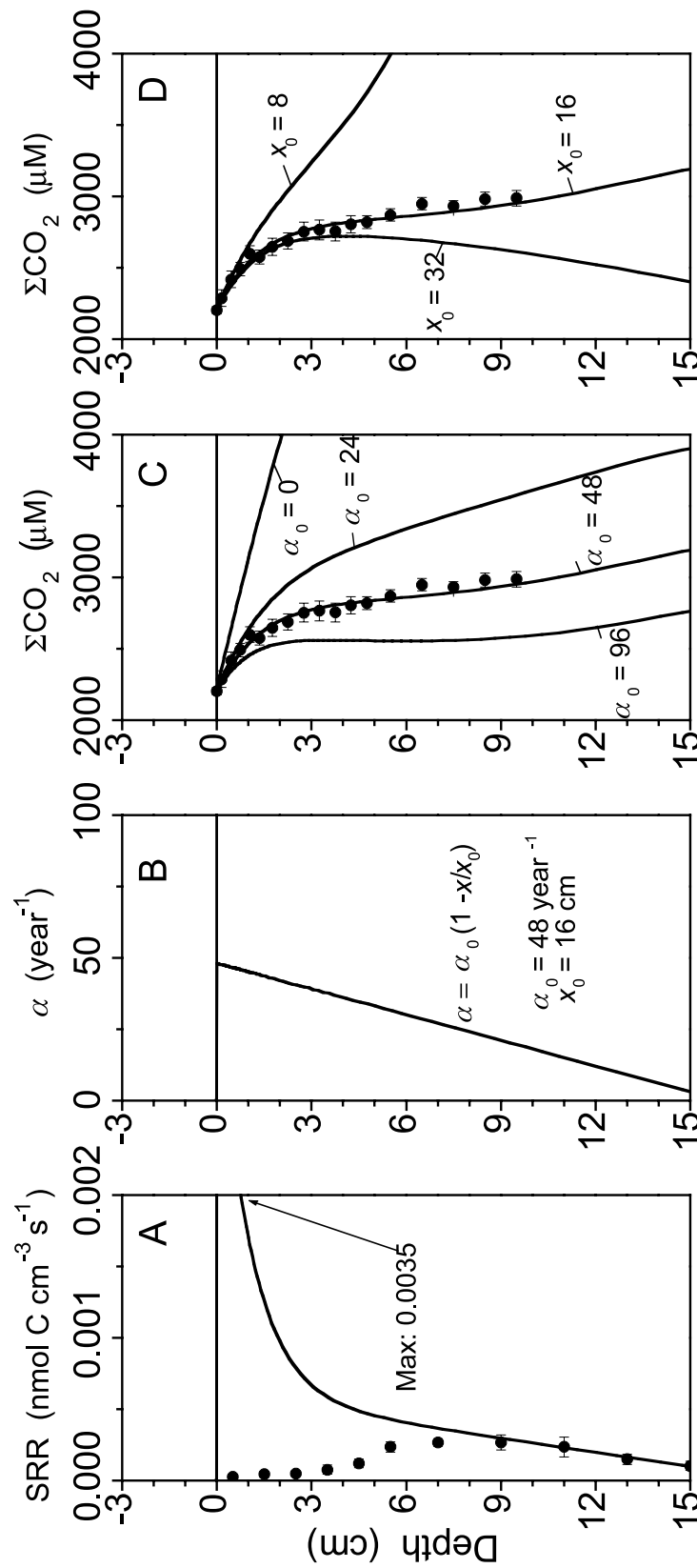


Fig. 5. Estimation of the irrigation parameter used for most solutes. (A) Measured sulfate reduction rates and a hypothetical profile for OM mineralization (error bars represent  $\pm 1 \text{ SE}$ ,  $n = 6$ ). (B) The irrigation parameter was assumed to vary linearly with depth and to be uniquely determined through the variables  $\alpha_0$  and  $x_0$ . (C) Measured and simulated  $\Sigma\text{CO}_2$  profiles for different values of  $\alpha_0$  (error bars represent  $\pm 1 \text{ SE}$ ,  $n = 18$ ). (D) Measured and simulated  $\Sigma\text{CO}_2$  profiles for different values of  $x_0$  (error bars represent  $\pm 1 \text{ SE}$ ,  $n = 18$ ).

To our knowledge, all previous multi-component models that have accounted for irrigation through the non-local source-sink function (Boudreau, 1984; Emerson and others, 1984) have used the same irrigation parameter for all solutes. This can lead to significant overestimation of the effects of irrigation for solutes such as  $\text{NH}_4^+$ ,  $\text{Mn}^{2+}$ ,  $\text{Fe}^{2+}$ , and  $\text{H}_2\text{S}$  that react with  $\text{O}_2$  in the sediment near the wall of well-irrigated burrows as illustrated in the following example.

Consider first a solute, such as  $\Sigma\text{CO}_2$ , that is formed in the sediment matrix through organic matter mineralization and hereafter is considered as a conservative constituent. This production will lead to a build up of  $\Sigma\text{CO}_2$  in the sediment matrix and will result in a transport, likely dominated by molecular diffusion, towards the sediment-water interface and also towards the lower concentration level in a well-irrigated burrow (fig. 6A). Since the average  $\Sigma\text{CO}_2$  concentration in the sediment matrix is larger than the water column concentration, the non-local source-sink function will predict correctly a removal of  $\Sigma\text{CO}_2$  from the sediment, which will occur from the depth in focus at a rate of  $\varphi\alpha([\Sigma\text{CO}_2]_0 - [\Sigma\text{CO}_2])$  where  $[\Sigma\text{CO}_2]_0$  is the water column concentration of  $\Sigma\text{CO}_2$ . Consider next a solute, such as  $\text{Fe}^{2+}$ , that also is produced in the same sediment but has a high potential for reacting rapidly with another solute, such as  $\text{O}_2$ , that is present in the burrow. Also in this situation a build up of  $\text{Fe}^{2+}$  will occur in the sediment matrix and will result in a transport towards the burrow (fig. 6B), but instead of being released to the burrow, it is fully consumed in the sediment matrix near the burrow wall through reaction with  $\text{O}_2$ . Since the average  $\text{Fe}^{2+}$  concentration in the sediment matrix in this situation is also larger than the water column concentration (fig. 6B), the non-local source-sink function will mistakenly predict a removal of  $\text{Fe}^{2+}$  from the sediment. We have corrected for this limitation of the source-sink function by utilizing reduced irrigation parameters for such solutes wherever it was quantitatively possible.

For  $\text{Mn}^{2+}$ , we estimated a reduced irrigation parameter relative to the one found for  $\Sigma\text{CO}_2$  by combining interpretations of measured concentration profiles and model simulations of the manganese cycle. Manganese appears in two forms in the model, either as a solute ( $\text{Mn}^{2+}$ ) or as a solid ( $\text{MnO}_2$ ). This implies, in depth-to-depth comparisons, that any production (or consumption) of  $\text{Mn}^{2+}$  or  $\text{MnO}_2$  always matches an equally-sized consumption (or production) of  $\text{MnO}_2$  or  $\text{Mn}^{2+}$ . Furthermore, since only  $\text{Mn}^{2+}$  is influenced by irrigation, information on the irrigation parameter can be extracted from the measured  $\text{Mn}^{2+}$  and  $\text{MnO}_2$  profiles. The measured profile of  $\text{Mn}^{2+}$  (fig. 7A) was used as input to an extended version of the profile interpretation procedure, PROFILE, of Berg and others (1998) that can include equilibrium adsorption and burial effects. In short, this procedure first determines an appropriate fit to the  $\text{Mn}^{2+}$  profile based on F-statistics, and from that, the  $\text{Mn}^{2+}$  production rate as a function of depth. The irrigation parameter determined for  $\Sigma\text{CO}_2$  (fig. 5) was used in the first interpretation and resulted in a good fit to the measured  $\text{Mn}^{2+}$  profile as reflected in the  $R^2$  value of 0.98 (fig. 7A). The corresponding production profile for  $\text{Mn}^{2+}$  (fig. 7A) was then mirrored and imposed as a consumption profile for  $\text{MnO}_2$  in a steady-state model simulation (fig. 7B). If the irrigation parameter determined for  $\Sigma\text{CO}_2$  also applied to  $\text{Mn}^{2+}$ , then an acceptable reproduction of the measured  $\text{MnO}_2$  profile should be expected. The large deviation between the two profiles was found to be the direct result of the limitation of the non-local source-sink function. The measured  $\text{Mn}^{2+}$  profile (fig. 7A) contained an apparent maximum at 7 to 12 centimeters depth, despite the fact that no consumption below this depth was expected. This characteristic suggested that  $\text{Mn}^{2+}$  was to some degree influenced by irrigation. Through a series of new profile interpretations and subsequent model simulations, reduction to 20 percent of the irrigation parameter determined for  $\Sigma\text{CO}_2$  was found to

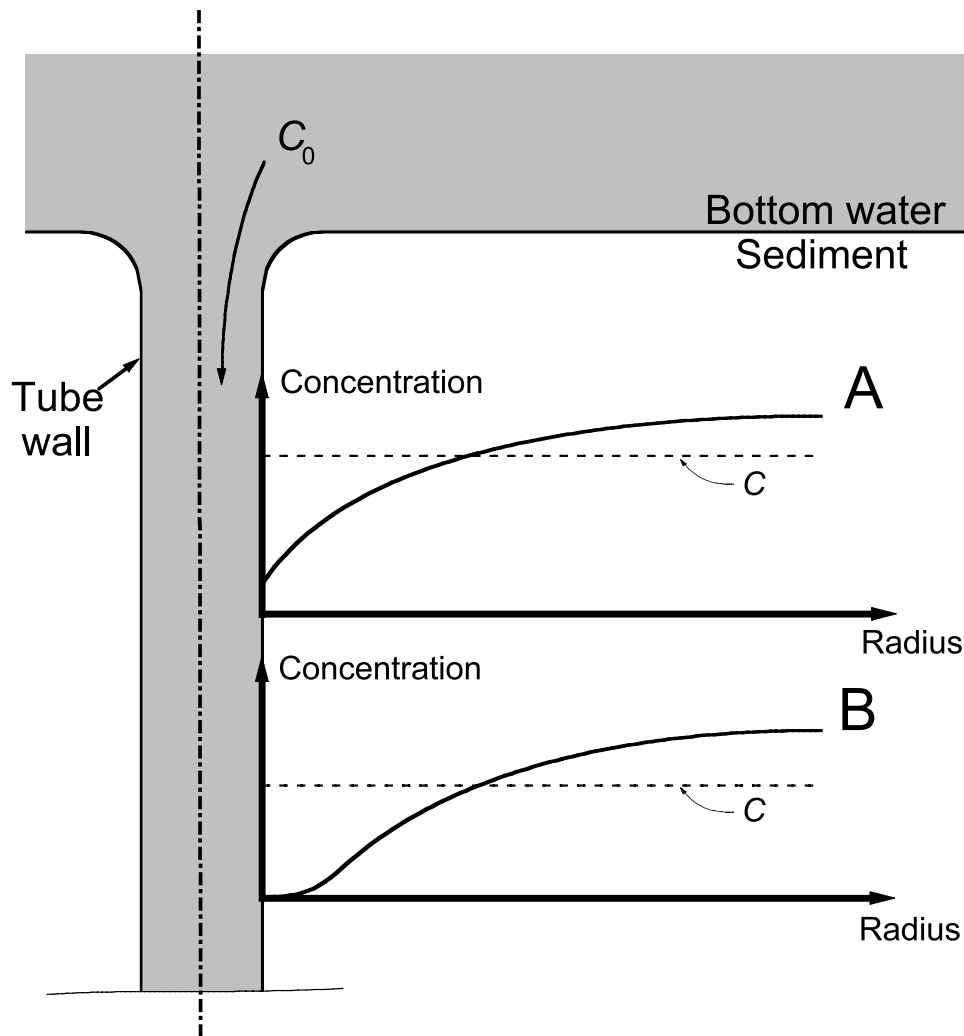


Fig. 6. Pore water concentrations of two solutes in the sediment around a well-irrigated burrow. (A) This solute is produced in the sediment and diffuses towards the lower concentration level in the burrow. Since the mean solute concentration ( $C$ ) is larger than the water column concentration ( $C_0$ ), the non-local source-sink function correctly predicts a removal of the solute from the sediment. (B) This solute is also produced in the sediment but has a high potential of reacting with  $O_2$  present in the burrow. Also in this situation the solute diffuses towards the burrow, but instead of being released to the burrow it is consumed in the sediment near the burrow wall. Since the mean solute concentration ( $C$ ) is larger than the water column concentration ( $C_0$ ), the non-local source-sink function will mistakenly predict a removal of the solute from the sediment.

give an acceptable agreement between the simulated and measured  $MnO_2$  profiles (fig. 7B).

Because the oxidation of  $Fe^{2+}$  with  $O_2$  is much faster than the oxidation of  $Mn^{2+}$ , at least for abiotic reactions (Stumm and Morgan, 1981), and because fluxes of soluble  $Fe^{2+}$  from sediments underlying oxic water are generally negligible (Balzer, 1982), we assumed an irrigation parameter for  $Fe^{2+}$  equal to zero. Reduction of the irrigation parameter for  $H_2S$  was not relevant because  $H_2S$  was measured and later simulated (see below) to be present only in concentrations near or below the detection limit ( $< 1 \mu M$ ). Finally, the irrigation parameter for  $NH_4^+$  was not reduced relative to the one determined for  $\Sigma CO_2$ , because adequate measurements to support such an analysis



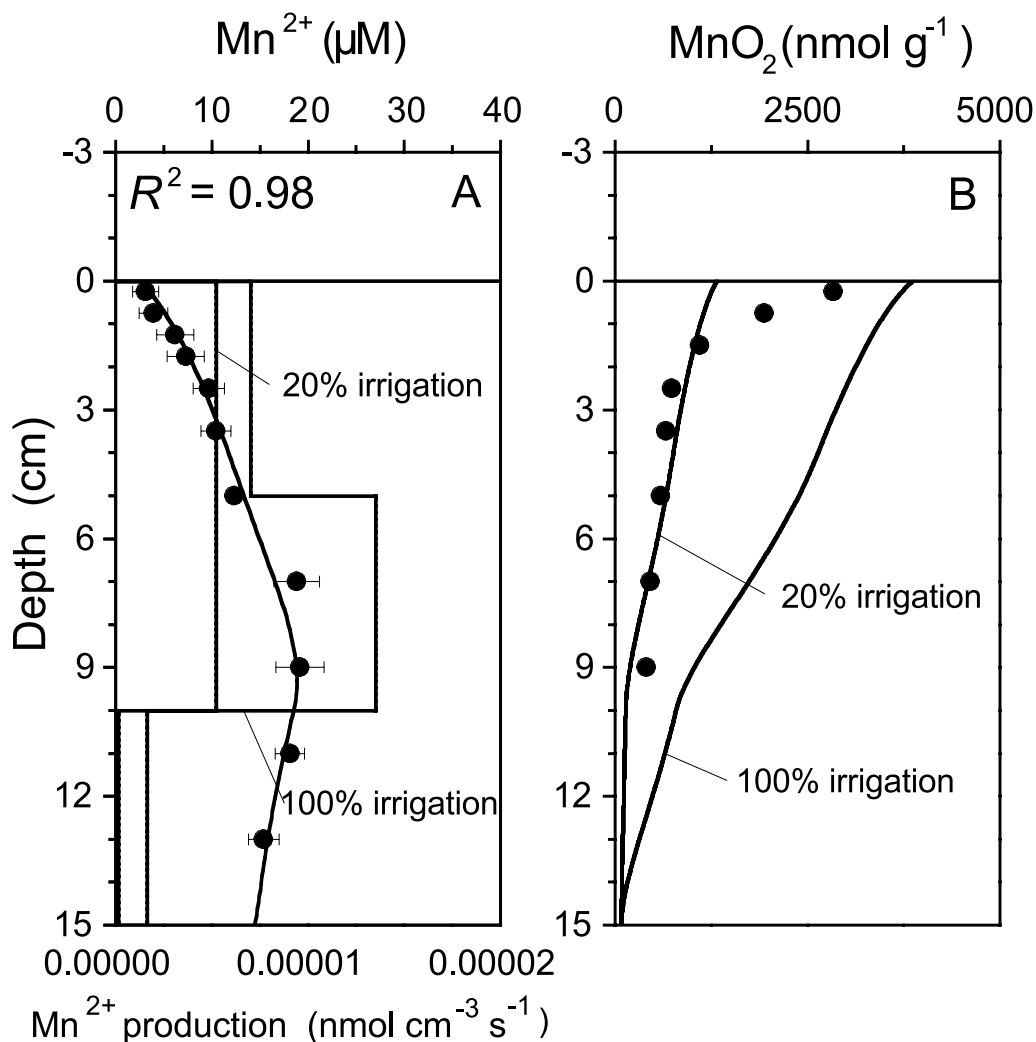


Fig. 7. Estimation of the irrigation parameter for Mn<sup>2+</sup>. (A) Two profile interpretations of the measured Mn<sup>2+</sup> profile performed with a modified version of PROFILE (Berg and others, 1998; error bars represent  $\pm 1$  SE,  $n = 6$ ). In one interpretation the irrigation parameter was reduced to 20 percent relative to the one determined for  $\Sigma\text{CO}_2$  (fig. 5). The two derived production profiles for Mn<sup>2+</sup> were then imposed as consumption profiles for MnO<sub>2</sub> in steady-state model simulations. (B) A good agreement between the simulated and the measured MnO<sub>2</sub> profiles was obtained only when the irrigation parameter for Mn<sup>2+</sup> was reduced.

were not available (see discussion below). More research is needed to investigate the effect of irrigation on different solutes and, if possible, to define general guidelines for how the irrigation parameter should vary for different solutes.

#### Boundary Conditions

Measured solute concentrations in the bottom water over the sediment showed relatively little variation throughout the year (Rysgaard and others, 1998). For that reason, the average of these concentrations was imposed as the upper boundary condition for these solutes. Note that boundary conditions not specific for the Young Sound site are described above.

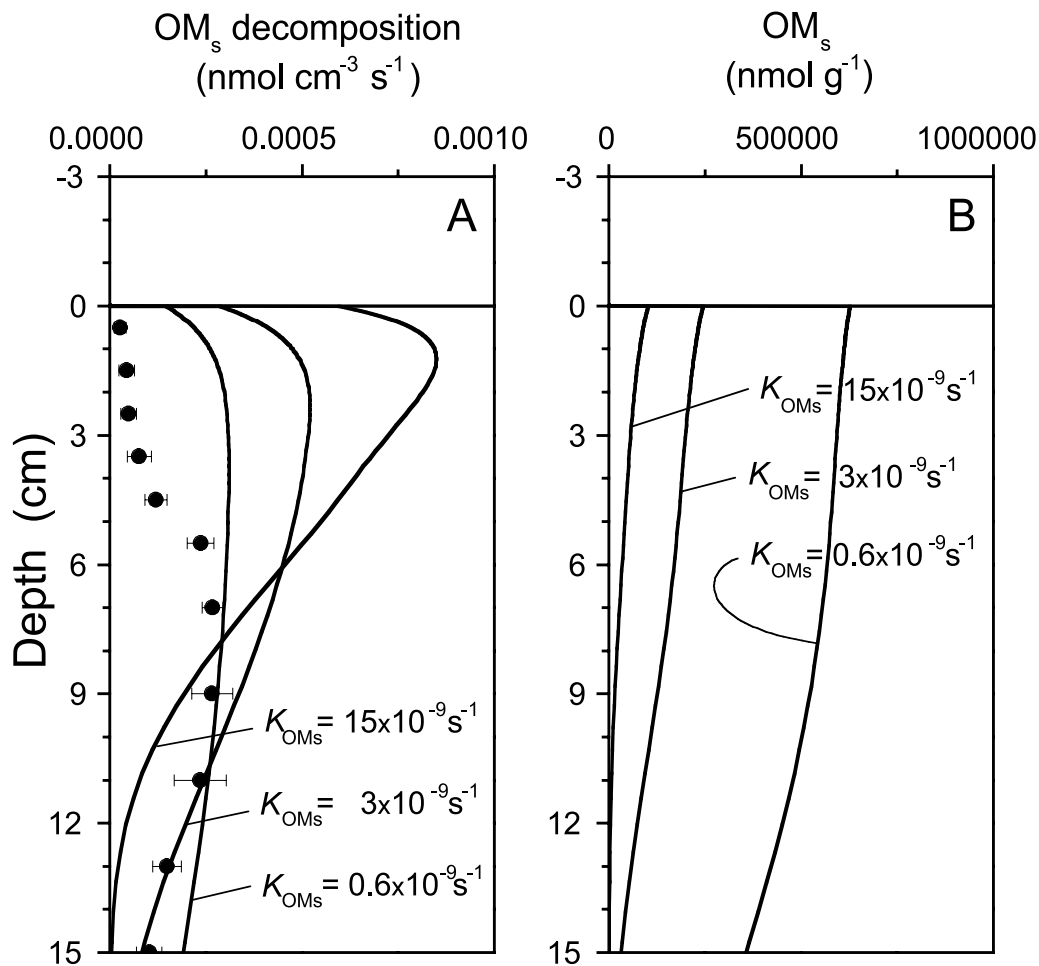


Fig. 8. Estimation of the rate constant for the slow decomposing OM pool. (A) Measured OM mineralization rates by sulfate reduction and simulated rates for different rate constants (error bars represent  $\pm 1$  SE,  $n = 6$ ). (B) Simulated build-up of OM in the slow decomposing pool for different rate constants.

#### *Remaining Input for Carbon Cycling*

The measurements of Rysgaard and others (1998) indicated that OM in the 10 to 15 centimeter depth interval was mineralized exclusively by sulfate reduction (see below). Furthermore, a constant OM mineralization throughout the year was expected in this depth interval as a result of the constant, year-round water temperature and an assumed uniform lability of OM. We used this information to quantify the rate constant,  $K_{OMs}$ , for the slow decomposing pool of OM (OM<sub>s</sub>). As later verified to be correct, all activity of the fast decomposing pool (OM<sub>f</sub>) was assumed to be limited to the upper few centimeters of the sediment. The value of  $K_{OMs}$  was found by comparing simulated OM mineralization rates for the OM<sub>s</sub> pool in the 10 to 15 centimeter depth interval with measured sulfate reduction rates in a series of steady-state, trial-and-error simulations (fig. 8A). In these simulations a constant total flux of decaying OM was supplied to the sediment surface as it was estimated by Rysgaard and others (1998). Seventy-five percent of this flux was imposed on the slow decomposing pool while 25 percent was imposed on the fast pool, a ratio that was chosen from mineralization studies of Westrich and Berner (1984) and Otsuki and Hanya (1972). In incubations

starting with fresh planktonic material, Westrich and Berner (1984) followed the OM decomposition over a period of two years and subsequently fitted the 3-G model to the data. Their regressions showed a 24/76 percent split between the slow and the fast pool at time zero, but as the result of rapid decay of the fast pool, a 75/25 percent split was predicted by the 3-G model after 37 days. A similar fit of the 3-G model to the data of Otsuki and Hanya (1972) showed that a 75/25 percent split was obtained after 13 days. The 75/25 percent split chosen in our model parameterization was based on the assumption that the OM supply to the sediment consisted mainly of planktonic material of some weeks of age. It should be noted that some precaution should be shown when the 3-G model applied to experiments of Westrich and Berner (1984) or Otsuki and Hanya (1972) is compared with the application in our model. The duration of these two experiments was 1 to 2 years while the age of OM described in our model is on the order of 100 years. These differences might have some effect on the distribution of OM between the fast and slow decomposing pools.

The ratio between the rate constants for the fast and slow decomposing OM pools ( $V_f:V_s$ ) was determined from comparisons of simulated oxic mineralization rates with  $O_2$  consumption rates estimated from measured  $O_2$  profiles. The comparisons were confined to the top millimeter of the sediment (fig. 9), where it was assumed that all OM mineralization was oxic. As later verified to be correct, it was further assumed that all secondary redox reactions consuming  $O_2$  were insignificant to OM mineralization in the top millimeter of the sediment and thus, that all  $O_2$  consumption originated from OM mineralization. A series of  $O_2$  profiles (fig. 9A) was used as input into the interpretation procedure, PROFILE, of Berg and others (1998). The resulting  $O_2$  consumption profiles were averaged (fig. 9B) and assumed to represent an average over the year based on the time when the  $O_2$  profiles were measured. In a series of trial-and-error simulations, the value of  $V_f:V_s$  was determined so that the consumption rate from both pools of OM in the top millimeter of the sediment was equal to the one found from the  $O_2$  profile interpretations (fig. 9B).

Only a few measurements of the sedimentary flux of OM in Young Sound were performed by Rysgaard and others (1998) (fig. 10A). For that reason, we relied mostly on a more frequently measured variable, the  $\Sigma CO_2$  flux out of the sediment, to quantify the time-dependent flux of degradable OM supplied to the sediment surface over the year. As expressed in the primary redox reactions (R1 to R6), the OM mineralization is equal to the  $\Sigma CO_2$  production, which in turn, with the zero gradient imposed at the lower boundary, is practically equal to the  $\Sigma CO_2$  flux out of the sediment. As later verified to be correct, the simulated  $\Sigma CO_2$  flux out of the sediment was assumed to respond almost instantaneously to changes in the input of degradable OM. The same was assumed for the measured  $\Sigma CO_2$  flux, which appeared to exhibit a remarkably constant level throughout the year, except for a short significant peak during the month of July (fig. 10B). We used this distinctive pattern to define the total OM flux over the year as consisting of two contributions, a constant base contribution overlaid by a short intense summer pulse. The annual  $\Sigma CO_2$  flux was estimated by Rysgaard and others (1998) to be  $2300 \text{ mmol m}^{-2} \text{ year}^{-1}$  and the burial flux of OM was estimated to be  $1100 \text{ mmol m}^{-2} \text{ year}^{-1}$  from the burial rate and measured OM concentrations at depths near the bottom of the calculation domain (see later). These two contributions were used to define the fraction  $\beta_{OMn}$  in equation 2, which was assumed to be constant over the year. Based on the variation of the  $\Sigma CO_2$  flux during the summer period (fig. 10B), the summer pulse of OM was assumed to have a triangular shape with a maximum in mid-July and a length of 35 days (fig. 10A). It was also assumed that the maximum value of the total OM flux equaled a sedimentary OM flux measured in mid-to-late July (fig. 10A). These assumptions were sufficient to uniquely define the total OM flux over the year (fig. 10A).

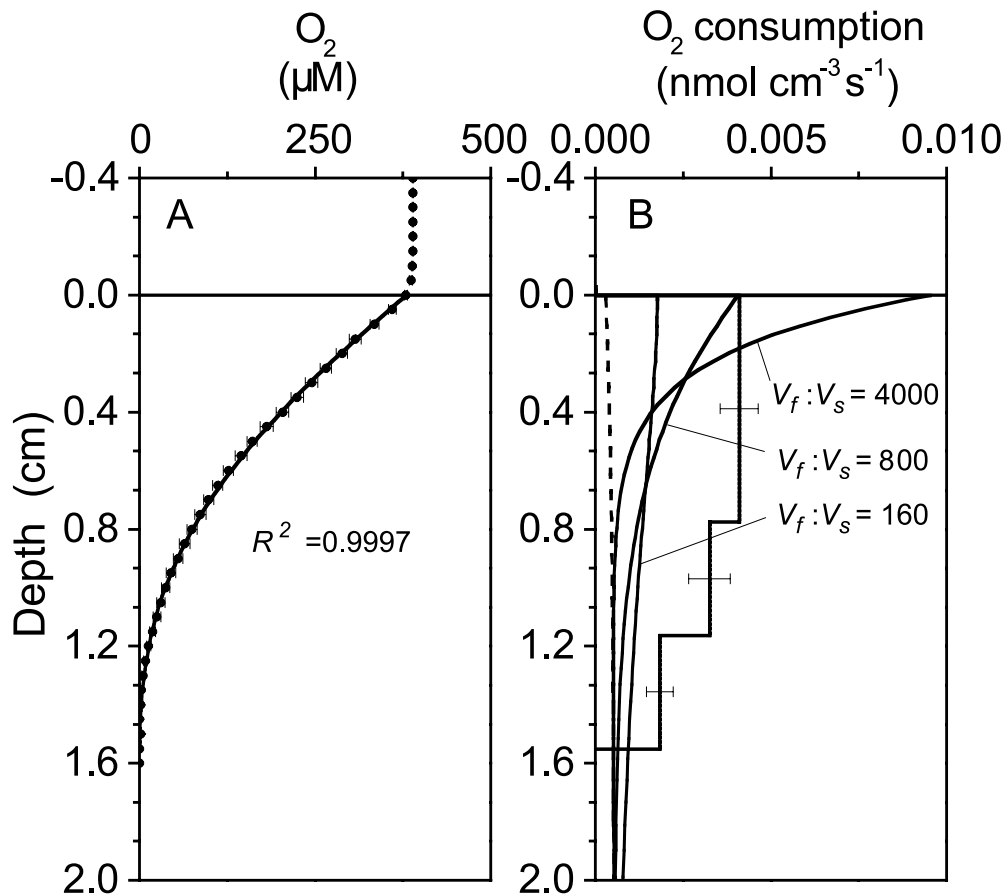


Fig. 9. Estimation of the ratio between the rate constants for the slow and the fast decomposing OM pools ( $V_f:V_s$ ). (A) Measured O<sub>2</sub> profile and its fit calculated with the interpretation procedure PROFILE (Berg and others, 1998; error bars represent  $\pm 1$  SE,  $n = 7$ ). (B) O<sub>2</sub> consumption rates estimated by PROFILE (step curve) and model simulated OM decomposition rates (smooth curves) for different values of  $V_f:V_s$  (error bars represent  $\pm 1$  SE,  $n = 7$ ). The dashed line represents OM decomposition of the slow pool, and the solid lines represent the total decomposition from both the slow and the fast pool. Note that the comparison was confined to the top millimeter of the sediment.

Knowing the total OM flux and the buried OM fraction, the distribution between the slow and fast decomposing pools of OM was then determined. Rysgaard and others (1999) showed through water column measurements that the elevated  $\Sigma\text{CO}_2$  flux out of the sediment in July (fig. 10B) was directly correlated to a phytoplankton bloom. Thus, we used a higher value of  $\beta_{\text{OMf}}$  in equation 2 for the summer pulse of OM than for the base contribution. These two variables are referred to as  $\beta_{\text{OMfs}}$  and  $\beta_{\text{OMfb}}$ . Valid values for  $\beta_{\text{OMfs}}$  and  $\beta_{\text{OMfb}}$  are constrained by the 75/25 percent split between the annual average input to the slow and fast decomposing OM pools discussed previously. In a series of dynamic trial-and-error simulations, the value of  $\beta_{\text{OMfs}}$  and  $\beta_{\text{OMfb}}$  were determined so that the simulated  $\Sigma\text{CO}_2$  flux agreed with the measured flux (fig. 10B). Each of these trial-and-error simulations required many simulated years to obtain quasi-stationary results on a year-to-year basis.

With known values for these variables, the carbon cycling was fully parameterized. Earlier in the parameterization process, the irrigation parameter for  $\Sigma\text{CO}_2$  was determined in comparisons of measured and simulated  $\Sigma\text{CO}_2$  profiles, where the latter were based on an annually averaged, hypothetical depth profile of OM mineralization

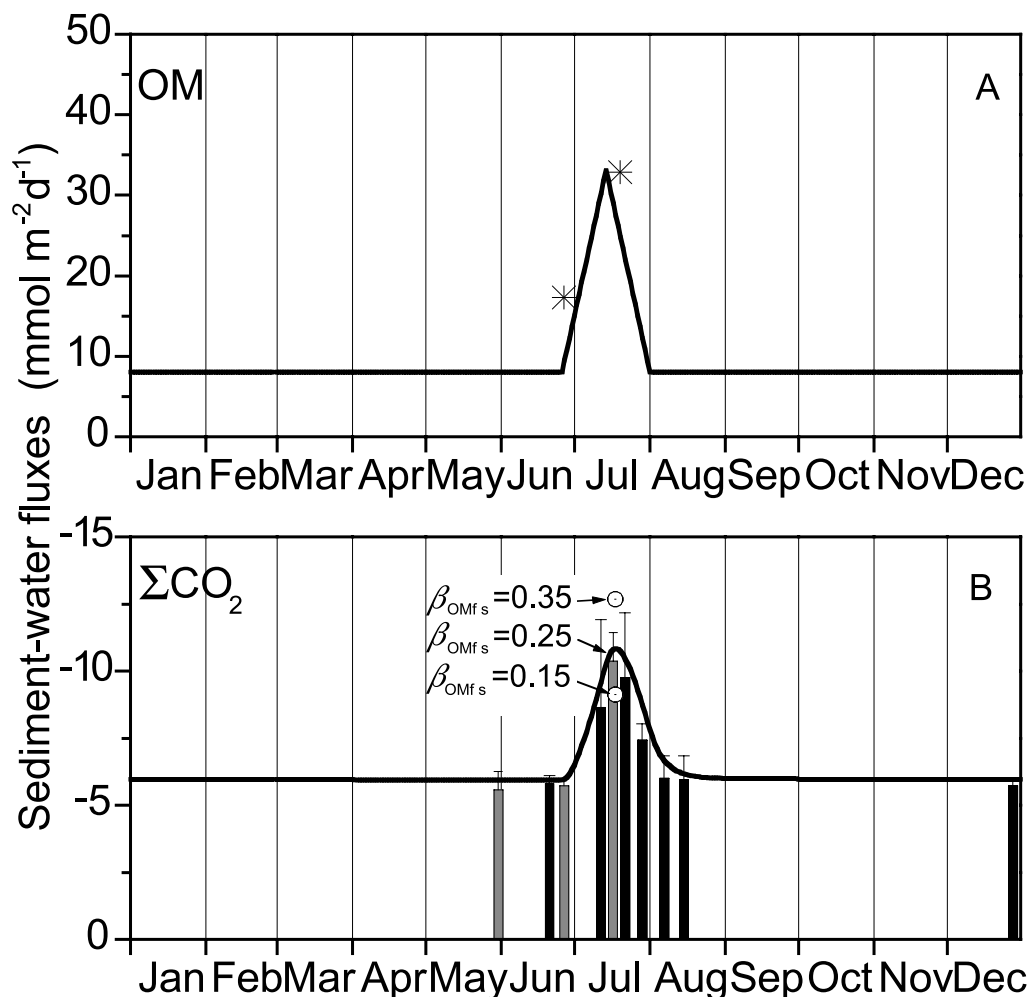


Fig. 10. Determination of the total OM flux supplied to the sediment surface through the annual cycle. (A) The generated total OM flux (line) and two measured values (stars). (B) Simulated and measured  $\Sigma\text{CO}_2$  fluxes through the annual cycle (error bars represent 1 SE,  $n = 6$ ). The black bars represent true measurements and the gray bars are estimated from measured  $\text{O}_2$  fluxes and a linear regression between the fluxes of  $\text{O}_2$  and  $\Sigma\text{CO}_2$  ( $R^2 = 0.81$ ). The two circles represent the maximum  $\Sigma\text{CO}_2$  fluxes in additional simulations with different values of  $\beta_{\text{OMfs}}$ .

(fig. 5). A new comparison, now with the true simulated OM mineralization profile, verified that the good agreement was maintained between the measured and simulated  $\Sigma\text{CO}_2$  profile. This comparison obviously included the dynamic changes through the year of the simulated  $\Sigma\text{CO}_2$  profile (data shown below).

#### Remaining Input for Nitrogen Cycling

At this point in the model application only four parameters were left to be assigned before the nitrogen cycling was also fully parameterized. These parameters were the limiting concentrations,  $[\text{O}_2]_{\text{lim}}$  and  $[\text{NO}_3^-]_{\text{lim}}$ ; the rate constant for the nitrification process,  $K_7$ ; and the C:N ratio. The concentrations  $[\text{O}_2]_{\text{lim}}$  and  $[\text{NO}_3^-]_{\text{lim}}$  were taken from Van Cappellen and others (1993) who estimated order of magnitude values for natural aquatic sediments. The particular values we adopted here were identical to the ones used in the model of Wang and Van Cappellen (1996).



The value of  $K_7$  was derived from site-specific measurements by Rysgaard and others (1998) and steady-state, trial-and-error simulations. Measured concentration profiles of  $O_2$  and  $NH_4^+$ , the two reactants in the nitrification process, were fitted with analytical functions and temporarily imposed in the model as substitutes for the simulated  $O_2$  and  $NH_4^+$  profiles (fig. 11A and 11B). In the trial-and-error simulations, the value of  $K_7$  was then adjusted until the simulated  $NO_3^-$  profile matched the measured profile (fig. 11C).

Three different C:N ratios were reported by Rysgaard and others (1998), a C:N ratio averaging 10.3 and estimated from total amounts of carbon and nitrogen in the sediment (fig. 12A), a C:N ratio of 7.6 estimated from carbon and nitrogen production in bag-incubated sediment samples, and a C:N ratio of 16 estimated from measured carbon and nitrogen fluxes over the sediment-water interface. These values defined a relatively broad range of justifiable C:N ratios to be used in the model. The C:N ratio was found in dynamic trial-and-error simulations in which the ratio was adjusted until a good agreement was obtained between the measured and the simulated  $NH_4^+$  profile (fig. 12B). The time point of these comparisons coincided with the peak of the summer pulse of OM supplied to the sediment surface. Good agreement was obtained with a depth-independent C:N ratio identical to the averaged total C:N ratio reported by Rysgaard and others (1998). It should be noted that if the irrigation parameter for  $NH_4^+$  had been reduced relative to the one determined for  $\Sigma CO_2$  (fig. 5), a higher C:N ratio would have been predicted. For example, a reduction of the irrigation parameter, as the one determined for  $Mn^{2+}$  (fig. 7), would have demanded a C:N ratio of 16 to give a similar good agreement between the measured and simulated  $NH_4^+$  profile. The irrigation parameter for  $NH_4^+$  and the dynamics of the  $NH_4^+$  profile are discussed below.

#### *Remaining Input for Iron and Sulfur Cycling*

With the nitrogen cycling fully parameterized, the variables for the cycling of manganese, iron and sulfur were left to be assigned. In the previous parameterizations we decoupled sections of the model and focused on only one or a few input parameters at a time. This practice generally cannot be applied in the parameterization of the manganese, iron, and sulfur cycles due to their complex linkages through various reactions. However, in this particular model application to the Young Sound sediment, manganese was only present in insignificant quantities relative to iron and sulfur, and this allowed us to temporarily neglect manganese when we parameterized the iron and sulfur cycles. The parameters for these two cycles, 13 in all, were the external flux of  $FeOOH$  ( $J_{FeOOH\ ext}$ ) supplied to the sediment surface; its distribution ( $\beta_{FeOOH}$ ) between the two pools of  $FeOOH$ ; the limiting concentration,  $[FeOOH]_{lim}$ ; the rate constants,  $K_9$ ,  $K_{11}$ ,  $K_{12}$ ,  $K_{14}$ ,  $K_{15}$ ,  $K_{16}$ ,  $K_{17}$ ,  $K_{20}$ ,  $K_{21}$ ; and the concentration,  $[H_2S]_{stop}$ , at which reaction R21 comes to a complete stop. Parameterization of these variables was accomplished through trial-and-error simulations until good agreements were obtained between the simulated and measured mean concentration profiles of  $Fe^{2+}$ , adsorbed  $Fe^{2+}$ ,  $SO_4^{2-}$ ,  $H_2S$ ,  $FeS$ ,  $FeS_2$  including  $S^0$ , and  $FeOOH$ . In addition, a 25/33 percent split of the annual OM mineralization between iron and sulfate reduction estimated by Rysgaard and others (1998) was also used as a guiding value in the parameterization. Given the relatively large number of input variables to the iron and sulfur cycles, it was an obvious advantage to have good starting values for as many variables as possible before we pursued the time-consuming parameterization through trial-and-error simulations. We determined these starting values in the following manner.

All  $Fe^{2+}$  simulated to escape the sediment at the upper boundary is immediately recycled as  $FeOOH$  to the sediment surface. The flux of recycled  $FeOOH$  is calculated in the model and needed no further specification. Furthermore, as a flux of zero is

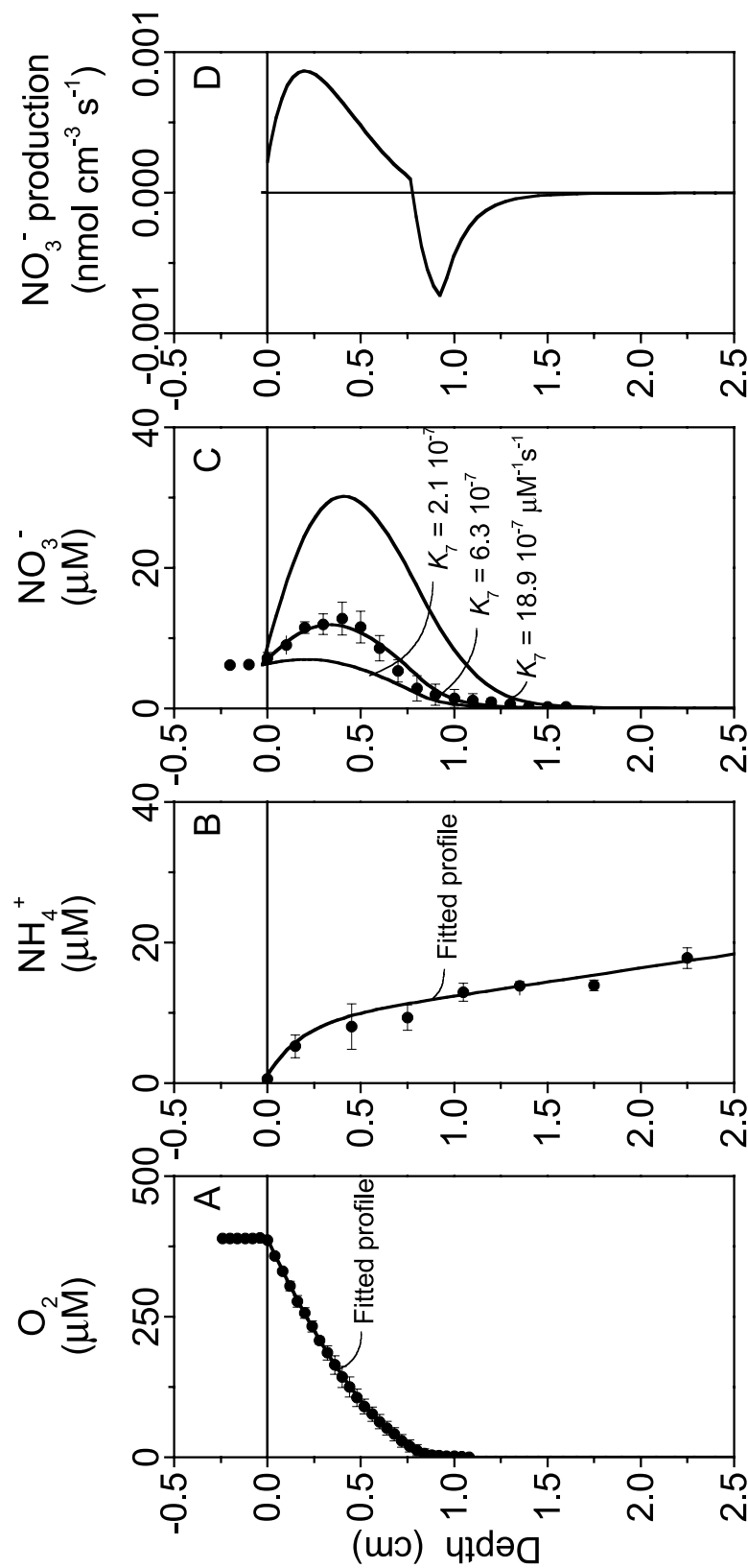


Fig. 11. Determination of the rate constant,  $K_7$ , for the nitrification process. (A) Fit to the measured  $O_2$  profile, which was imposed temporarily in the model (error bars represent  $\pm 1$  SE,  $n = 6$ ). (B) Fit to the measured  $NH_4^+$  profile, also imposed in the model (error bars represent  $\pm 1$  SE,  $n = 3$ ). (C) Measured and simulated  $NO_3^-$  profiles for different values of  $K_7$  (error bars represent  $\pm 1$  SE,  $n = 3$ ). (D) Simulated production of  $NO_3^-$  as a result of nitrification and denitrification.

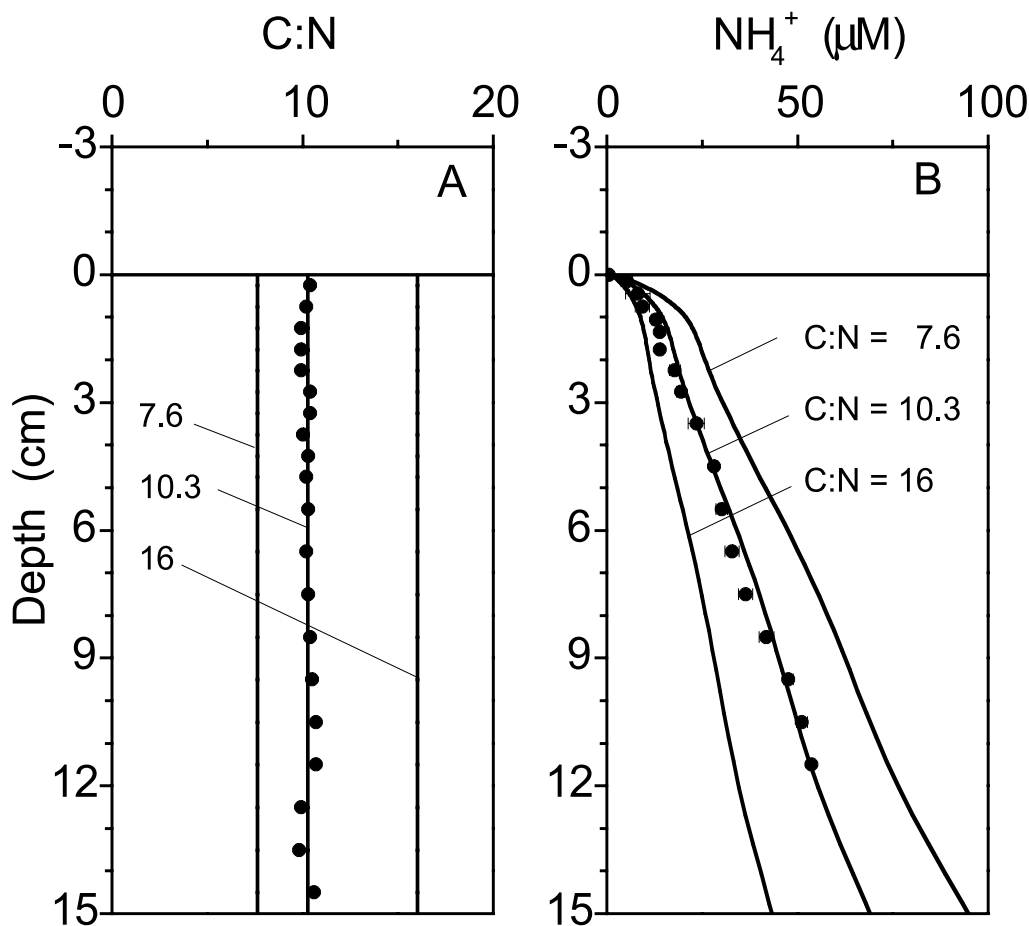


Fig. 12. Determination of the C:N ratio for OM mineralization. (A) Various C:N ratios reported by Rysgaard and others (1998). (B) Measured and simulated  $\text{NH}_4^+$  profiles for the different C:N ratios (error bars represent  $\pm 1$  SE,  $n = 3$ ). A good agreement was obtained for the measured C:N ratio of 10.3.

imposed as the upper boundary condition for  $\text{FeS}$  and  $\text{FeS}_2$ , it is evident from a mass conservation argument that  $J_{\text{FeOOH ext}}$  must equal the burial flux of iron at the lower boundary. This flux consists mainly of adsorbed  $\text{Fe}^{2+}$ , and the solid iron fractions  $\text{FeS}$ ,  $\text{FeS}_2$ , and  $\text{FeOOH}$ . A starting value for  $J_{\text{FeOOH ext}}$  of  $5.2 \times 10^{-4} \text{ nmol cm}^{-2} \text{ s}^{-1}$  was estimated from the sedimentation rate and extrapolated measured concentrations of these iron constituents to the lower boundary (data shown below). Based on fractional distributions of  $\text{FeOOH}$  in other sediments and sedimenting matter (Canfield, 1989; Canfield, 1997),  $\beta_{\text{FeOOH}}$  was given the initial value of 0.5 in an even distribution of the external flux to the iron pools  $\text{FeOOH}_A$  and  $\text{FeOOH}_B$ .

Four reactions involving iron or sulfur concentrations (R9, R12, R14, R15) and also their regulation are identical to ones included in the model of Van Cappellen and Wang (1996). We used their reported rate constants of  $1.1 \times 10^{-6}$ ,  $5.1 \times 10^{-9}$ ,  $2.5 \times 10^{-10}$ , and  $1.9 \times 10^{-9} \mu\text{M}^{-1} \text{ s}^{-1}$  as starting values for  $K_9$ ,  $K_{12}$ ,  $K_{14}$ , and  $K_{15}$ . A starting value of  $[\text{FeOOH}]_{\text{lim}}$  was also chosen based on the study of Van Cappellen and Wang (1996), who included only one pool of  $\text{FeOOH}$  in their model and used values of  $[\text{FeOOH}]_{\text{lim}}$  ranging from 65000 to 100000  $\text{nmol g}^{-1}$ . Because we utilized two pools for  $\text{FeOOH}$  a lower value of  $[\text{FeOOH}]_{\text{lim}}$  of 50000  $\text{nmol g}^{-1}$  was chosen.

Order of magnitude values for several of the remaining rate constants were derived from interpretations of measured  $\text{FeS}_2$  and  $\text{FeS}$  profiles performed with an

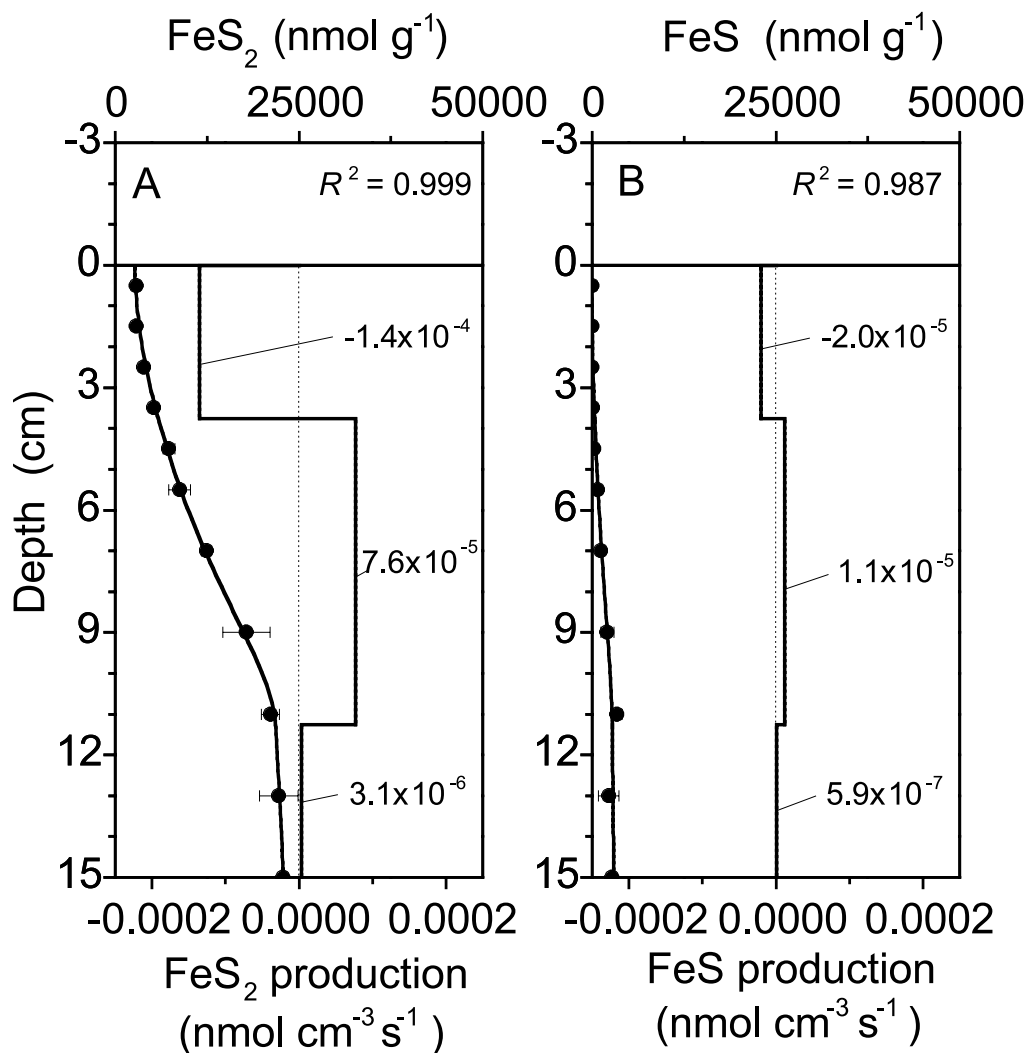


Fig. 13. Profile interpretations of measured FeS<sub>2</sub> and FeS profiles performed with a modified version of PROFILE (Berg and others, 1998; error bars represent  $\pm$  SE,  $n = 3$ ). From the calculated production-consumption rates, initial values for the rate constants  $K_{11}$ ,  $K_{16}$ , and  $K_{17}$  were estimated.

extended version of the procedure, PROFILE, of Berg and others (1998) that can take solid species into account (fig. 13). The interpretations, which were performed with a flux of zero and a zero concentration gradient imposed as upper and lower boundary conditions, resulted in good fits to the measured profiles as reflected in the  $R^2$  values of 0.999 and 0.987 (fig. 13). As expressed in the primary and secondary redox reactions, the net production of almost all species is the result of many reactions. FeS<sub>2</sub> is different in the sense that FeS<sub>2</sub> can only be produced through one single reaction (R16) and consumed in another (R17). Given the reactants in these reactions (FeS, S<sup>0</sup> and FeS<sub>2</sub>, O<sub>2</sub>), their overlap in depth-to-depth comparisons is likely to be relatively small. As a result, the production of FeS<sub>2</sub> found through interpretation of the FeS<sub>2</sub> profile (fig. 13A) can be attributed exclusively to reaction R16, while the consumption can be attributed to reaction R17. The production of FeS<sub>2</sub> was predicted to occur over the 3.75 to 15 centimeter depth interval (fig. 13A) with an average rate of  $5.2 \times 10^{-5}$  nmol cm<sup>-3</sup> s<sup>-1</sup>. In the same depth interval, the average measured FeS concentration (fig.

13B), one of the reactants in reaction R16, equaled  $1800 \text{ nmol g}^{-1}$ . The other reactant,  $\text{S}^0$ , was not measured in the Young Sound sediment, but other studies have reported ratios of  $[\text{S}^0]:[\text{FeS}]$  of approximately 0.1 (Sørensen and Jørgensen, 1987; Thamdrup and others, 1994b). Based on these values and the rate law for reaction R16,  $K_{16}$  was estimated to be  $2.0 \times 10^{-10} \text{ cm}^3 \text{ nmol}^{-1} \text{ s}^{-1}$ .

The interpretation of the  $\text{FeS}_2$  profile also predicted a consumption of  $1.4 \times 10^{-4} \text{ nmol cm}^{-3} \text{ s}^{-1}$  in the 0 to 3.75 centimeter depth interval, which extended further down into the sediment than the measured  $\text{O}_2$  penetration depths of 1 to 1.5 centimeters (fig. 9). This apparent inaccuracy in the profile interpretation might be the result of the relatively coarse depth resolution of the measured  $\text{FeS}_2$  concentrations. It is also possible, however, that  $\text{FeS}_2$  was actually consumed at notable rates at these depths, driven by  $\text{O}_2$  supplied by irrigation. In the 0 to 3.75 centimeter depth interval, the measured  $\text{FeS}_2$  concentration averaged  $3700 \text{ nmol g}^{-1}$  and the  $\text{O}_2$  concentration was estimated from measured  $\text{O}_2$  profiles to be on the order of  $50 \text{ } \mu\text{M}$ . Based on these values and the rate law for reaction R17,  $K_{17}$  was estimated to be  $4.8 \times 10^{-10} \text{ } \mu\text{M}^{-1} \text{ s}^{-1}$ .

As expressed in the secondary redox reactions, the entire production of  $\text{FeS}_2$  originates from  $\text{Fe}^{2+}$  and  $\text{H}_2\text{S}$  reacting first to give  $\text{FeS}$  (R11), and then by the reaction of  $\text{FeS}$  with  $\text{S}^0$  (R16). This implies that the production of  $\text{FeS}$  in reaction R11 must equal the production of  $\text{FeS}_2$  in reaction R16 plus additional contributions covering the burial loss of  $\text{FeS}$  and the consumption of  $\text{FeS}$  through reaction R15. These two contributions were estimated in the interpretation of the measured  $\text{FeS}$  profile (fig. 13B) to be  $9.5 \times 10^{-6}$  and  $7.6 \times 10^{-5} \text{ nmol cm}^{-2} \text{ s}^{-1}$ . Comparisons of these values with the total  $\text{FeS}_2$  production of  $5.8 \times 10^{-4} \text{ nmol cm}^{-2} \text{ s}^{-1}$  justified the use of the  $\text{FeS}_2$  production rate as a production rate for  $\text{FeS}$  in an estimation of the rate constant for reaction R11. In the 3.75 to 15 centimeter depth interval, the measured  $\text{Fe}^{2+}$  concentration, a reactant in reaction R11, averaged  $180 \text{ } \mu\text{M}$ . The other reactant,  $\text{H}_2\text{S}$ , was found in concentrations near or below the detection limit ( $< 1 \text{ } \mu\text{M}$ ) at all depths by Rysgaard and others (1998). Despite these low concentrations,  $\text{H}_2\text{S}$  played a key role in the cycling of iron and sulfur, and the low  $\text{H}_2\text{S}$  concentrations reflect that  $\text{H}_2\text{S}$  was consumed at the same rate at which it was produced. Here we assumed temporarily that the  $\text{H}_2\text{S}$  concentrations were on the order of  $1 \text{ } \mu\text{M}$ . Based on these values and the rate law for reaction R11,  $K_{11}$  was estimated to  $4.5 \times 10^{-7} \text{ } \mu\text{M}^{-1} \text{ s}^{-1}$ .

A literature survey did not yield any information on possible starting values of  $K_{20}$  and  $K_{21}$  to be used in the parameterization of the iron and sulfur cycles. A value of  $1.0 \times 10^{-10} \text{ s}^{-1}$  was chosen arbitrarily and used for both rate constants.

In studies with pure bacterial cultures, Thamdrup and others (1993) and Finster and others (1998) have shown that disproportionation of  $\text{S}^0$  (R21) is inhibited fully at  $\text{H}_2\text{S}$  concentrations on the order of  $100 \text{ } \mu\text{M}$ . Under realistic field conditions, significantly poorer growth conditions are expected. Thus, we chose a starting value of  $10 \text{ } \mu\text{M}$  for the stop concentration,  $[\text{H}_2\text{S}]_{\text{stop}}$ , in the regulation of this process.

With these 13 parameter values for the iron and sulfur cycling, which were all subject to adjustments, the entire model was run until quasi-stationary results were obtained on a year-to-year basis. Starting with a concentration of zero for all species in the first simulation, several thousand simulated years were needed to strictly meet this requirement. The slow build-up of the  $\text{FeOOH}$  concentrations caused by the relatively small external flux of  $\text{FeOOH}$  required this long simulation time. Other parts of the model, such as the transport of  $\text{O}_2$  in the upper sediment layer, had a significantly faster dynamic that demanded a time step of one hour. Subsequent simulations to this first one were performed with the concentrations from the previous simulations as starting values, which made it possible to obtain quasi-stationary results on a year to year basis after 20 to 100 years of simulated time. These relatively long simulated times combined with a rather small time

step did not lead to excessive computation times because the numerical solution we used was specially optimized with respect to speed (see above). This allowed us to simulate one year in less than three seconds on a 700 MHz Pentium PC.

Variations in simulated concentration profiles of iron and sulfur constituents within the year were barely detectable, which made the time of comparison between measured and simulated profiles unimportant. This insignificant seasonal variation in the presence of a constant water temperature was the result of the almost constant OM concentrations and lability at depths where iron and sulfate reduction occurred, and also to some degree the constant external flux of FeOOH imposed to the sediment surface. The simulated profiles in the first simulation matched most of the measured profiles relatively well (fig. 14), with the largest deviations found for the FeS and FeS<sub>2</sub>. Clearly, the concentration levels simulated for FeS were too high, while levels for FeS<sub>2</sub> were found to be too low. From the reactions of the iron and sulfur cycles, it was evident that this imbalance could be corrected if reaction R16 was stimulated by higher concentrations of S<sup>0</sup>. The consumption of S<sup>0</sup> through reaction R21 was simulated to be insignificant, which suggests that higher S<sup>0</sup> concentrations should be obtained by stimulating reaction R14, the only possible source for additional S<sup>0</sup>. This was done in the second simulation where  $K_{14}$  was increased by a factor of five. The adjustment of  $K_{14}$  had the desired effect (fig. 14) on the FeS and FeS<sub>2</sub> profiles, but resulted in too high concentration levels of Fe<sup>2+</sup> and Fe<sub>ads</sub><sup>2+</sup>. In a third simulation, the rate constant for reaction R20 was increased to reduce the Fe<sup>2+</sup> production in reaction R4. The adjustments of input parameters for the iron and sulfur cycles were continued through many trial-and-error simulations until good agreements were obtained between simulated and measured results (data shown below). During this process, 9 of the 13 parameters were adjusted from their initial values.

#### *Remaining Input for Manganese Cycling*

At this point in the model application only the parameters for the manganese cycle were left to be assigned. These parameters, 7 in all, were the external flux of MnO<sub>2</sub> ( $J_{\text{MnO}_2 \text{ ext}}$ ) supplied to the sediment and its distribution ( $\beta_{\text{MnO}_2}$ ) between the two pools of MnO<sub>2</sub>, the limiting concentration, [MnO<sub>2</sub>]<sub>lim</sub>, and the rate constants  $K_8$ ,  $K_{10}$ ,  $K_{13}$ ,  $K_{19}$ . The parameterization was done following the same practice as for the iron and sulfur cycles. As a result of the fewer input parameters for the manganese cycle this last step in the model parameterization was significantly less challenging than the one for the iron and sulfur cycling. In addition, some starting values for the parameterization were chosen from the known parameters of the iron cycle. For example, the rate constant for the transformation of MnO<sub>2A</sub> to MnO<sub>2B</sub> (R19) initially was given the values as found for FeOOH (R20), and the rate constant for Mn<sup>2+</sup> reactions with O<sub>2</sub> (R8) initially was given a value that was a factor of 100 smaller than the rate constant for Fe<sup>2+</sup> reactions with O<sub>2</sub> (R9). For the two reactions, reaction R10 and R13, starting values were taken from the model applications of Van Cappellen and Wang (1996).

### SIMULATED AND MEASURED RESULTS

#### *Sensitivity Analysis*

Table 3 contains all final values of input parameters to the model for its application to the Young Sound sediment. As illustrated clearly in many of the figures showing elements of the parameterization, the model is sensitive to variations in most input parameters (figs. 5, 7 to 12, and 14). This is seen as a positive characteristic as it increases the precision in the value assignment. However, for a smaller subset of input parameters, imposed variations seemed only to have little effect on simulated results, and this obviously increases the uncertainties of these parameter values. In order to quantify these uncertainties more systematically, a sensitivity analysis was performed for 31 selected input parameters (fig.



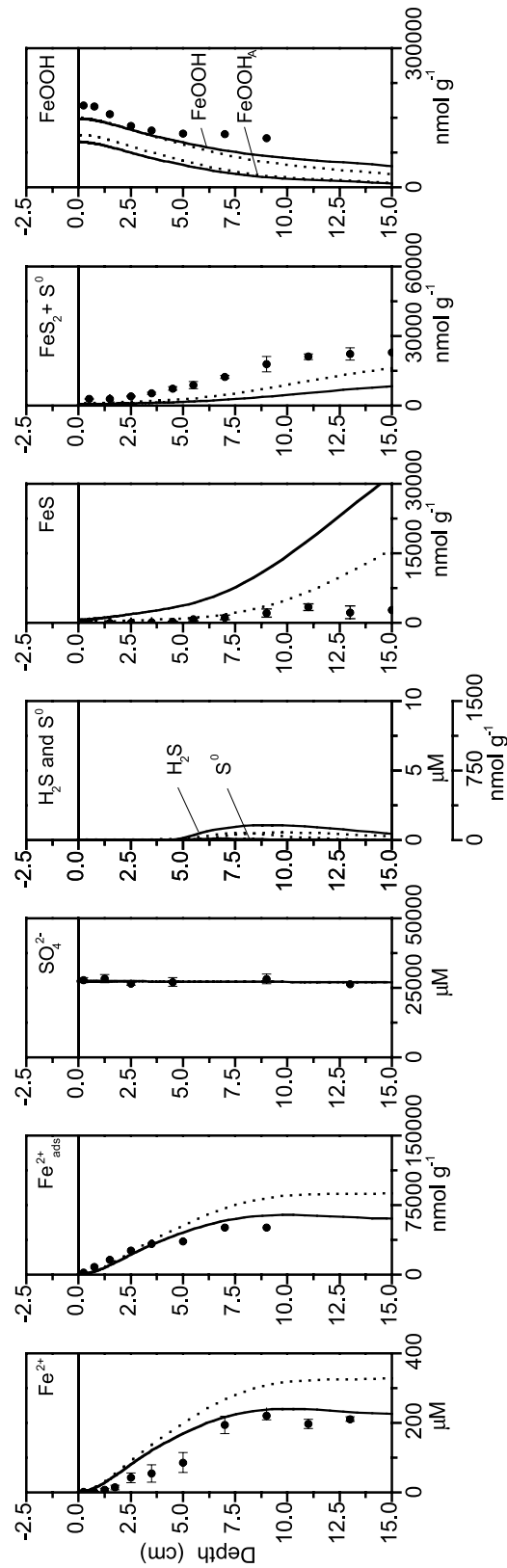


Fig. 14. Comparisons of simulated and measured profiles during the parameterization of the iron and sulfur cycles (error bars represent  $\pm 1$  SE,  $n = 3-6$ ). Based on results of the first simulation (solid lines), the rate constant  $K_{14}$  was increased by a factor of five in the second simulation (dotted lines). The FeOOH profile represents the sum of the pools  $\text{FeOOH}_A$  and  $\text{FeOOH}_B$ .

15). These parameters were changed, one at a time, in simulations that were run until quasi-stationary results were obtained on a year-to-year basis. The changes imposed were 5 percent for all input parameters, except for  $\alpha_{\text{Fe}}$  which was increased from its original value of  $0 \text{ year}^{-1}$  to 0.05 times the  $\alpha$  determined for  $\Sigma\text{CO}_2$  (fig. 5). Two variables were defined as representative measures of the model sensitivity, one expressing the maximum relative change in depth-to-depth comparisons of all concentration profiles, and one expressing the maximum relative change in comparisons of all depth-integrated reaction rates. Expressed in percentages, these variables are given by

$$S_1 = 100 \frac{\max(|C - C_{\text{ref}}|)}{\max(C_{\text{ref}})}$$

$$S_2 = 100 \frac{\int_0^L V \, dx - \int_0^L V_{\text{ref}} \, dx}{\int_0^L V_{\text{ref}} \, dx} \quad (4)$$

where the notation *ref* is used for simulated results obtained with the original parameters values listed in table 3.

Disproportionation of  $\text{S}^0$  is a recently discovered reaction in coastal sediments (Canfield and Thamdrup, 1994) and its importance in sulfur transformations is not fully realized. The effect of this process was revealed in a simulation, run until quasi-stationary results were obtained on a year-to-year basis, where disproportionation of  $\text{S}^0$  was neglected while all other input parameters were unchanged from their original values listed in table 3 (fig. 16).

#### Concentration-Depth Profiles

The majority of the simulated concentration-depth profiles based on the completed model parameterization (table 3) are shown in figure 17 in comparison with measured profiles where they exist. In each panel, two sets of simulated profiles are shown representing the maximum seasonal variations through the simulated year. These variations are relatively limited and only visible for the profiles of  $\text{O}_2$ ,  $\Sigma\text{CO}_2$ ,  $\text{NH}_4^+$ , and  $\text{NO}_3^-$ .

#### Sediment-Water Fluxes

Simulated sediment-water fluxes through the year are shown in figure 18 in comparison with measured fluxes. Irrigation played a significant role in the exchange of all solutes between the sediment and the water column, in agreement with the findings of Wang and Van Cappellen (1996). Irrigation contributed 61, 39, and 82 percent of the total fluxes of  $\Sigma\text{CO}_2$ ,  $\text{O}_2$ , and  $\text{NH}_4^+$ , respectively, shown in figure 18. For  $\text{NO}_3^-$ , the combined flux due to molecular diffusion and bioturbation equaled  $-0.12 \text{ mmol m}^{-2} \text{ d}^{-1}$  and was directed out of the sediment, while the irrigative flux of  $0.024 \text{ mmol m}^{-2} \text{ d}^{-1}$  supplied the sediment with  $\text{NO}_3^-$  as a result of a higher concentration in the water column relative to the sediment as a whole.

#### Reaction Rates

Simulated OM mineralization by oxic decomposition; denitrification; and manganese, iron, and sulfate reduction are shown in figure 19 in comparison with measured rates where they exist. As expected, the simulated seasonal dynamic was most pronounced for reactions occurring closest to the sediment surface. The peak of the oxic decomposition (fig. 19A) in mid-July was more than three times higher than its base

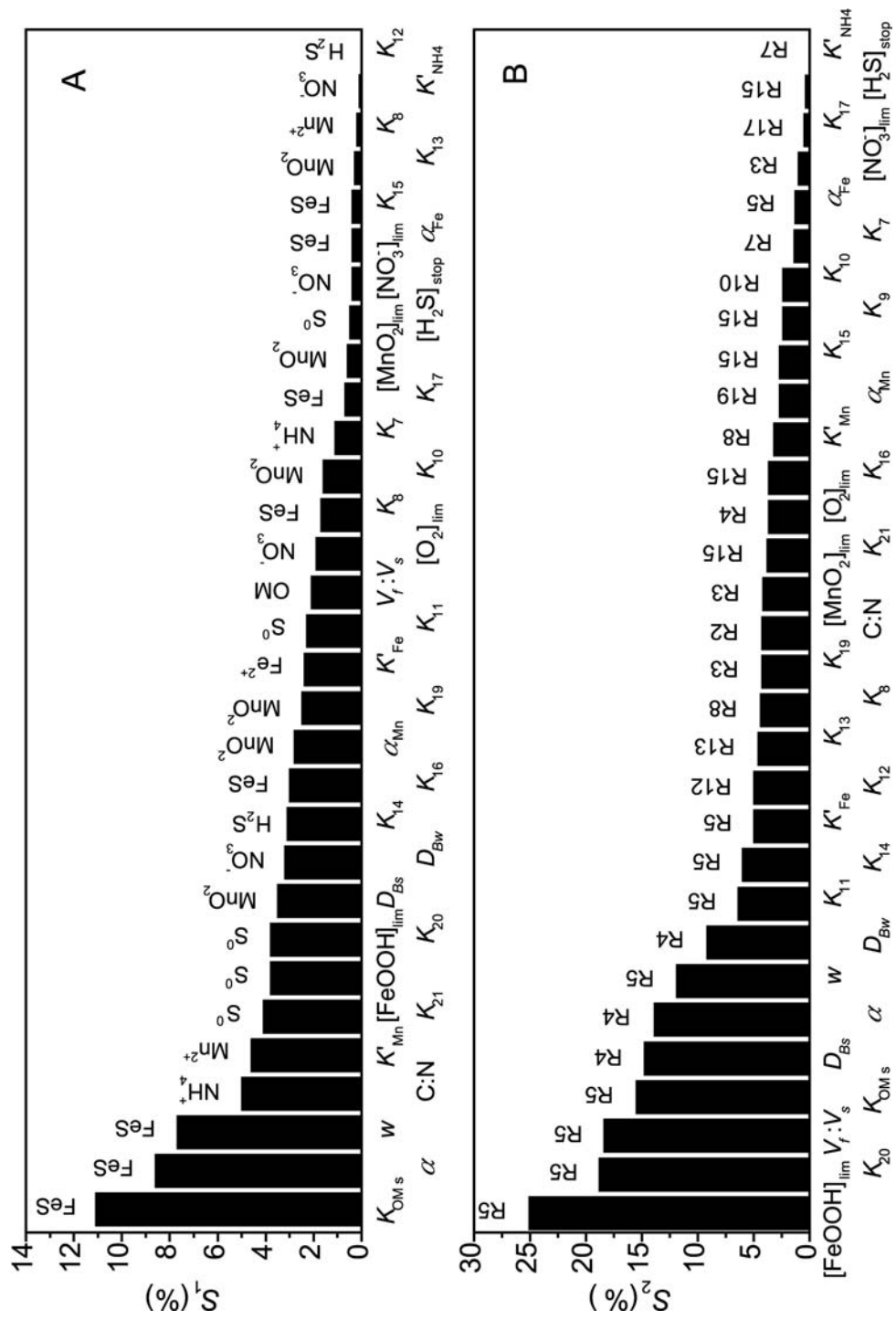


Fig. 15. Sensitivity analysis for 31 selected input parameters. The parameters were changed one at a time in simulations from which the maximum effect on concentration profiles (A) and on reaction rates (B) was determined. The changes imposed were 5 percent for all input parameters, except for  $\alpha_{\text{Fe}}$  which was increased from  $0 \text{ year}^{-1}$  to 0.05 times  $\alpha$  for  $\Sigma\text{CO}_2$  (fig. 5). The most affected concentration profile (A) and reaction rate (B) for each changed parameter are listed above the bars.

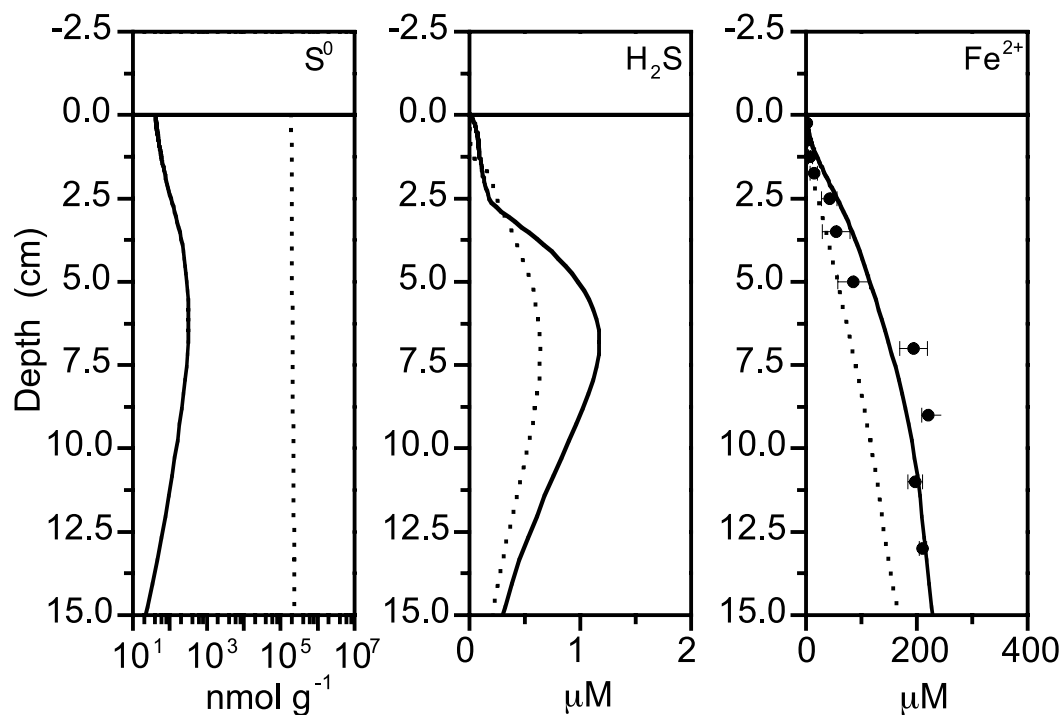


Fig. 16. Simulated effect on selected profiles when excluding  $S^0$  disproportionation ( $K_{21} = 0$ , dotted line). All other input parameters have their final value as listed in table 3. Note the logarithmic x-axis for  $S^0$ .

level, while the sulfate reduction appeared to be constant throughout the year (fig. 19C). This latter result is in agreement with the measured sulfate reduction rates, which showed relatively large variations but exhibited no clear seasonal dynamic.

Simulated OM mineralization by oxic decomposition; denitrification; and iron and sulfate reduction are shown in figure 20, as a function of depth, in comparison with measured rates where they exist. The simulated rates are valid for mid July where the mineralization reached its maximum. Iron reduction rates were measured at this time, and the sulfate reduction rates represent multiple measurements that were averaged, because no clear seasonal dynamic was identified (fig. 20C). The pulse of relatively fresh OM supplied to the sediment surface caused the slightly uneven shape of the simulated iron reduction profile near its maximum (fig. 20B). The simulated iron reduction profile, and in particular the sulfate reduction profile, matched the measured data well. As the result of  $O_2$  and  $NO_3^-$  supplied by irrigation, the simulated oxic decomposition and denitrification (fig. 20A) extended to relatively large sediment depths.

#### Pathways and Cycles

Simulated pathways of  $O_2$  consumption, and the cycling of carbon, nitrogen, manganese, iron, and sulfate are shown in figures 21 and 22. All contributions, shown as arrows, represent annual values and can be linked to specific reactions in table 2 from the reactants written above or below the arrows. The distribution of the annual OM mineralization between oxic decomposition; denitrification; and manganese, iron, and sulfate reduction as estimated by Rysgaard and others (1998) and simulated by this model are shown in figure 23.

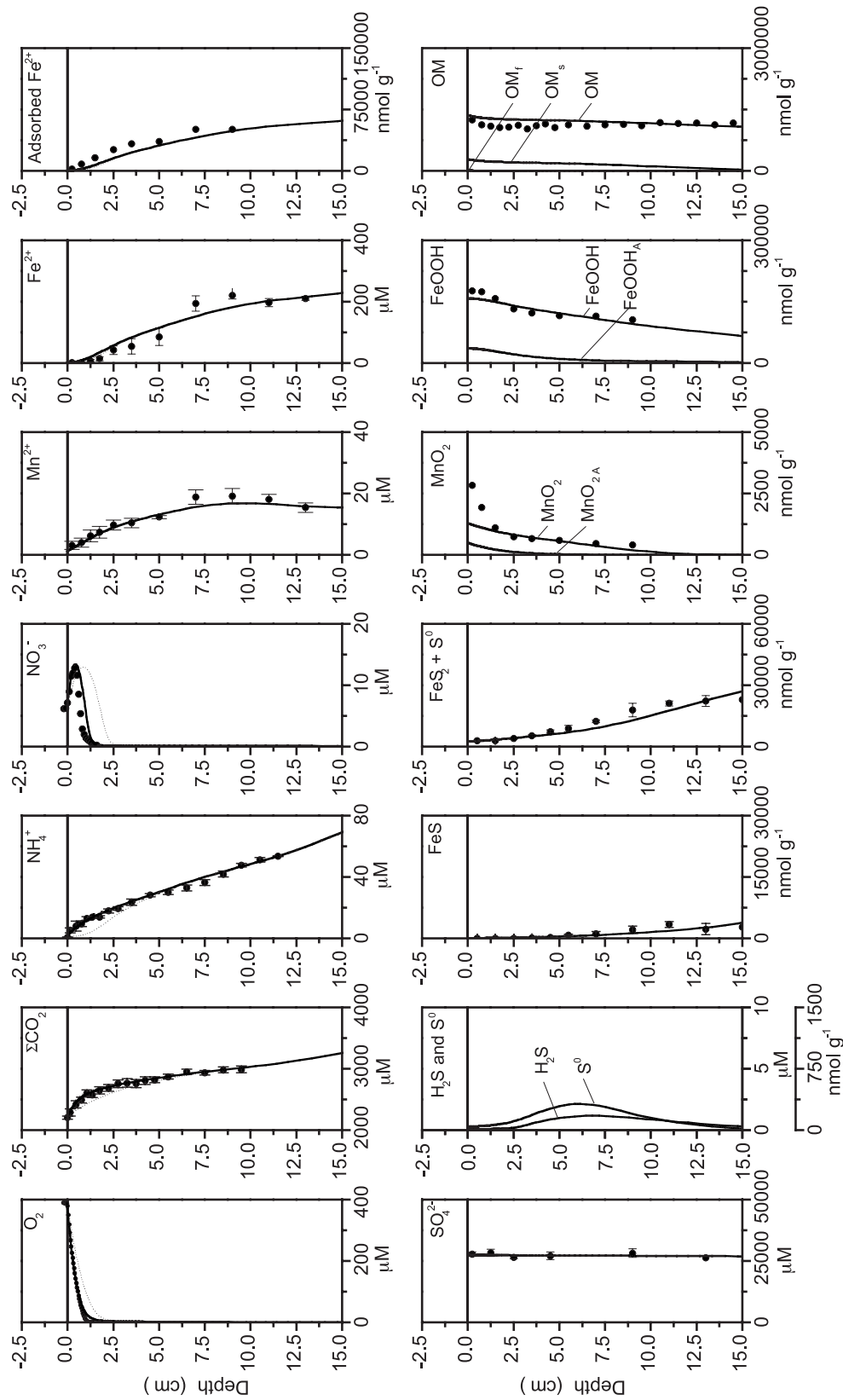


Fig. 17. Measured and simulated profiles for most species included in the model (error bars represent  $\pm 1$  SE,  $n = 3-18$ ). The simulated profiles represent a simulation where all input parameters have their final value as listed in table 3. The measured profiles represent averages of profiles measured primarily through the short summer period. Two sets of simulated profiles are shown, one representing the time when the OM flux peaked (mid-July, solid lines), and one representing the time immediately before the summer pulse of OM (late June, dotted lines). The  $\text{MnO}_2$ , FeOOH and OM profiles represent the sum of the pools utilized for these solid constituents.

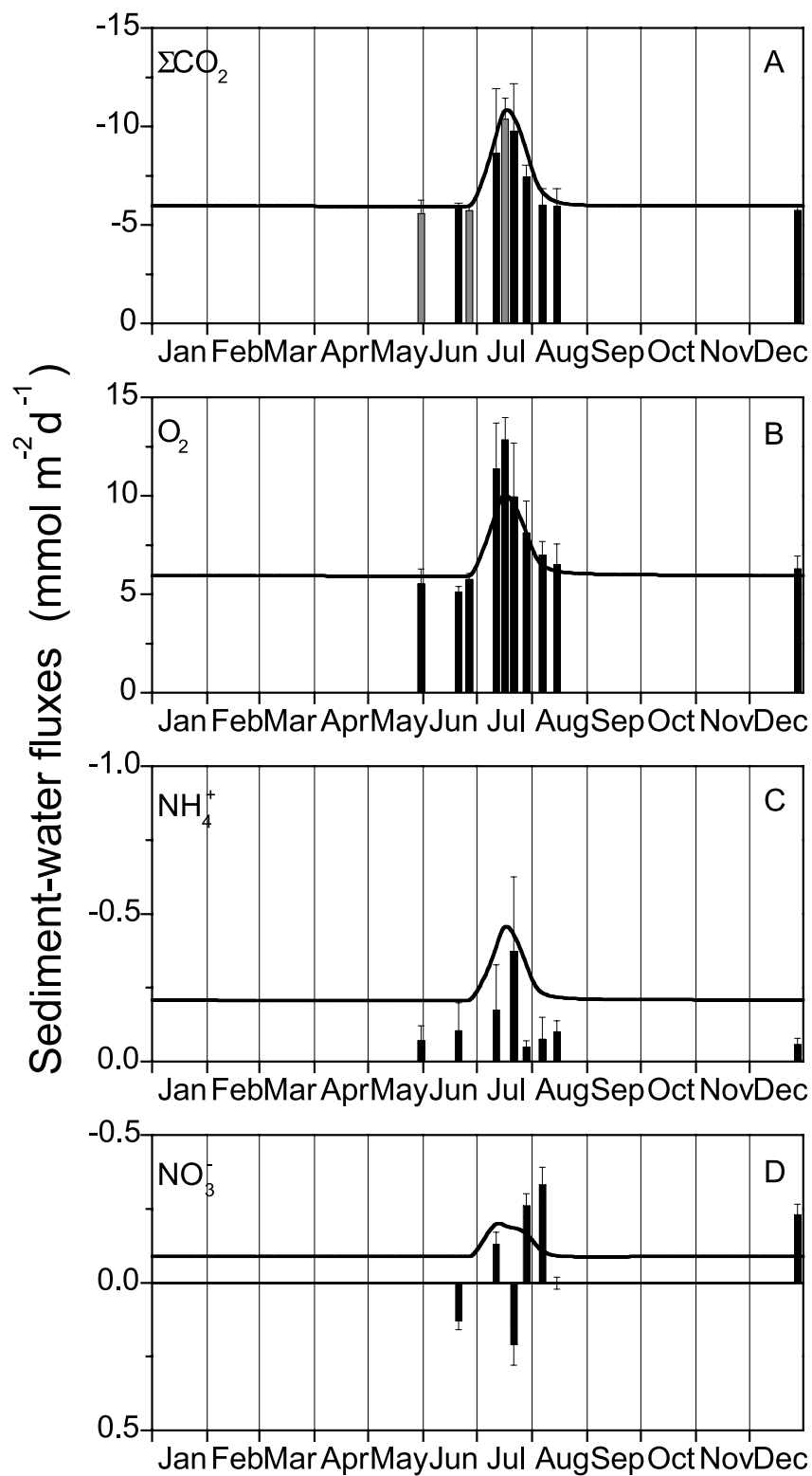


Fig. 18. Measured and simulated sediment-water fluxes through the year (error bars represent 1 SE,  $n = 6$ ).



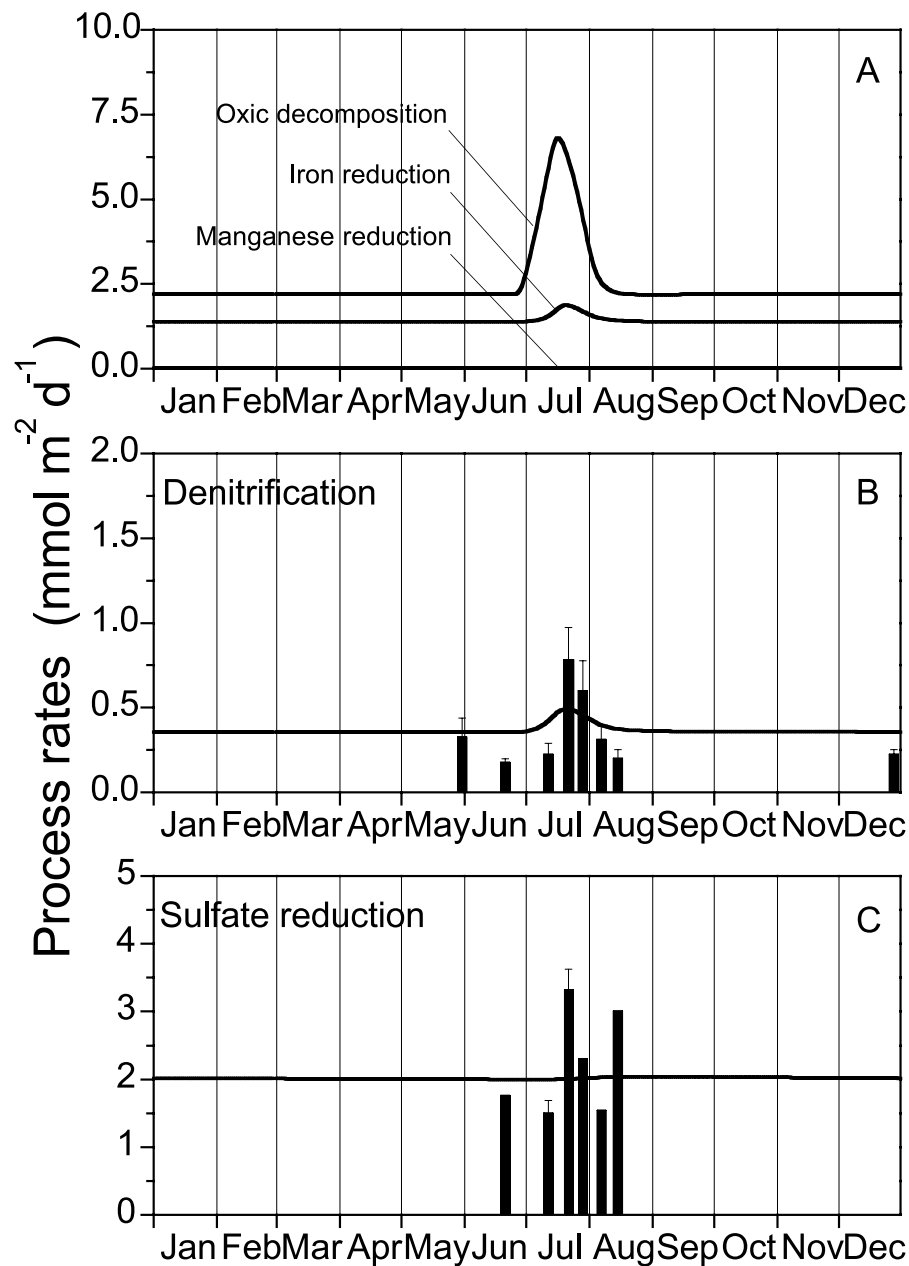


Fig. 19. Simulated and measured process rates of OM mineralization distributed on oxic decomposition; denitrification; and manganese, iron, and sulfate reduction (error bars represent 1 SE,  $n = 3-5$ ).

## DISCUSSION

### *Comparison with Site-Specific Measurements*

The model successfully simulated a large array of variables that were measured through the annual cycle in the Young Sound sediment by Rysgaard and others (1998). These variables include concentration profiles of  $\text{O}_2$ ,  $\Sigma\text{CO}_2$ ,  $\text{NH}_4^+$ ,  $\text{NO}_3^-$ ,  $\text{Mn}^{2+}$ ,  $\text{Fe}^{2+}$ , adsorbed  $\text{Fe}^{2+}$ ,  $\text{SO}_4^{2-}$ ,  $\text{H}_2\text{S}$ ,  $\text{FeS}$ ,  $\text{FeS}_2$ ,  $\text{MnO}_2$ ,  $\text{FeOOH}$ , OM (fig. 17); sediment-water fluxes of  $\Sigma\text{CO}_2$ ,  $\text{O}_2$ ,  $\text{NH}_4^+$ ,  $\text{NO}_3^-$  (fig. 18); depth-integrated process rates of denitrifica-

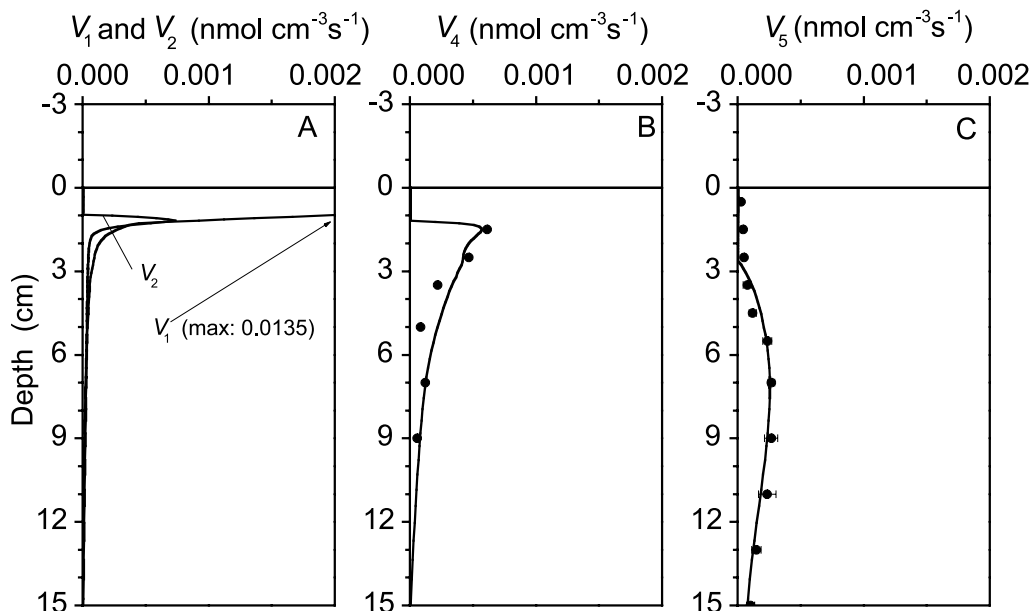


Fig. 20. Simulated and measured process rates of OM mineralization as a function of depth (error bars represent  $\pm 1$  SE,  $n = 6$ ). All simulated rates are shown for the time when the OM flux peaked (Mid-July).

tion and sulfate reduction (fig. 19); and depth profiles of iron and sulfate reduction rates (fig. 20). Generally, the model reproduced these variables with accuracy within error estimates ( $\pm 1$  SE) derived from replicate measurements. In addition, the model also successfully predicted the annual distribution of OM mineralization on oxic decomposition; denitrification; and manganese, iron, and sulfate reduction within a few percent of the distribution estimated by Rysgaard and others (1998) (fig. 23).

While these successful modeling results are not seen as a proof that the reactions and their associated kinetics included in the model provide a full and accurate description of the biogeochemistry of the Young Sound sediment, they are a strong indication that our perception is correct about which reactions are important and how they are regulated. Our results further support the notion that processes catalyzed by natural bacterial communities can be adequately described by simplified reaction kinetics that do not explicitly include bacterial biomass.

The simulated concentration profiles showed little seasonal variation, which was visible only for  $O_2$ ,  $\Sigma CO_2$ ,  $NH_4^+$ , and  $NO_3^-$  (fig. 17). For  $O_2$  and  $NO_3^-$ , smaller penetration depths were simulated during the elevated summer supply of OM to the sediment. For the same time period, slightly elevated concentrations in the top 2 centimeters of the sediment were found for  $\Sigma CO_2$  and  $NH_4^+$ . These limited seasonal variations, characteristic for the simulated profiles, were in line with those of the measured profiles for which no distinctive seasonal patterns could be discerned above the background of natural spatial variations. For that reason, all measured profiles in figure 17, with one exception, represent an average of all profiles measured throughout the year that were generally determined at the same times as the sediment-water fluxes (fig. 18). The measured  $NO_3^-$  profile was determined only for one point in time close to the summer peak supply of OM to the sediment (fig. 10). In that case, the simulated  $NO_3^-$  profile also agreed well with the measured one.

The most obvious deviation between the simulated and measured profiles was found for  $MnO_2$  in the top 1 to 1.5 centimeters of the sediment (figs. 7 and 17). The measured distribution suggests a significant consumption of  $MnO_2$  immediately below the oxic zone, but such consumption was not reflected in the measured distribution of

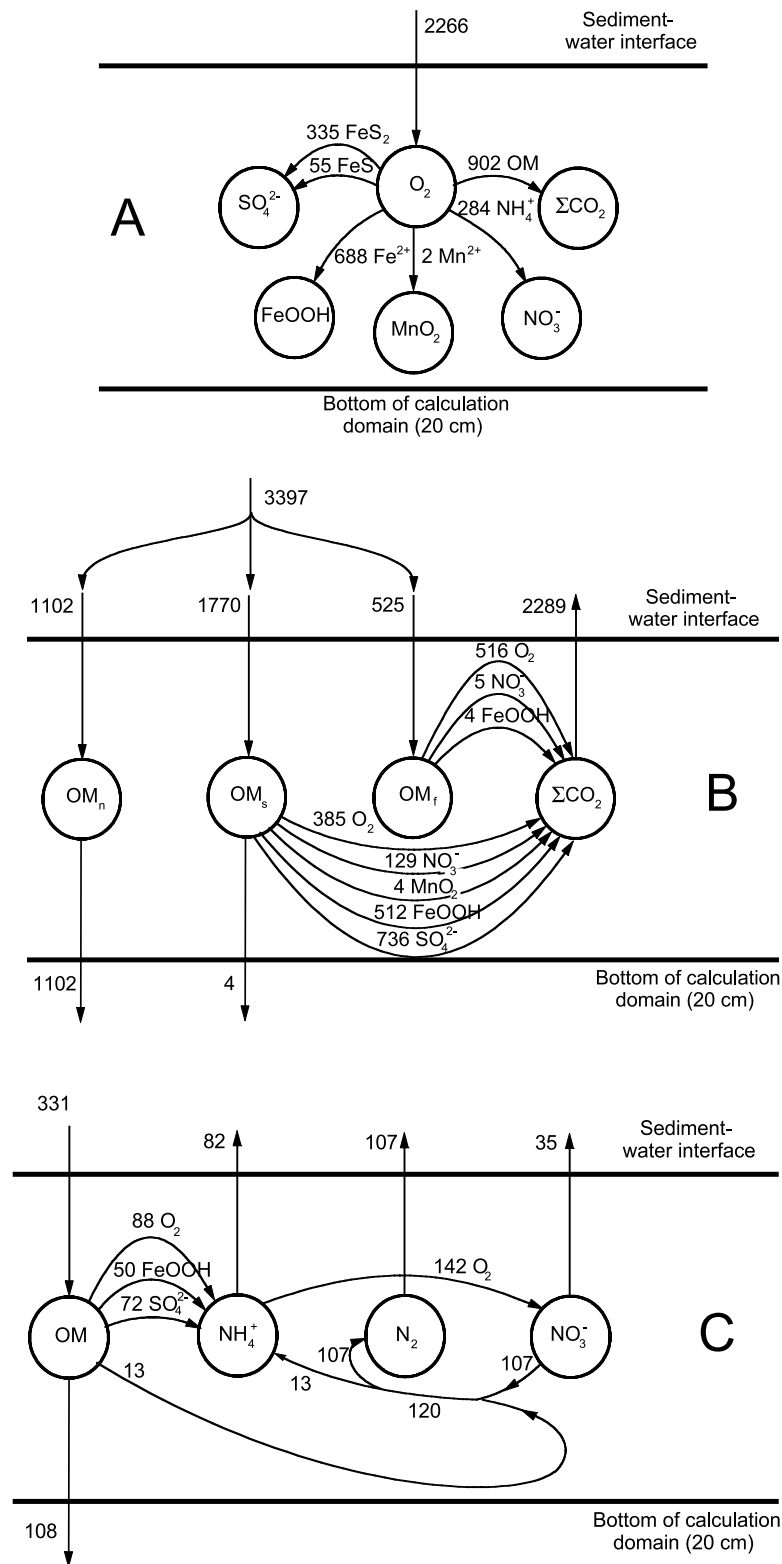


Fig. 21. Pathways of simulated annual oxygen consumption (A, in  $\text{mmol O}_2 \text{ m}^{-2} \text{ year}^{-1}$ ), carbon cycling (B, in  $\text{mmol C m}^{-2} \text{ year}^{-1}$ ), and nitrogen cycling (C, in  $\text{mmol N m}^{-2} \text{ year}^{-1}$ ). Only contributions other than zero are shown. (Any small imbalance in the budgets shown in the figure is due to rounding all values to the nearest integer.)

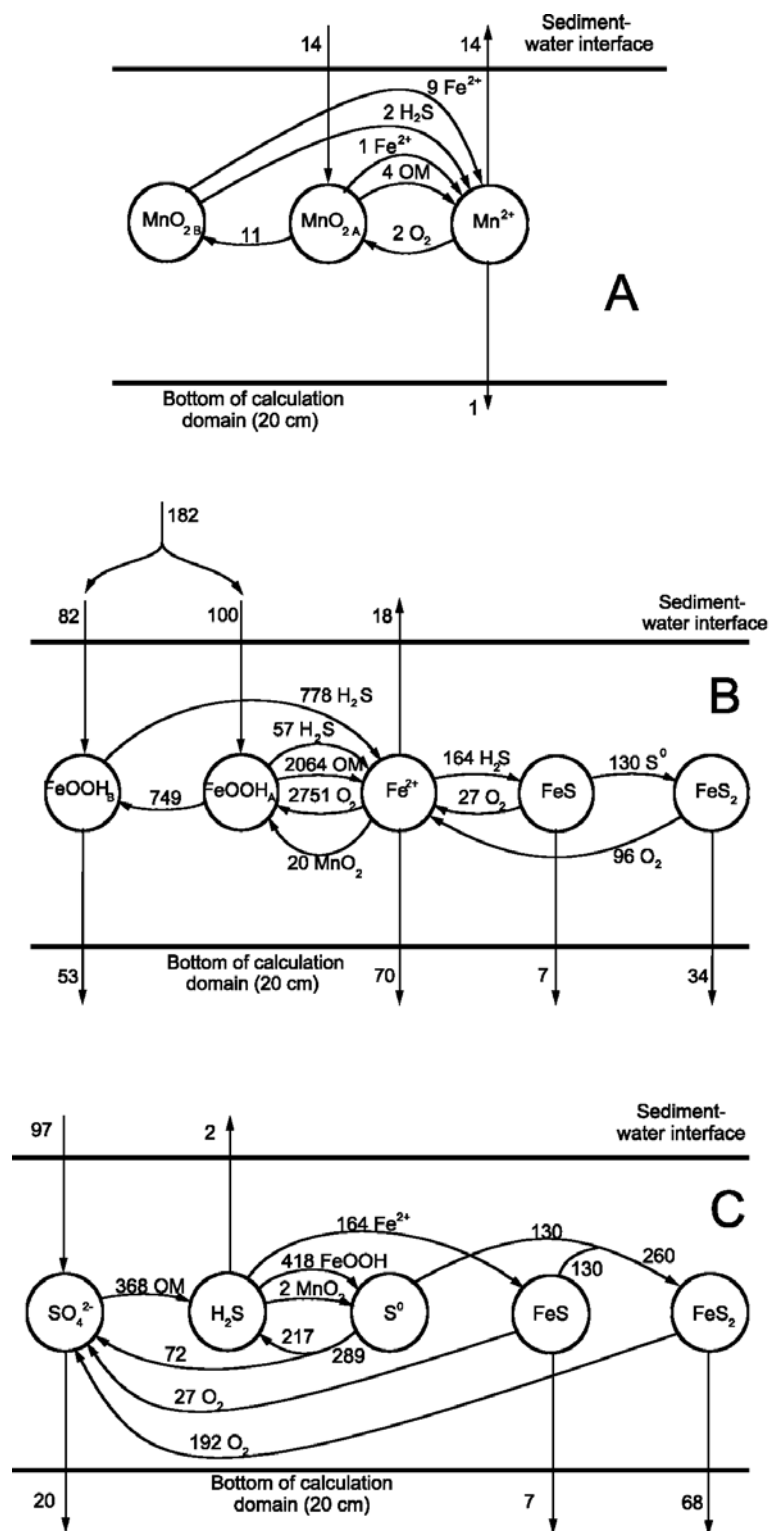


Fig. 22. Pathways of simulated annual manganese cycling (A, in  $\text{mmol Mn m}^{-2} \text{ year}^{-1}$ ), iron cycling (B, in  $\text{mmol Fe m}^{-2} \text{ year}^{-1}$ ), and sulfur cycling (C, in  $\text{mmol S m}^{-2} \text{ year}^{-1}$ ). Only contributions other than zero are shown. (Any small imbalance in the budgets shown in the figure is due to rounding all values to the nearest integer.)

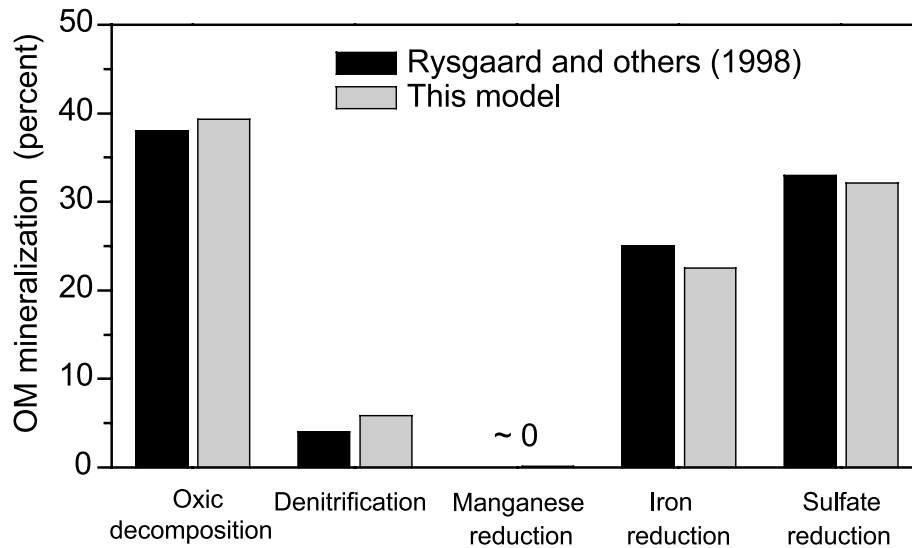


Fig. 23. Distribution of annual OM mineralization between the different primary redox reactions estimated by Rysgaard and others (1998) and simulated by this model.

$\text{Mn}^{2+}$ . This contradicts the common perception of manganese cycling (Aller, 1994) and to date we have no explanation for this apparent inconsistency.

The measured fluxes (fig. 18), except for that of  $\text{NO}_3^-$ , exhibited clear seasonal variations with elevated levels during the short summer period. The rapid increase in these fluxes was presumably caused by the settling of a phytoplankton bloom (Rysgaard and others, 1999), and was followed by an equally prompt decline. This characteristic seasonal dynamic was also clearly visible in the simulated fluxes (fig. 18). Concomitant dynamic changes simulated for the concentration profiles (fig. 17) indicated that the seasonality of fluxes was caused by enhanced OM mineralization only in the upper few centimeters of the sediment.

On an annual basis, the fluxes of  $\Sigma\text{CO}_2$ ,  $\text{O}_2$ ,  $\text{NH}_4^+$ , and  $\text{NO}_3^-$  were estimated to be  $-2300$ ,  $2350$ ,  $-33$ , and  $-30 \text{ mmol m}^{-2} \text{ year}^{-1}$  by Rysgaard and others (1998), while the corresponding simulated fluxes were  $-2300$ ,  $2270$ ,  $-81$ , and  $-35 \text{ mmol m}^{-2} \text{ year}^{-1}$ . Given the uncertainties of the annual fluxes as they were estimated by Rysgaard and others (1998) from periodic measurements (fig. 18), the only significant deviation was found for  $\text{NH}_4^+$ . This deviation might be explained at least partly by the fact that urea is not included explicitly in the model. As shown by Rysgaard and others (1998), nitrogen was also released from the sediment throughout the year in the form of urea in quantities of 25 to 50 percent of those of  $\text{NH}_4^+$ . Thus it might have been more correct to compare the simulated release of  $\text{NH}_4^+$  with the combined measured release of  $\text{NH}_4^+$  and urea. It is also possible that the simulated removal of  $\text{NH}_4^+$  by irrigation, which consists of 82 percent of the total flux, was overestimated significantly. In the model parameterization, the same irrigation parameter was chosen for  $\text{NH}_4^+$  and  $\Sigma\text{CO}_2$  (fig. 5), despite the fact that reduced irrigation parameters were applied for other solutes,  $\text{Mn}^{2+}$  (fig. 7) and  $\text{Fe}^{2+}$ , which react with  $\text{O}_2$  in the sediment near the wall in well-irrigated burrows. This phenomenon can reduce the removal of such solutes from sediments significantly and is not appropriately accounted for in the non-local source-sink function describing the effects of irrigation (see above). If nitrifying bacteria were abundant in the sediment near burrow walls it is likely that substantial amounts of  $\text{NH}_4^+$  actually were transformed to  $\text{NO}_3^-$  rather than being removed by irrigation. The irrigation parameter for  $\text{NH}_4^+$  was not reduced relative to

the one determined for  $\Sigma\text{CO}_2$  because adequate measurements to support such an analysis were not available.

### *Sensitivity Analysis*

Most of the 31 selected input parameters included in the sensitivity analysis exhibited relatively large responses to the changes imposed (fig. 15). Overall, the order of input parameters, representing their decreasing influence on simulated results, showed the same picture regardless of which of the two sensitivity measures (eq 4) was considered. A better sense of the sensitivities shown in figure 15 can be obtained by relating them to the results of the trial-and-error simulations conducted as part of the model parameterization (figs. 5, 7 to 12, and 14). The rate constant for the slow decomposing OM pool ( $K_{\text{OM},s}$ ) was not surprisingly one of the most influential input parameters (fig. 15). Furthermore, we also expected that the concentration  $[\text{H}_2\text{S}]_{\text{stop}}$  at which the  $\text{S}^0$  disproportionation (R 21) comes to a complete stop, was one of the least influential parameters because the  $\text{H}_2\text{S}$  concentrations at all depths were simulated to be significantly lower than the  $10\ \mu\text{M}$  assigned to  $[\text{H}_2\text{S}]_{\text{stop}}$ . The generally high level of sensitivity to changes in input parameters is a positive characteristic as it ensures good precision in the fitting when the model was parameterized.

### *Comparison with Other Modeling Studies*

In all, seven secondary redox reactions and their regulations (R7, R9, R10, R12, R13, R14, R15) were identical to ones included in the model of Van Cappellen and Wang (1996). For these reactions we used their rate constants as starting values when the model was parameterized. With respect to the rate constants  $K_9$  and  $K_{12}$ , no changes were made relative to values reported by Van Cappellen and Wang (1996). The values of  $K_7$ ,  $K_{13}$ ,  $K_{14}$ , and  $K_{15}$  were adjusted moderately, all within ranges defined either by variations in the three different site applications presented by Wang and Van Cappellen (1996) or by findings in a literature survey conducted by these authors. Only  $K_{10}$  was reduced significantly from its starting value, because we included two  $\text{MnO}_2$  pools for this reaction, while Van Cappellen and Wang included only one pool corresponding approximately to the pool of  $\text{MnO}_{2A}$  in our model. Additionally, the distribution of the total OM mineralization on oxic decomposition; denitrification; and manganese, iron, and sulfate reduction implemented through the limiting concentrations  $[\text{O}_2]_{\text{lim}}$ ,  $[\text{NO}_3^-]_{\text{lim}}$ ,  $[\text{MnO}_2]_{\text{lim}}$ , and  $[\text{FeOOH}]_{\text{lim}}$  was adapted from Van Cappellen and Wang (1996). The values of  $[\text{O}_2]_{\text{lim}}$  and  $[\text{NO}_3^-]_{\text{lim}}$  obtained in our parameterization, again using the values of Van Cappellen and Wang (1996) as starting values, were identical to the values reported by these authors. This result was obtained even though we utilized two pools for OM and simulated the depth-dependent mineralization of each pool while Van Cappellen and Wang (1996) imposed a known OM mineralization rate as a function of depth. The value determined for  $[\text{MnO}_2]_{\text{lim}}$  was within the rather wide range of 4000 to 32000  $\text{nmol g}^{-1}$  found by Wang and Van Cappellen (1996) in their model applications for three different sites. Compared to the value obtained by these authors,  $[\text{FeOOH}]_{\text{lim}}$  was found to be approximately twice as small, which is consistent with the fact that we partitioned FeOOH into two pools, only one of which was utilized by iron-reducing bacteria.

In applying the 3-G model, we determined rate constants for the two degradable OM pools of 76 and  $0.095\ \text{year}^{-1}$ . These values can be compared to those of 24 and  $1.4\ \text{year}^{-1}$  found by Westrich and Berner (1984) from incubation experiments of fresh planktonic material, and rate constants of 58 and  $3.3\ \text{year}^{-1}$  obtained when fitting the 3-G model to the similar data of Otsuki and Hanya (1972). Thus, while the most reactive OM in the Young Sound sediment corresponds to the most reactive components of fresh phytoplankton, the slower pool exhibits a markedly slower decay than found for plankton in these studies. This is not surprising, considering that the



experiments of Otsuki and Hanya (1972) and Westrich and Berner (1984) had durations of 1 to 2 years while the OM described in our model ranges from fresh planktonic material to OM that is several hundred years old. Consequently, the low rate constant is more appropriately compared with values determined for similar time scales. Compilations of such data exhibit considerable scatter (Tromp and others, 1995; Boudreau, 1997), but our rate constant of  $0.095 \text{ year}^{-1}$  generally agrees with these compiled values. It agrees closely with the rate of  $0.11 \text{ year}^{-1}$  that can be calculated from the correlation suggested by Boudreau (1997) for the rate constant of organic decay in the upper 10 to 20 centimeters as a function of sediment accumulation rates. The large scatter in the available data does not allow us to infer a temperature dependence of these rate constants, but the permanently low temperature below  $-1^{\circ}\text{C}$  does not appear to have any extraordinary effect on carbon mineralization.

#### *Pathways and Cycles*

The predicted OM mineralization through the different degradation pathways offers a detailed picture of the relative contribution of oxygen respiration; denitrification; and manganese, iron and sulfate reduction; and also of the partitioning of the secondary redox reactions that cannot be directly measured by present-day techniques.

Of the total  $\text{O}_2$  consumption, only 40 percent was used directly in the OM mineralization through bacterial oxygen respiration (fig. 21A). The remaining 60 percent was used to re-oxidize various reduced compounds being produced from manganese, iron, and sulfate reduction, and also to oxidize  $\text{NH}_4^+$  through nitrification. Re-oxidation of  $\text{Fe}^{2+}$  and iron sulfides was responsible for 48 percent of the total  $\text{O}_2$  taken up by the sediment (fig. 21A), while nitrification was responsible for the remaining 12 percent.

Since the fast OM pool was diminished to close to zero at depths where iron and sulfate reduction occurred, these reactions were supported almost exclusively by the slower OM pool. Oxygen respiration, denitrification, and iron and sulfate reduction were responsible for 22, 7, 29, and 42 percent, respectively, of the turnover of the slow OM pool (fig. 21B). Oxygen respiration was responsible for 98 percent of the turnover of the fast OM pool, while denitrification and iron reduction each accounted for only 1 percent (fig. 21B).

Production of  $\text{NH}_4^+$  through OM mineralization was coupled primarily to  $\text{O}_2$  respiration, iron reduction and sulfate reduction in proportions of 39, 23, and 32 percent, respectively, while a smaller fraction of 6 percent came from denitrification (fig. 21C). Nitrification was significant and consumed 64 percent of the produced  $\text{NH}_4^+$  while the remaining 36 percent was released to the water column. Twenty-five percent of the  $\text{NO}_3^-$  produced through nitrification was released to the water column, while 75 percent was consumed by denitrification and released to the water column as  $\text{N}_2$ .

Manganese was cycled rapidly, with permanent burial accounting for only a few percent of the total manganese reduction (fig. 22A), as has been observed in other coastal sediments (Aller, 1994; Thamdrup and others, 1994b). Eighty-eight percent of the  $\text{Mn}^{2+}$  re-oxidation occurred in the water column because of an efficient removal of  $\text{Mn}^{2+}$  from the sediment. This removal was distributed evenly between molecular diffusion, bioturbation, and irrigation. Manganese recycling through the water column is well documented for coastal sediments, although earlier studies have estimated lower fractions of less than 30 percent of produced  $\text{Mn}^{2+}$  (Sundby and Silverberg, 1985; Thamdrup and others, 1994a). However, previous modeling studies have also suggested a dominance of manganese recycling through the water column similar to the dominance we found (Wang and Van Cappellen, 1996).

Iron also was cycled rapidly, with permanent deposition of iron compounds accounting for only 6 percent of the total internal iron reduction (fig. 22B). This dominance of internal iron cycling is a general characteristic of continental marine sediments (Canfield and others, 1993a; Thamdrup and Canfield, 1996). Contrasted with manganese, however, iron recycling through the water column was insignificant. This behavior was the combined result of the exclusion of  $\text{Fe}^{2+}$  irrigation argued for earlier and the substantially faster reaction in the upper centimeters of the sediment with  $\text{O}_2$  of  $\text{Fe}^{2+}$  (R9) relative to  $\text{Mn}^{2+}$  (R8). This difference is reflected in the ratio of 100 between the rate constants for these reactions. Bacterial reduction accounted for 97 percent of the total reduction of the  $\text{FeOOH}$  pool,  $\text{FeOOH}_A$ , accessible to both biological and chemical reactions. Ninety-six percent of the reduced  $\text{FeOOH}$  was re-oxidized in the sediment, with  $\text{O}_2$  accounting for 99 percent of this re-oxidation and 1 percent due to  $\text{MnO}_2$ . In other coastal sediments,  $\text{MnO}_2$  has been found to account for a larger part of the re-oxidation (Canfield and others, 1993a; Aller 1994), but the small contribution determined here is most likely explained by particularly low  $\text{MnO}_2$  concentrations. In comparison, the oxidation of  $\text{Fe}^{2+}$  accounted for 63 percent of the total  $\text{MnO}_2$  reduction (fig. 22A).

Sulfur likewise was cycled internally with a permanent burial of only 20 percent of the sulfur produced by sulfate reduction (fig. 22C), which agrees with the general perception of sulfur cycling in marine sediments (Jørgensen, 1982). Most of the sulfate regenerated was through aerobic oxidation of  $\text{FeS}$  and  $\text{FeS}_2$ , 9 and 66 percent, respectively. These findings agree with a previous study that concluded that anaerobic sulfide oxidation is of minor importance (Thamdrup and others, 1994b). Disproportionation of  $\text{S}^0$  accounted for 25 percent of the total sulfate regeneration. Moreover, as much as 79 percent of the sulfide produced through sulfate reduction was transformed through disproportionation, after partial re-oxidation of  $\text{H}_2\text{S}$  to  $\text{S}^0$ , mainly coupled to the reduction of  $\text{FeOOH}$ . Sulfide played a key role in the sediment as reflected by the significant gross production of  $585 \text{ mmol m}^{-2} \text{ year}^{-1}$  that was balanced by an equally sized gross consumption. This fine balance explains the absence of  $\text{H}_2\text{S}$  in the sediment and is a good example of the serious misinterpretation possible if the standing concentration of  $\text{H}_2\text{S}$ , or any other constituents, is used alone to evaluate their importance in different sediment redox reactions.

#### *Extensions Relative to Previous Models*

Several substantial changes were made to the model during its application to the Young Sound sediment. These changes were identified based on specific deviations between simulated and measured results. For example, in an early version of the model, the OM mineralization was described by only one degradable OM pool similar to the model of Dhakar and Burdige (1996). However, comparisons between the simulated and measured  $\Sigma\text{CO}_2$  flux through the summer months (figs. 10 or 18) showed clearly that one additional degradable OM pool was required in order to describe the rapid dynamic of the  $\Sigma\text{CO}_2$  flux.

Likewise, in one of the first versions of the model only one pool was utilized for each of the solid species  $\text{MnO}_2$  and  $\text{FeOOH}$ . After comparing simulated and measured results, this formulation was deemed inadequate to describe the concentration profiles in the manganese and iron cycles (fig. 17). More specifically, the one-pool approach for both  $\text{MnO}_2$  and  $\text{FeOOH}$  obviously assumed that all  $\text{MnO}_2$  and  $\text{FeOOH}$  could be reduced biologically through the primary redox reactions, which were simulated to occur at high rates relatively close to the sediment surface. The corresponding production of  $\text{Mn}^{2+}$  and  $\text{Fe}^{2+}$  resulted in profiles for both solutes that also reached their maximum values close to the sediment surface and then declined rapidly with depth. These profile shapes diverged substantially from those of the measured  $\text{Mn}^{2+}$  and  $\text{Fe}^{2+}$  profiles (fig. 17). The particular depth distributions of the  $\text{Mn}^{2+}$  and  $\text{Fe}^{2+}$

net production that resulted in simulated concentration profiles comparable to those measured, could only be achieved by introducing one additional pool for each of the solid species  $\text{MnO}_2$  and  $\text{FeOOH}$ . While the metal oxides required a slight increase in complexity of the model, the simple adsorption model provided a good description of non-sulfide-bound particulate  $\text{Fe}^{2+}$ . Without a more accurate description of  $\text{Fe}^{2+}$  speciation in surface sediments, we suggest that this inflated adsorption model may be applicable to other fine-grained sediments.

$\text{S}^0$  was not measured in the Young Sound sediment, but other studies have reported ratios of  $[\text{S}^0]:[\text{FeS}]$  on the order of 0.1 (Sørensen and Jørgensen, 1987; Thamdrup and others, 1994b). A comparable ratio was found in our simulations. This result was directly linked to the disproportionation of  $\text{S}^0$  (R21), which was not accounted for in the initial versions of the model. These early simulations suffered from a high build-up of  $\text{S}^0$  to concentration levels almost 2000 times higher than what we obtained with the presented model (fig. 16). The elevated  $\text{S}^0$  concentration levels were 7 times higher than the sulfur bound in the  $\text{FeS}_2$  pool, which is far above any reported observations (Sørensen and Jørgensen, 1987; Thamdrup and others, 1994b). We are only aware of one experimental quantification of  $\text{S}^0$  disproportionation in a marine sediment (Canfield and Thamdrup, 1996), but based on sulfur isotope distributions, disproportionation processes have been suggested to contribute significantly to the oxidative sulfur transformations in coastal sediments (Canfield and Thamdrup, 1994; Habicht and Canfield, 2001). Our present findings further support the importance of  $\text{S}^0$  disproportionation.

Finally, we emphasize that these substantial changes to the model could only be identified and implemented because of the extensive measurements available for the Young Sound sediment. Although a substantial amount of knowledge and experience in mathematical modeling of OM and nutrient diagenesis has been gained from the many reported modeling studies, it is still crucial to have detailed measurements for parameterizations and validations of such models.

#### ACKNOWLEDGMENTS

We thank P. Regnier and two anonymous reviewers for their constructive reviews of this paper. We also thank K. J. McGlathery for commenting on the manuscript and M. J. Gore for copyediting the manuscript. This study was supported by grants from University of Virginia and the Danish National Science Research Councils (contract # 9501025 and # 9700224).

#### REFERENCES

- Aller, R. C., 1980a, Diagenetic processes near the sediment-water interface of Long Island Sound. II. Fe and Mn: *Advances in Geophysics*, v. 22, p. 351–415.
- 1980b, Quantifying solute distributions in the bioturbated zone of marine sediments by defining an average microenvironment: *Geochimica et Cosmochimica Acta*, v. 44, p. 1955–1965.
- 1994, The sedimentary Mn cycle in Long Island Sound: its role as intermediate oxidant and the influence of bioturbation,  $\text{O}_2$  and  $\text{C}_{\text{org}}$  flux on diagenetic reaction balance: *Journal of Marine Research*, v. 52, p. 259–295.
- Archer, D. E., Morford, J. L., and Emerson, S. R., 2002, A model of suboxic sedimentary diagenesis suitable for automatic tuning and gridded global domains: *Global Biogeochemical Cycles*, v. 16, p. 17(1)–17(21).
- Balzer, W., 1982, On the distribution of iron and manganese at the sediment/water interface: thermodynamic versus kinetic control: *Geochimica et Cosmochimica Acta*, v. 46, p. 1153–1161.
- Berg, P., Risgaard-Petersen, N., and Rysgaard, S., 1998, Interpretation of measured concentration profiles in sediment pore water: *Limnology and Oceanography*, v. 43, p. 1500–1510.
- Berg, P., Rysgaard, S., Funch, P., and Sejr, M., 2001, Effects of bioturbation on solutes and solids in marine sediments: *Aquatic Microbial Ecology*, v. 26, p. 81–94.
- Berner, R. A., 1970, Sedimentary pyrite formation: *American Journal of Science*, v. 268, p. 1–23.
- 1980a, Early diagenesis. A theoretical approach: Princeton, New Jersey, Princeton University Press, 241 p.

- 1980b, A rate model for organic matter decomposition during bacterial sulfate reduction in marine sediments. *Biogeochemistry of organic matter at the sediment-water interface: CNRS International Colloquium*, p. 35–44.
- 1981, Authigenic mineral formation resulting from organic matter decomposition in modern sediments: *Fortschritte der Mineralogie*, v. 59, p. 117–135.
- Boudreau, B. P., 1984, On the equivalence of nonlocal and radial-diffusion models for porewater irrigation: *Journal of Marine Research*, v. 42, p. 731–735.
- 1996, A method-of-lines code for carbon and nutrient diagenesis in aquatic sediments: *Computers and Geosciences*, v. 22, p. 479–496.
- 1997, *Diagenetic models and their implementation*: Berlin, Heidelberg, New York, Springer-Verlag, 414 p.
- Boudreau, B. P., Mucci, A., Sundby, B., Luther, G. W., and Silverberg, N., 1998, Comparative diagenesis at three sites on the Canadian continental margin: *Journal of Marine Research*, v. 56, p. 1259–1284.
- Broecker, W. S., and Peng, T. H., 1974, Gas exchange rates between air and sea: *Tellus*, v. 26, p. 21–35.
- Canfield, D. E., 1989, Reactive iron in marine sediments: *Geochimica et Cosmochimica Acta*, v. 53, p. 619–632.
- 1997, The geochemistry of river particulates from the continental USA: major elements: *Geochimica et Cosmochimica Acta*, v. 61, p. 3349–3365.
- Canfield, D. E., and Thamdrup, B., 1994, The production of  $^{34}\text{S}$ -depleted sulfide during bacterial disproportionation of elemental sulfur: *Science*, v. 266, p. 1973–1975.
- 1996, Fate of elemental sulfur in an intertidal sediment: *FEMS Microbiology Ecology*, v. 19, p. 95–103.
- Canfield, D. E., Thamdrup, B., and Hansen, J. W., 1993a, The anaerobic degradation of organic matter in Danish coastal sediments: Iron reduction, manganese reduction, and sulfate reduction: *Geochimica et Cosmochimica Acta*, v. 57, p. 3867–3883.
- Canfield, D. E., Jørgensen, B. B., Fossing, H., Glud, R., Gundersen, J., Ramsing, N. B., Thamdrup, B., Hansen, J. W., Nielsen, L. P., and Hall, P. O. J., 1993b, Pathways of organic carbon oxidation in three continental margin sediments: *Marine Geology*, v. 113, p. 27–40.
- Cornell, R. M., and Schwertmann, U., 1996, *The Iron Oxides*: Weinheim, New York, VCH, 573 p.
- Dhakar, S. P., and Burdige, D. J., 1996, A coupled, non-linear, steady state model for early diagenetic processes in pelagic sediments: *American Journal of Science*, v. 296, p. 296–330.
- Emerson, D., and Moyer, C., 1997, Isolation and characterization of novel iron-oxidizing bacteria that grow at circumneutral pH: *Applied Environmental Microbiology*, v. 63, p. 4784–4792.
- Emerson, S., Jahnke, R., and Heggie, D., 1984, Sediment-water exchange in shallow water estuarine sediments: *Journal of Marine Research*, v. 42, p. 709–730.
- Finster, K., Liesack, W., and Thamdrup, B., 1998, Elemental sulfur and thiosulfate disproportionation by *Desulfocapsa sulfexigens* sp. nov., a new anaerobic bacterium isolated from marine surface sediment: *Applied Environmental Microbiology*, v. 64, p. 119–125.
- Fossing, H., Ferdelman, T. G., and Berg, P., 2000, Sulfate reduction and methane oxidation in continental margin sediments influenced by irrigation (South-East Atlantic off Namibia): *Geochimica et Cosmochimica Acta*, v. 64, p. 897–910.
- Froelich, P. N., Klinkhammer, G. P., Bender, M. L., Luedtke, G. R., Heath, G. R., Cullen, D., and Dauphin, P., 1979, Early oxidation of organic matter in pelagic sediments of the eastern equatorial Atlantic: suboxic diagenesis: *Geochimica et Cosmochimica Acta*, v. 43, p. 1075–1090.
- Glud, R. N., Risgaard-Petersen, N., Thamdrup, B., Fossing, H., and Rysgaard, S., 2000, Benthic carbon mineralization in a high-Arctic Sound, (Young Sound, NE-Greenland): *Marine Ecology Progress Series*, v. 206, p. 59–71.
- Habicht, K. S., and Canfield, D. E., 2001, Isotope fractionation by sulfate-reducing natural populations and the isotopic composition of sulfide in marine sediments: *Geology*, v. 29, p. 555–558.
- Herbert, R. A., 1999, Nitrogen cycling in coastal marine ecosystems: *FEMS Microbiology Review*, v. 23, p. 563–590.
- Herman, P. M. J., Soetaert, K., Middelburg J. J., Heip, C., Lohse, L., Epping, E., Helder, W., Antia, A. N., and Peinert, R., 2001, The seafloor as the ultimate sediment trap – using sediment properties to constrain benthic-pelagic exchange processes at the Goban Spur: *Deep-Sea Research II*, v. 48, p. 3245–3264.
- Iversen, N., and Jørgensen, B. B., 1993, Measurements of the diffusion coefficients in marine sediments: influence of porosity: *Geochimica et Cosmochimica Acta*, v. 57, p. 571–578.
- Jørgensen, B. B., 1978, A comparison of methods for quantification of bacterial sulfate reduction in coastal marine sediments. 2. Calculation from mathematical models: *Geomicrobiology Journal*, v. 1, p. 29–47.
- 1982, Mineralization of organic matter in the sea bed - role of sulphate reduction: *Nature*, v. 296, p. 643–645.
- Koretsky, C. M., Meile, C., and Van Cappellen, P., 2002, Quantifying bioirrigation using ecological parameters: a stochastic approach: *Geochemical Transactions*, v. 3, p. 17–30.
- Kostka, J. E., and Luther, G. W., 1994, Partitioning and speciation of solid phase iron in saltmarsh sediments: *Geochimica et Cosmochimica Acta*, v. 58, p. 1701–1710.
- Kristensen, E., Ahmed, S. I., and Devol, A. H., 1995, Aerobic and anaerobic decomposition of organic matter in marine sediment: which is fastest: *Limnology and Oceanography*, v. 40, p. 1430–1437.
- Li, Y. H., and Gregory, S., 1974, Diffusion of ions in sea water and deep-sea sediments: *Geochimica et Cosmochimica Acta*, v. 38, p. 703–714.
- Luff, R., Wallmann, K., Grandel, S., and Schlüter, M., 2000, Numerical modeling of benthic processes in the deep Arabian Sea: *Deep-Sea Research II*, v. 47, p. 3039–3072.
- Mackin, J. E., and Aller, R. C., 1984, Ammonium adsorption in marine sediments: *Limnology and Oceanography*, v. 29, p. 250–257.



- Meile, C., Koretsky, C. M., and Van Cappellen, P., 2001, Quantifying bioirrigation in aquatic sediments: An inverse modeling approach: *Limnology and Oceanography*, v. 46, p. 164–177.
- Meysman, F. J. R., Middelburg, J. J., Herman, P. M. J., and Heip, C. H. R., 2003a: Reactive transport in surface sediments. I. Model complexity and software quality: *Computers and Geosciences*, v. 29, p. 291–300.
- 2003b: Reactive transport in surface sediments. II. Media: an object-oriented problem-solving environment for early diagenesis: *Computers and Geosciences*, v. 29, p. 301–318.
- Otsuki, A., and Hanya, T., 1972, Production of dissolved organic matter from dead green algal cells. I. Aerobic microbial decomposition: *Limnology and Oceanography*, v. 17, p. 248–257.
- Rysgaard, S., and Berg, P., 1996, Mineralization in a northeastern Greenland sediment: mathematical modelling, measured sediment pore water profiles and actual activities: *Aquatic Microbial Ecology*, v. 11, p. 297–305.
- Rysgaard, S., Finster, K., and Dahlgard, H., 1996, Primary production, nutrient dynamics and mineralisation in a northeastern Greenland fjord during the summer thaw: *Polar Biology*, v. 16, p. 497–506.
- Rysgaard, S., Thamdrup, B., Risgaard-Petersen, N., Fossing, H., Berg, P., Christensen, P. B., and Dalsgaard, T., 1998, Seasonal carbon and nitrogen mineralization in a high-Arctic coastal marine sediment, Young Sound, Northeast Greenland: *Marine Ecology Progress Series*, v. 175, p. 261–276.
- Rysgaard, S., Nielsen, T. G., and Hansen, B., 1999, Seasonal variation in nutrients, pelagic primary production and grazing in a high-Arctic coastal marine ecosystem, Young Sound, Northeast Greenland: *Marine Ecology Progress Series*, v. 179, p. 13–25.
- Sobolev, D., and Roden, E. E., 2001, Suboxic deposition of ferric iron by bacteria in opposing gradients of Fe(II) and oxygen at circumneutral pH: *Applied Environmental Microbiology*, v. 67, p. 1328–1334.
- Soetaert, K., Herman, P. M. J., and Middelburg, J. J., 1996, A model of early diagenetic processes from the shelf to abyssal depths: *Geochimica et Cosmochimica Acta*, v. 60, p. 1019–1040.
- Sørensen, J., and Jørgensen, B. B., 1987, Early diagenesis in sediments from Danish coastal waters: microbial activity and Mn-Fe-S geochemistry: *Geochimica et Cosmochimica Acta*, v. 51, p. 1583–1590.
- Stumm, W., and Morgan, J. J., 1981, *Aquatic Chemistry*: New York, John Wiley and Sons, 583 p.
- Sundby, B., and Silverberg, N., 1985, Manganese fluxes in the benthic boundary layer: *Geochimica et Cosmochimica Acta*, v. 50, p. 372–381.
- Taillefert, M., Bono, A. B., and Luther, G. W., 2000, Reactivity of freshly formed Fe(III) in synthetic solutions and (pore)waters: voltammetric evidence of an aging process: *Environmental Science and Technology*, v. 34, p. 2169–2177.
- Thamdrup, B., 2000, Microbial manganese and iron reduction in aquatic sediments: *Advances in Microbial Ecology*, v. 16, p. 41–84.
- Thamdrup, B., and Canfield, D. E., 1996, Pathways of carbon oxidation in continental margin sediments off central Chile: *Limnology and Oceanography*, v. 41, p. 1629–1650.
- Thamdrup, B., and Dalsgaard, T., 2000, The fate of ammonium in anoxic manganese oxide-rich marine sediment: *Geochimica et Cosmochimica Acta*, v. 64, p. 4157–4164.
- Thamdrup, B., Finster, K., Hansen, J. W., and Bak, F., 1993, Bacterial disproportionation of elemental sulfur coupled to chemical reduction of iron or manganese: *Applied Environmental Microbiology*, v. 59, p. 101–108.
- Thamdrup, B., Glud, R. N., and Hansen, J. W., 1994a, Manganese oxidation and in situ fluxes from a coastal sediment: *Geochimica et Cosmochimica Acta*, v. 58, p. 2563–2570.
- Thamdrup, B., Fossing, H., and Jørgensen, B. B., 1994b, Manganese, iron, and sulfur cycling in a coastal marine sediment, Aarhus Bay, Denmark: *Geochimica et Cosmochimica Acta*, v. 58, p. 5115–5129.
- Tromp, T. K., Van Cappellen, P., and Key, R. M., 1995, A global model for the early diagenesis of organic carbon and organic phosphorus in marine sediments: *Geochimica et Cosmochimica Acta*, v. 59, p. 1259–1284.
- Van Cappellen, P., and Wang, Y., 1996, Cycling of iron and manganese in surface sediments: A general theory for the coupled transport and reaction of carbon, oxygen, nitrogen, sulfur, iron, and manganese: *American Journal of Science*, v. 296, p. 197–243.
- Van Cappellen, P., Gaillard, J. F., and Rabouille, C., 1993, Biogeochemical transformations in sediments: Kinetic models of early diagenesis, in Wollast, R., Mackenzie, F. T., and Chou, L., editors, *Interactions of C, N, P, and S Biogeochemical Cycles and Global Change*: Berlin, Heidelberg, New York, Springer-Verlag, p. 401–445.
- Wang, Y., and Van Cappellen, P., 1996, A multicomponent reactive transport model of early diagenesis: Application to redox cycling in coastal marine sediments: *Geochimica et Cosmochimica Acta*, v. 60, p. 2993–3014.
- Westrich, J. T., and Berner, R. A., 1984, The role of sedimentary organic matter in bacterial sulfate reduction: the G-model tested: *Limnology and Oceanography*, v. 29, p. 236–249.
- Wijsman, J. W. M., Herman, P. M. J., Middelburg, J. J., and Soetaert, K., 2002, A model for early diagenetic processes in sediments of the continental shelf of the Black Sea: *Estuarine Coastal and Shelf Science*, v. 54, p. 403–421.